



Universiteit  
Leiden

The Netherlands

## Flow-based arterial spin labeling: from brain to body

Franklin, S.L.

### Citation

Franklin, S. L. (2022, June 16). *Flow-based arterial spin labeling: from brain to body*. Retrieved from <https://hdl.handle.net/1887/3309826>

Version: Publisher's Version

License: [Licence agreement concerning inclusion of doctoral thesis in the Institutional Repository of the University of Leiden](#)

Downloaded from: <https://hdl.handle.net/1887/3309826>

**Note:** To cite this publication please use the final published version (if applicable).

# Flow-based arterial spin labeling

From brain to body



Suzanne Lisa Franklin.



**Flow-based arterial spin labeling:  
from brain to body**

Suzanne Lisa Franklin

**Cover design:** Sophie Pammler

**Printing/layout:** Optima Grafische Communicatie, Rotterdam, The Netherlands ([www.ogc.nl](http://www.ogc.nl))

**ISBN:** 978-94-6361-683-6

The work presented in this thesis was carried out at the C.J. Gorter Center at Leiden University Medical Center, Leiden, The Netherlands, and the Imaging Department at University Medical Center Utrecht, Utrecht, The Netherlands.

This research project was funded by Netherlands Organisation for Scientific Research (NWO), domain: Applied and Engineering sciences, project number: 14951.

© Suzanne Lisa Franklin, 2022

No parts of this book may be reproduced or transmitted in any form or by any means without permission of the copyright owner. Copyright of the published chapters is held by the publishers of the journal in which the work appeared. All rights reserved.

Flow-based arterial spin labeling:  
from brain to body

Proefschrift

Ter verkrijging van  
de graad van doctor aan de Universiteit Leiden,  
op gezag van rector magnificus prof.dr.ir. H. Bijl,  
volgens besluit van het college voor promoties  
te verdedigen op donderdag 16 juni 2022  
klokke 15.00 uur

door

Suzanne Lisa Franklin

geboren te Eindhoven  
in 1990

Promotoren	Prof. Dr. Ir. M.J.P. van Osch Prof. Dr. A. Webb
Co-promotor	Dr. C. Bos, <i>Center for Image Sciences, University Medical Center Utrecht, Utrecht, The Netherlands</i>
Promotiecommissie	Prof. Dr. H.J. Lamb Prof. Dr. Ir. A.J. Nederveen, <i>Department of Radiology and Nuclear Medicine, Amsterdam University Medical Centers, University of Amsterdam, Amsterdam, The Netherlands</i> Prof. Dr. U.A. van der Heide, <i>Department of Radiation Oncology, The Netherlands Cancer Institute, Amsterdam, The Netherlands</i> Dr. J. Hutter, <i>Centre for the Developing Brain, School of Imaging Sciences and Biomedical Engineering, King's College London, London, UK</i>

Progress is born of doubt and inquiry.

*Robert G. Ingersoll, 1871*





# CONTENTS

1.	<b>General introduction</b>	9
2.	<b>Influence of the cardiac cycle on velocity selective and acceleration selective arterial spin labeling.</b>	23
	Supporting Information	39
3.	<b>Multi-organ comparison of flow-based arterial spin labeling techniques: Spatially non-selective labeling for cerebral and renal perfusion imaging.</b>	45
	Supporting Information	66
4.	<b>Feasibility of velocity-selective arterial spin labeling in breast cancer patients for non-contrast enhanced perfusion imaging</b>	73
	Supporting Information Figures	88
5.	<b>Arterial Spin Labeling using Spatio-temporal Encoding (SPEN) readout for robust perfusion imaging in inhomogenous magnetic fields</b>	93
	Supporting Information Figures	106
	Appendix: theoretical background of spatio-temporal encoding	108
6.	<b>B0 and B1 influence on velocity selective inversion arterial spin labeling and background suppression efficiency</b>	113
7.	<b>Summary and general discussion</b>	125
8.	<b>Dutch summary</b>	135
9.	<b>References</b>	143
10.	<b>List of publications</b>	157
11.	<b>Curriculum vitae</b>	161
11.	<b>Acknowledgements</b>	165



# Chapter 1

---

**General introduction**

---



Blood is vital for survival of our organs. It delivers the oxygen and nutrients, necessary for cells to survive and perform their function. In addition, it transports waste products to the kidneys and liver[1]. Blood is pumped from the heart into the vascular tree. From the aorta, which has a diameter of approximately 3.2 cm[2], blood is transported to ever smaller arteries, and eventually into the microvasculature. The microvasculature consist of arterioles and capillaries, which have a diameter of approximately 5-100  $\mu\text{m}$  and 5-10  $\mu\text{m}$ , respectively[1]. It is at the capillary level, that the exchange of oxygen, nutrients and waste products takes place with the tissue[1].

Blood flow at the level of the microvasculature, i.e. perfusion, can provide important information about the function of the organ[3]. In case of e.g. tumorous tissue, blood flow can be increased, because the abnormal growth of cells requires an increased amount of oxygen and nutrients[4]. But there are also diseases associated with an abnormally low blood flow, e.g. acute kidney injury[5]. Here perfusion levels drop below the level required for the metabolic needs, resulting in impairment of kidney function.

This work covers development and optimization of magnetic resonance imaging (MRI) techniques to measure perfusion. Besides MRI, various other perfusion methods exist [6]; e.g. positron emission tomography (PET), single photon emission computed tomography (SPECT), Xenon-enhanced computed tomography (XeCT), and Doppler ultrasound. In PET, SPECT, and XeCT, radioactive tracers are used to generate contrast between blood and surrounding tissue. Although they use tracers with a relatively short half-life, examinations are still associated with a radiation dose of  $\sim 2$  mSv for PET, and  $\sim 10$  mSv for SPECT and XeCT. Considering that the average risk for developing cancer is estimated to increase with 0.012% for every mSv[7], caution is necessary with respect to the frequency that these techniques are employed. In addition, these techniques have a high cost and long examination times.  $\text{H}_2^{15}\text{O}$ -PET is the most expensive due to the requirement of an on-site cyclotron[6], [8]. Doppler ultrasound on the other hand, is completely non-invasive, but there is a limitation to which vessels can be examined and there is a large operator dependence[9].

MRI does not require radioactive tracers, but is often used in combination with gadolinium-based contrast agents (GBCAs) [10], i.e. Dynamic Contrast Enhanced (DCE-) MRI [11] and Dynamic Susceptibility Contrast (DSC) MRI [12]. However, there are also MRI-techniques that do not require administration of GBCAs. Arterial Spin Labeling (ASL) is a cluster of MRI-perfusion techniques, which is completely non-invasive, and which can provide a perfusion map, instead of assessing separate vessels, as in the case of Doppler ultrasound. Clinically, ASL is primarily used for brain applications [8], [13], [14], e.g. in patients with stenosis of brain feeding artery[8], [15], stroke[8], [16] or vascular dementia[8], [17]. However, there are various body applications where ASL could add considerable value[18], [19].

In this work, applications of ASL for perfusion measurements in kidneys and breast were developed, and solutions to the encountered technical challenges were investigated. This introduction will first discuss technical aspects and limitations of contrast enhanced MRI. Followed by an introduction to ASL, including spatially-selective and flow-based ASL, specific challenges that arise in body applications of ASL, i.e. field inhomogeneity, and a possible solution in terms of an alternative readout technique, i.e. spatial encoding (SPEN). Lastly, clinical applications will be discussed.

## CONTRAST ENHANCED MRI

In contrast enhanced MRI, GBCA's are used to create contrast between blood and the surrounding tissue[20]. GBCAs are paramagnetic and induce magnetic susceptibility effects, they thus shorten both  $T_1$  and  $T_2/T_2^*$ . Which effect dominates, depends on sequence parameters, as well as the location and concentration of the GBCA. The susceptibility effects are most pronounced when the GBCAs remain intravascular, causing magnetic field gradients that extend well beyond the vessel wall. This leads to  $T_2^*$ -shortening, in and around the vessels, and a subsequent *loss* in signal[21]. At the same time GBCAs also shorten  $T_1$ , which will *enhance* the signal on a  $T_1$ -weighted sequence. For perfusion measurement, there are two types of dynamic contrast enhanced MRI, i.e. DSC-MRI and DCE-MRI. DSC exploits the  $T_2/T_2^*$  shortening induced by the contrast agent, while DCE exploits the  $T_1$ -shortening properties.

In DSC-MRI[12],  $T_2$  or  $T_2^*$ -weighted images are dynamically acquired before and after injection, to image the first pass of the bolus. It is mainly applied in brain, because the effect relies on GBCAs to remain intravascular, and an intact blood-brain-barrier prevents quick extravasation into surrounding tissue[21]. Evaluating the loss of signal during the first pass of the bolus, allows quantification of cerebral blood flow (CBF), cerebral blood volume (CBV), mean transit time (MTT), and timing parameters such as time-to-bolus peak (TBP)[21]. DSC is mainly used for evaluation of cerebral ischemia and brain tumors[22].

In DCE-MRI,  $T_1$ -weighted images are acquired dynamically before, and after administration of the GBCA, to enable kinetic analysis of the contrast “wash-in” and “wash-out” phase[22]. During the “wash-in” phase the signal is mainly characterized by blood flow. However, there is a second effect that is often exploited in oncology. With time, contrast agent leaks from the intravascular compartment into the extravascular space, from which it will be slowly cleared. This provides a measure of vessel wall permeability. This effect slowly takes over, and dominates the “wash-out” phase of the kinetic curve. Multiple analysis methods exist for DCE-MRI, e.g. evaluation of the shape of the kinetic curve and more advanced modeling allowing the quantification of blood flow, blood volume, and well as the rate at which the contrast agent

diffuses from blood to tissue, e.g.  $K_{\text{trans}}$ [23]. DCE-MRI is used in many different diseases and organs, e.g. imaging of tumors[10], monitoring therapy response[23], kidney function[23], and neurodegenerative diseases [10]. Permeability measures are employed to discriminate between benign and malignant tumors, since angiogenesis in malignant tumors lead to a higher vessel wall permeability[24], [25]. A rapid decrease in the “wash-out” phase of the kinetic curve, characterizes higher vessel wall permeability, giving a strong indication for malignancy[24], [26].

However, contrast agents should be used cautiously, especially in specific patient groups. About fifteen years ago, nephrogenic systemic fibrosis (NSF), a rare disease in patients with severe renal failure, was first linked to the use of GBCAs[10]. This prompted strict guidelines regarding the use of GBCA in patients with severe kidney failure and/or previous severe reactions to GBCAs[27], including recommendations on dosage and type of GBCA. Since then, the number of NSF incidences has been greatly reduced[10], [27], [28]. However, there are still concerns due to another recently identified side-effect, i.e. retention of contrast agent in organ tissue. Since 2014, numerous studies have been published showing retention of contrast agents in parts of the brain, skin and bones, even in healthy individuals, with unknown clinical and long-term effects[10], [28], [29]. The amount of retention is dependent on the type of contrast agent[29], [30] with macrocyclic agents showing less retention than linear GBCAs, but all seem to show some amount of retention[29]. For this reason, in addition to the important benefits of not requiring an intravenous injection, and enabling repeated measurements, non-contrast enhanced perfusion techniques, such as Arterial Spin Labeling (ASL) have gained a lot of traction.

## ARTERIAL SPIN LABELING

In contrast to DCE-MRI, ASL does not create contrast between blood and surrounding tissue by using a contrast agent. Instead, blood itself is used as an endogenous tracer [31]. The magnetization of blood is modulated to create a difference in magnetization between blood and tissue, and thus contrast. In ASL, two types of images are acquired alternatingly; an image where the magnetization of blood is modulated, i.e. labeled, followed by an image without labeling: the control image. Subtracting the label image from the control image results in the ASL image, which only shows signal of the labeled blood while other signals cancel out. Because ASL-signal is based on a difference in longitudinal magnetization, it will relax with  $T_1$ , causing a drop in SNR with time[32]. The amount blood compared to tissue is relatively low; e.g. the brain’s gray matter has a vascular volume of about 5%[33], even though it is one of the most highly perfused organs, receiving 15-20% of the cardiac output[34]. In an ASL



experiment you can expect to obtain a signal intensity of  $\sim 1\%$  of the relaxed brain signal[13]. This means that ASL is an inherently SNR-starved technique.

To maximize SNR multiple ASL techniques have been developed, which vary in the way blood is labeled, and what blood is labeled[32]. This work is mostly focused on flow-based ASL techniques; they label blood on flow velocity or acceleration, whereas more conventional ASL techniques label based on spatial location.

Another key component of the ASL sequence is background suppression. Background suppression aims to minimize all other sources of label/control differences, e.g. caused by motion or physiological noise, to prevent subtraction errors and improve SNR [13], [35], [36]. Background suppression consist of two or more non-selective inversion pulses in combination with a saturation pulse at the beginning of the sequence. The timings are optimized based on Bloch simulations of the magnetization to minimize the signal of relevant background signals at the time of acquisition. Because they are applied in both label and control condition, the difference between label and control, and thus the ASL-signal, is untouched. There is only a small loss due to imperfect inversion of the background suppression pulses[37].

## SPATIALLY SELECTIVE ARTERIAL SPIN LABELING

In spatially selective ASL, either a labeling plane is planned: such that all blood flowing through gets labeled, e.g. pseudo continuous ASL (pCASL)[38], or a volume is labeled: as in the case of pulsed ASL techniques, e.g. flow alternating inversion recovery (FAIR). The labeling takes place upstream of the imaging region. Which means that there is a delay, the transit delay or arterial transit time, before the labeled blood has reached the microvasculature in the imaging region.

The transit delay is not a physiological constant, but varies between regions, gender, age, pathology, and just generally between individuals[16], [39]–[42]. For example, MoyaMoya disease results in significantly increased, and a higher inter-subject variation of transit delays[43]. Image acquisition takes place at a certain delay, the post-labeling-delay (PLD), after labeling, to grant the labeled blood time to reach the microvasculature. The PLD ideally needs to be longer than the longest transit delay to make sure all labeled blood has reached the imaging region, and prevent perfusion underestimation[13]. However, because the ASL signal decays with  $T_1$  there is a limit to the length of PLD. The  $T_1$  of arterial blood is approximately 1.65s at 3T, so at a PLD of 1.65s already 63% of ASL-signal has decayed. This can cause limitations in organs with naturally slow blood flow, e.g. the breast[44]. Because the transit delay is usually not known beforehand, multiple PLDs can be acquired to improve perfusion quantification[13].

The recommended ASL technique for brain is pCASL [13]. For brain applications, the pCASL labeling plane is planned in the neck-region, on the carotids and vertebral arteries. The labeling plane is planned at a specific location to make sure that all feeding arteries are perpendicular to the labeling plane. This ensures that all blood flowing into the brain, is inverted [13], [38]. For body applications, planning of the labeling slab can be challenging. First, because of movement, e.g. due to respiration, it can be challenging to plan the plane at the right location. Movement of the organ into the labeling plane needs to be prevented, to prevent direct labeling of the tissue. Second, the vascular bed can be complex, complicating planning of the labeling plane such that all incoming blood flow is labeled correctly, i.e. so that all feeding arteries are perpendicular to the labeling plane. For example, the breast is fed mainly by the internal thoracic artery, but also to some extent by the intercostal and lateral thoracic arteries[45]. These different feeding arteries can all slightly differ in orientation, which can affect labeling efficiency[38]. Third, field inhomogeneity at the labeling location can reduce labeling efficiency, e.g. in the lung area[38], [46], [47]. For example, in renal applications, the labeling slab is planned on the aorta; it should be placed high enough to prevent kidneys from moving into the labeling slab during respiratory cycle; but should not be placed too high to prevent loss in labeling efficiency due to off-resonance around the lungs.

An alternative spatially-selective ASL approach is FAIR [48]. FAIR does not suffer from the same planning issues as pCASL, but there are other considerations that need to be taken into account during planning. In FAIR, difference between label and control is generated by using either a selective or non-selective inversion pulse, followed by a PLD and finally image acquisition. The selective inversion covers the imaging region with a certain additional width, to ensure proper inversion in the whole imaging region[48]. After subtraction, the ASL-signal will consist of the blood signal which was outside of the selective inversion pulse during labeling, and flowed into the imaging region during the PLD. So to label aortic blood, the aorta should be left out of the selective inversion pulse, which can be a challenge for e.g. renal ASL. When the coronal plane of the kidneys (partly) includes the aorta, then it will not be possible to include this part of the kidney in the imaging region, preventing whole kidney coverage.

## FLOW-BASED ARTERIAL SPIN LABELING

Flow-based ASL does not suffer from planning issues and transit time sensitivity[49], [50]. In flow-based ASL, blood is labeled non-spatially selective, based on either a cut-off velocity or acceleration. By choosing this cut-off low enough, blood is no longer only labeled upstream to, but also within the imaging region, essentially eliminating the transit time issues [49]. Various flow-based ASL techniques have been published which are either based on labeling blood by saturation, such as velocity-selective ASL (VS-ASL)[49], acceleration-selective ASL

(Acc-ASL)[51], VS-ASL with multiple VSASL-modules (mm-VSASL)[52], or inversion, i.e. velocity selective inversion-based ASL (VSI-ASL)[53]. Because flow-based ASL is inherently transit-time insensitive and does not require planning of a labeling slab, it is especially interesting for body applications.

VS-ASL was first introduced in 2006[49]. Velocity dependence is realized by a set of two bipolar gradients. Bipolar gradients have a zeroth gradient moment of zero, meaning that in case the hydrogen nuclei are static during application of the labeling module, the phase build up by each separate gradient cancel out[54]. However, when the hydrogen nuclei move, there will be a net phase build up, which depends on the velocity[54]. By summing the phase accrual of all velocities while assuming a laminar flow profile, the relation between longitudinal magnetization and velocity will form a sinc-profile [49]. At a velocity of zero, the magnetization remains untouched, while after the first zero-crossing of the sinc, the longitudinal magnetization is significantly reduced. The cut-off velocity is defined as the first zero-crossing and the magnetization is assumed to be saturated above this value[49]. The cut-off velocity is determined by the gradient strength and the delays in between the gradients. It is usually set to 2 cm/s, corresponding to the flow velocity found in the penetrating arteries of the brain's cortical surface[55], at which level within the arterial tree a laminar flow profile is still found[56]. The sequence is only sensitive to velocity in the direction of the gradient. However, because of increased tortuosity of smaller vessels, VS-ASL with a cutoff velocity  $< 4$  cm/s has been found to be relatively independent on the direction of velocity encoding [49]. The VS-ASL sequence consists of a labeling module including bipolar gradients in the label condition, and a control module without bipolar gradients in the control condition. These modules are followed by a PLD, and a second labeling module right before readout. This second labeling module is applied in both the label and control condition and includes bipolar gradients in both conditions. It acts as a vascular crusher, and ensures that only labeled blood that decelerated from above the cutoff velocity during the first labeling module, to below the cutoff velocity during the second module, gets imaged. This means that only arterial blood gets imaged, and venous blood does not, because arterial blood will decelerate as it flows further into the vascular tree, while venous blood does the opposite. The other important reason for having the second labeling module is that it enables quantification of perfusion. The second labeling module cuts off the bolus, and you need to know the bolus length to properly quantify the ASL-signal[49]. Note, that in VS-ASL, the PLD cannot be chosen too short. Even though labeling already takes place in the imaging region, the labeled blood needs enough time to decelerated below the cutoff velocity during the PLD, otherwise it will be crushed by the last VS-ASL module, and SNR will be compromised[49], [56]. In addition, if the PLD is too short, eddy currents induced by the gradients in the VS-ASL labeling module can lead to subtraction errors in the perfusion image[57].

After the introduction of the original VS-ASL approach, several flow-based techniques have been introduced to improve SNR. Acc-ASL is based on similar principles as VS-ASL, only in this case, the gradients in the labeling module are unipolar, introducing an acceleration-sensitivity instead of velocity[51]. In Acc-ASL, the second labeling module is not necessary to remove the venous component from the signal, because higher acceleration (or actually deceleration) mainly occurs on the arterial side and Acc-ASL therefore inherently labels arterial blood. The absence of the second labeling module means Acc-ASL can provide a higher SNR than VS-ASL. The second labeling module removes a significant part of the signal, i.e. all velocities larger than the cutoff velocity. However, a consequence is that quantification is not possible, because the bolus length will not be known[51]. Mm-VSASL is a variation of VS-ASL, where an additional labeling/control module is added to increase the amount of generated label[52]. VSI-ASL on the other hand, is based on a completely different principle. The VSI-ASL labeling module consists of a train of sub-pulses with bipolar gradients and refocusing pulses in between. Spins are inverted in small steps based on the Fourier principle; by using a rectangular amplitude envelope of the sub-pulses a sinc-shaped velocity profile is obtained[53], [58]. But theoretically, the amplitudes of the sub-pulses can be adjusted in such a way to obtain any desired velocity profile[58]. Contrary to VS-ASL, VSI-ASL inverts the static spins while the faster flowing spins retain their magnetization. For this reason VSI-ASL is usually combined with an odd number of background suppression pulses to keep the static tissue positive[53]. Because VSI-ASL is based on inversion instead of saturation it has a theoretical factor 2 SNR advantage compared to the other flow-based techniques. However, this is not met in practice, largely because the block pulses used in the VSI-module introduce a  $B_1$ -sensitivity which reduces labeling efficiency[53]. VSI-ASL can be used with either a velocity-insensitive control module, i.e. the same RF pulse train as the labeling module, with gradients turned off, or a velocity-compensated control module, i.e. the same RF pulse train and gradient lobes as the labeling module, only with a unipolar gradient orientation[53]. In the original implementation a velocity-compensated control module is used, because the velocity-insensitive control module the diffusion sensitivity of the label module is not compensated by the control. This could lead to an overestimation of blood flow[53]. However, the velocity-compensated control has  $B_1$ -sensitivity which could reduce labeling efficiency already at  $B_1$ -levels of  $1 \pm 0.1$ [53]. Although this does not provide clear issues in brain, it could potentially become a problem in body applications.

## MAGNETIC FIELD INHOMOGENEITY

One of the mechanisms through which the local  $B_0$  is disturbed is through variations in magnetic susceptibility. Magnetic susceptibility is a tissue characteristic which determines the degree to which the tissue becomes magnetized when placed in an external magnetic field[59].

Variations in magnetic susceptibility result in local changes to the precession frequency, so that these hydrogen nuclei are mapped to the wrong location within the MR-image, resulting in distortions of the imaged object[59]. In addition, large variations in susceptibility over a small distance can lead to additional dephasing, i.e. shortening of  $T_2^*$ , and consequently loss of signal[59]. These mechanisms affecting the homogeneity of  $B_0$  are larger in the body compared to brain due to more air-tissue interfaces, e.g. in the vicinity of the bowel and lungs[60]. This can complicate body applications of ASL in organs close to the lungs, such as breast and kidney.

Another mechanism affecting the  $B_0$  experienced by hydrogen nuclei, is their molecular environment. The molecular environment determines the degree to which the hydrogen nucleus is shielded from the externally applied magnetic field  $B_0$ [54]. The effect is a difference in precession frequency between different types of molecules, which results in a displacement between different tissue types, i.e. chemical shift. The most well-known chemical shift effect is that between water and fat.

Also the  $B_1$ -field is less homogeneous in body compared to brain. The object to be imaged is typically larger for body imaging, which means it can become of similar dimensions as the 'standing wave' effect[60], [61]. The standing wave effect occurs when various electromagnetic waves interact within the sample, causing either constructive or destructive interference, leading to large spatial variations in  $B_1$ .

Similar to VSI-ASL, inhomogeneity in the  $B_1$  and  $B_0$ -field can also affect the labeling efficiency of other ASL-techniques. Much is still unknown about the performance of flow-based ASL-techniques in the kind of field conditions found in body. Next to affecting labeling efficiency, field inhomogeneity can also affect the readout. In ASL, single-shot echo-planar imaging (EPI) is often used as readout. EPI is a fast readout, making it relatively insensitive to motion, which is especially important for body applications. However, the speed of EPI comes at the cost of a sensitivity to  $B_0$ -field offsets, especially in the phase-encoding direction, because of limited gradient strength in this direction.

## READOUT METHODS

Segmented 3D turbo spin echo (TSE) or gradient- and spin-echo (GRASE) approaches have been recommended for brain ASL[13]. This is mainly because they enable optimized background suppression for the whole FOV, instead of only the first couple of slices, as is the case in 2D multi-slice EPI. In kidney, due to limited clinical experience with 3D readouts, 2D spin-echo echo planar imaging (SE-EPI) is recommended[62], despite its sensitivity to field-inhomogeneity.

Spatio-temporal encoding (SPEN) is a readout technique that is more robust to field inhomogeneity than EPI, while keeping similar readout times[63]. In SPEN, a frequency swept pulse is used in combination with a gradient, which imparts a quadratic phase profile[63]. The result is that resonance frequencies are spread out over the FOV. So contrary to EPI, not all locations will get excited at the same time. Thus each location will experience the excitation gradient for a specific time, leading to a specific phase-build up after excitation[64]. A refocusing pulse, followed by blips of an acquisition gradient will then sequentially unwind the phases belonging to specific parts of the FOV, leading to a signal that is spatially encoded in time. Because the signal in time is already directly proportional to the spin density at a certain location, there is no need for Fourier analysis.

SPEN is usually applied in the direction equivalent to the phase-encoding direction in EPI. An important advantage of SPEN is that it enables use of a stronger acquisition gradient compared to EPI [63], see appendix chapter 4. In addition, by choosing the proper timings, all points will get  $T_2^*$  refocusing[63], instead of only the center of k-space as is the case in EPI, see the appendix of chapter 4. These properties make SPEN more robust to field inhomogeneity than EPI. So, it would be interesting to see whether SPEN can be used in conjunction with ASL, especially when considering body applications or patient groups with implants. See appendix chapter 4 for formulas and theoretical background on SPEN.

## CLINICAL APPLICATIONS OF ASL

Although ASL is still traditionally seen as a brain technique, numerous body applications have started to emerge[18], [19]. In this work, we will explore the application of ASL in kidney and breast cancer.

In kidneys, perfusion provides the driving force for glomerular filtration, and thus the metabolic activity of the kidneys, as well as delivery of oxygen and nutrients to support general organ function [18]. Furthermore, hypoxia as a result of inadequate blood supply has shown to be associated to the initiation and progression of acute kidney injury (AKI) and chronic kidney disease (CKD)[18]. Being able to measure the perfusion of kidneys locally thus has great potential for the clinic, and would allow to study these diseases better. However, the use of contrast agent is restricted in patients with severe CKD, AKI or in patients who previously experienced severe reactions to GBCAs[27]. In addition, multiple contrast-enhanced measurements within a short time frame are not recommended, since retention of contrast agent remains a concern[27]. ASL provides a non-contrast enhanced alternative for renal perfusion measurements. The relatively short acquisition time and the fact that it does not require administration of contrast agents make repeated measurements possible, enabling monitoring

of perfusion over time, for example to study drug or treatment response[18]. At this point, FAIR or pCASL with a coronal oblique orientation of the imaging slices is recommended[62]. But transit time artefacts, and in particular planning of the labeling slab complicate the use of spatially-selective ASL in kidneys [62]. Flow-based ASL provides a transit time insensitive alternative that does not require planning of the labeling slab.

Also in breast cancer there is a clear potential for flow-based ASL. Screening for breast cancer with mammography has reduced breast cancer mortality with approximately 30% [65]. However, the sensitivity of mammography is limited, especially in the high-risk population[66]–[68]. In addition, mammography has a tendency to be less sensitive to aggressive tumor subtypes[69]. Breast MRI on the other hand, has a sensitivity approximately twice as high as mammography for breast cancer detection, a good specificity, and is specifically more sensitive to the detection of aggressive tumors[66], [69]. Breast MRI consists of a multi-parametric protocol, with as main workhorse DCE-MRI. Tumors require growth of new vessels, i.e. angiogenesis, to grow larger than 2-3mm<sup>3</sup>[70]. DCE-MRI can measure this increase in perfusion, as well as the increase in vessel permeability, making it especially sensitive to aggressive tumor types[66]. However, compared to mammography, breast MRI is expensive; the main contributors being the required staff, because of the time required for administration of contrast agent, the length of the examination, and cost of the contrast agent itself[71]. High costs lead to the decision to recommend breast MRI only for the high-risk population[65], [71], [72]. Women who fall in this high-risk category, e.g. carriers of the BRCA1 and/or BRCA2 mutation, get annual breast MRI for screening from the age of 30[65]. However, because of the cumulative effect of gadolinium retention with every GBCA-administration[73], and because the vast majority of these women are healthy, a non-contrast enhanced alternative would be very valuable. If ASL proves to be sensitive to breast lesions, it has the potential to prevent gadolinium retention and to lower costs, which could even open up the possibility for breast MRI screening in the average-risk population.

Previous studies have shown feasibility of FAIR implementations in breast, although in a single slice setting[74]–[77]. Because the labeling takes place outside the field-of-view (FOV), the distance labeled blood needs to travel is reduced in single-slice imaging. The main feeding artery of the breast, i.e. the internal mammary artery, has a blood flow of approximately 19cm/s[44], while the main feeding artery of the brain, i.e. the carotids, have a blood flow of approximately 39cm/s[78]. So it is likely that, because of the slow flow in breast, multi-slice FAIR would suffer from significant SNR loss due to increased transit delays. Flow-based ASL can provide a transit-time insensitive alternative, by labeling directly within the imaging region, thereby potentially enabling whole-breast coverage.

## THESIS OUTLINE

This work focusses on technical challenges concerning various aspects of ASL image acquisition in body applications. As motivated above, flow-based ASL methods have a lot of potential for body applications. First, a more general aspect of VS-ASL was studied, which was not necessarily limited to body applications. Blood velocity changes constantly as a function of the cardiac cycle, so it was hypothesized that the amount of label that is generated with velocity-selective ASL would be dependent on the phase of the cardiac cycle at which flow-based labeling is applied. This was studied in brain and is discussed in **Chapter 2**. Secondly, to investigate which flow-based ASL technique has the best performance, a comparison was made between four flow-based ASL techniques. Because different conditions apply in terms of e.g. field homogeneity, this comparison was done both in brain and kidney. Results of this study are discussed in **Chapter 3**. Thirdly, after successful application of flow-based ASL in kidney, the feasibility of velocity selective ASL was studied in breast cancer patients, to study whether enough contrast is generated to pick up hyper-perfusion in breast cancer lesions. Results of the study are shown in **Chapter 4**. When applying ASL in the kidneys and breast, it became apparent the EPI readout lead to subtraction artefacts in these applications, due to inhomogeneity of the  $B_0$ -field. **Chapter 5** discusses the technical feasibility of combining ASL with Spatial Temporal Encoding (SPEN) readout to enable a more robust readout. Lastly, the study in kidneys also demonstrated issues related to  $B_1$ -sensitivity of the background suppression pulses and VSI-ASL module. **Chapter 6** describes simulations of different non-selective inversion pulses, and VSI-ASL labeling and control modules, to find out how they perform under field conditions as they are found in body, and whether more robust alternatives can be found.





# Chapter 2

---

## **Influence of the cardiac cycle on velocity selective and acceleration selective arterial spin labeling.**

---

S.L. Franklin, S. Schmid, C. Bos, M.J.P. van Osch.

<sup>1</sup>C.J. Gorter Center for High Field MRI, Department of Radiology,  
Leiden University Medical Center, Leiden, The Netherlands

<sup>2</sup>Center for Image Sciences, University Medical Centre Utrecht, Utrecht, The Netherlands

<sup>3</sup>Leiden Institute for Brain and Cognition, Leiden University, Leiden, The Netherlands

## ABSTRACT

**Purpose:** In this study, the influence of the cardiac cycle on the amount of label produced by a velocity-selective (VSASL) and acceleration-selective arterial spin labeling (AccASL) module was investigated.

**Methods:** A short-PLD sequence was developed where a single VSASL- or AccASL-module was preceded by pCASL labeling to isolate the arterial blood pool. ASL subtraction was performed with label/control images with similar cardiac phase and time-of-measurement, followed by retrospective binning in ten cardiac phase bins. ASL signal variation over the heart cycle was evaluated and tested for significance using a permutation test.

**Results:** VSASL and AccASL showed significant arterial signal fluctuations over the cardiac cycle of up to respectively ~36% and ~64%, mainly in areas containing large arteries. pCASL also showed significant signal fluctuations, of up to ~25% in arteries. Raw label/control images confirmed that the observed signal fluctuations were caused by the amount of label produced during the cardiac cycle, rather than inflow-effects, since the raw images did not all show equal cardiac phase dependence.

No significant effects of the cardiac cycle were found on the gray matter ASL-signal.

**Conclusion:** Significant influence of the cardiac cycle on the generated label was found for spatially non-selective ASL-sequences. Hence, in order to become independent of the cardiac cycle, sufficient averages need to be taken. Alternatively, these findings could be highly interesting for the purpose of quantifying pulsatility more distally in the vascular tree.

# INTRODUCTION

Arterial Spin Labeling (ASL) is a non-invasive MRI technique allowing quantitative perfusion measurements by magnetically labeling arterial blood. In traditional ASL, blood proximal to the imaging volume is magnetically altered in the label image, followed by a post-labeling-delay (PLD) where the labeled blood flows into the imaging region. By subtracting this label image from a control image in which the inflowing magnetization is unaltered, static tissue signal is removed and only perfusion signal is left.

However, in traditional ASL transit delay artefacts can arise when not all of the labeled blood has reached the imaging volume during the PLD, thereby leading to underestimation of the perfusion and occurrence of vascular artefacts. In velocity-selective (VSASL) and acceleration-selective ASL (AccASL) blood is not labeled based on location, but based on flow velocity and acceleration, respectively. This implies that labeling is also performed within the imaging volume, thereby reducing tissue transit-delay artifacts[49]. The VSASL-module creates label by saturating spins above a certain cut-off velocity[49], or in case of Fourier-transform based velocity selective inversion (FT-VSI), inverting spins below the cut-off velocity[53]. The AccASL-module creates label by saturating spins above a certain cut-off acceleration/deceleration[51]. By labeling closer to the target region, VSASL and AccASL offer not only advantages in patients with slow-flow, but also in functional MRI (fMRI) experiments where ASL is used as readout[79], [80].

However, since velocity and acceleration of blood varies over the cardiac cycle, it is our hypothesis that the amount of label generated will depend on the cardiac phase in which the VSASL- or AccASL-module is applied. Previously, the cardiac cycle has already been shown to influence signal stability in other ASL techniques, such as pulsed-ASL[81], [82] and pCASL[83]. Inflow of fresh blood[83] as well as transit time[81], [82] have been mentioned as mechanisms through which the cardiac cycle influences signal stability. In case of VSASL and AccASL it is important to know whether the cardiac cycle has a significant effect on the amount of label that is generated to allow correct quantification and interpretation of these techniques, as well as to maximize temporal SNR, which can be considered especially important for functional applications[79]. In the current study the effect of the cardiac cycle on the amount of label that is produced is examined by using only a *single* VSASL(AccASL)-module with a short PLD, in combination with pCASL pre-pulse to limit the saturation-effect of the VSASL- and AccASL-modules to *arterial* blood, thereby avoiding contamination by venous signal.

In summary, the aim of this study is to investigate whether the amount of label generated by a VSASL- or AccASL-module depends on the cardiac phase during which the labeling takes place.

# METHODS

## General approach

Both VSASL- and AccASL-modules consist of motion sensitizing gradients, which are switched-on in label condition and switched-off in control condition. The VSASL gradients have alternating polarity, creating label by saturating spins above a certain cut-off velocity, whereas the AccASL gradients all have a positive polarity resulting in saturation above an acceleration threshold. Subtracting label from control thus generates signal from the saturated spins, i.e. the spins above the cut-off velocity(acceleration).

The original VSASL-sequence consists of two VSASL-modules with the same cut-off velocity: the first module is either in label or control condition, whereas the second module is played out after a PLD of 1-2 seconds and is always in label (velocity crushing) condition. The purpose of the second module is to provide a well-defined end to the bolus, enabling quantification, and to remove the venous component of the VSASL signal. The original AccASL implementation consists of only a single AccASL-module, since it inherently has very limited venous labeling[51].

To study the influence of the cardiac cycle it is important to be able to control the timing of labeling with respect to the cardiac cycle. This means that the effects of a *single* VSASL(AccASL)-module on the arterial blood pool need to be isolated. However, using only a single VSASL-module would result in a mixture of arterial and venous signal and, since arterial and venous systems overlap at tissue level, it would be very hard to isolate the labeled arterial blood using an arterial or venous mask. Therefore, a pCASL-preparation was used to first isolate the arterial signal, which was subsequently saturated by the spatial non-selective single VSASL(AccASL)-module, see Figure 1. Before adopting this experimental design, we also employed the same approach in a prospectively triggered fashion, see Supporting Information Figure S1. The prospectively triggered sequence had a very long pCASL-labeling duration (>7s), to become insensitive to differences in labeling duration. However, results of this approach were inconclusive, see Supporting Information Figure S2 and S3. Details of the methods and results of this experiment are reported in the Supporting Information.

Combining pCASL and a single VSASL- or a AccASL-module in one sequence yields four control/label conditions, since both the pCASL- and VSASL(AccASL)-module can be in label or control condition, see Figure 1B. Our main parameters of interest are VSArt and AccArt, see Figure 1C, which represent the amount of pCASL label, i.e. arterial blood, that is saturated by the VSASL- or AccASL-module. VSArt and AccArt are calculated by subtracting the pCASL image with VSASL- or AccASL-crushing from a regular pCASL image. Other possible subtractions and their interpretations, are described in Figure 1C. Whereas our analysis focuses on

VSArt and AccArt-images as a function of cardiac phase, single-VSASL(AccASL) images will also be shown to allow evaluation of the effectiveness of the pCASL pre-pulse to isolate the arterial blood pool, nevertheless it should be noted that the single-VSASL(AccASL)-image will partially contain venous signal. In addition, the pCASL images will be shown to provide information on cardiac phase dependence of label generation by pCASL.

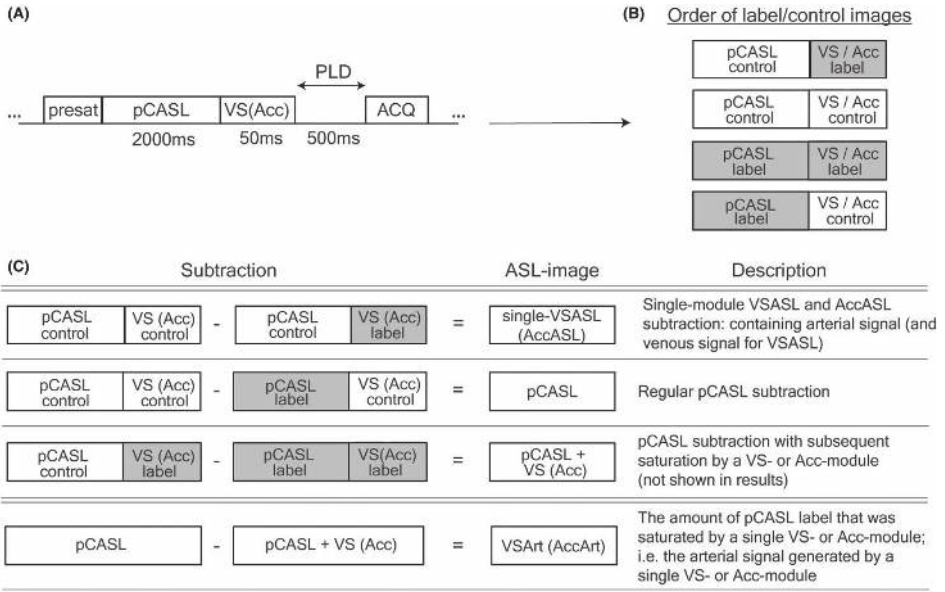


Figure 1 A) Sequence diagram for the scans combining pCASL and a VSASL- or AccASL-module. B) Order of label/control conditions for four consecutive acquisitions, this was repeated 200 times. C) Subtractions of the label/control images and their descriptions.

## In-vivo experiments

In total fourteen healthy volunteers were scanned, seven (22–56 years, 3 men and 4 women) with pCASL-VSASL, and seven (19–59 years, 3 men and 4 women) with pCASL-AccASL. All volunteers were screened for MRI contra-indications, and provided written informed consent. Cardiac phase was recorded continuously using a peripheral pulse unit (PPU) on the finger of the volunteer. A PPU-triggered phase-contrast quantitative flow scan, planned on the internal carotid arteries (at the location of the pCASL labeling), was acquired in order to measure blood flow velocity as a function of cardiac phase and to be able to measure the delay in occurrence of the R-peak as measured by PPU and maximum velocity at labeling location. For post-processing a 3D T<sub>1</sub>-weighted scan was acquired to obtain a gray matter mask, and a whole-brain phase-contrast angiography (PCA) scan was acquired to allow the generation of an arterial mask.

## MRI acquisition parameters

Scans were acquired on a Philips 3T MRI scanner (Ingenia CX, Philips, Best, The Netherlands) using a multi-slice single-shot EPI readout and a 32-channel head coil.

The ASL scans were acquired with a TR/TE of 3204ms/16ms, and 200 repetitions per label/control condition, resulting in a total scan time of 43 minutes. Presaturation of the imaging region was employed before pCASL-labeling using a WET-pulse[84]. The labeling duration of pCASL was set to 2000ms, which is longer than the average tissue arrival time[85] to make sure that pCASL-signal filled the whole arterial side of the vasculature and to minimize any influence of the cardiac cycle on the distance that label will travel into the (micro)vasculature. The VSASL cut-off velocity was set to 1.9cm/s and the AccASL cut-off acceleration to 1.3m/s<sup>2</sup>. Background suppression pulses were applied during pCASL labeling at 50 and 1150ms. See Table 1 for all scan parameters. A relatively short PLD of 500ms was chosen to reduce cardiac phase dependent effects on the transport of label, i.e. transit delay, as well as cardiac phase dependent inflow from ‘fresh’ spins which did not experience presaturation, while still ensuring enough time for VSASL(AccASL)-gradient induced eddy currents to decay.

Parameter	ASL scans	
Voxel size	3x3x7mm <sup>3</sup>	
Number of slices	17	
TR	3204ms	
TE	16ms	
Number of repetitions	200 (per label/control condition)	
Background suppression pulses	50/1150ms	
Total scan time	43 minutes	
Post-labeling delay	500ms	
pCASL labeling duration	2000ms	
	<b>VSASL</b>	<b>AccASL</b>
Labeling module duration	50ms	50ms
Gradient duration	0.8ms	0.8ms
Gradient strength	17mT/m	30mT/m
Cut-off velocity/acceleration	1.9cm/s	1.3m/s <sup>2</sup>

Table 1. Scan parameters for the retrospectively triggered ASL scans.

The phase-contrast quantitative flow measurement was PPU-triggered and acquired using a single slice 2D-FFE readout, with a TR/TE of 13/8.0ms, retrospectively reconstructed in 15 heart-phases, with voxels sizes of 0.6/0.6/6mm, and a phase-contrast encoding velocity of 200cm/s, resulting in a total scan duration of 2 min 57 s. In addition, a whole-brain PCA scan was acquired using a 3D-FFE readout, with a TR/TE of 20/4.0ms, reconstructed voxel sizes of 1.1/1.1/1.75mm, and a phase-contrast encoding velocity of 30cm/s, resulting in a total scan

duration of 53 s. The 3D- $T_{1w}$  scan was acquired using a multi-shot 3D-TFE readout, with a TR/TE of 9.7/4.6ms, using reconstructed voxel sizes of 0.9/0.9/1.2mm, resulting in a total scan duration of 4 min 57 s.

## Postprocessing

ASL images were realigned (SPM 12, University College London, London, United Kingdom) and data analysis was conducted using MATLAB R2015b (The MathWorks, Inc., Natick, MA, United States of America). In regular ASL, label and control images are acquired in an interleaved fashion to prevent subtraction errors arising from scanner drift. In the current study not only scanner drift but also cardiac phase needed to be taken into account. Since the four label/control images were not triggered on cardiac phase, no predefined, sequentially acquired label-control pairs with the same cardiac phase were available for subtraction. Thus, images with similar times of measurement as well as cardiac phase needed to be found to perform the subtractions. Suitable images for subtraction were created by performing Gaussian-weighted averaging within the “time-of-measurement/cardiac phase”-plane, see Figure 2. A Gaussian kernel was moved over the plane with a step size of  $\pi/5$  in cardiac phase direction and  $36*TR$  in time-of-measurement direction, to obtain a grid of  $22 \times 10$  data points for each label/control condition. The Gaussian kernel was designed such that it had a full-width-half-maximum of a step size, leading to blurring of half a step size in both directions;  $18^\circ$  (i.e.  $\pi/10$ ) in cardiac phase direction and  $18*TR = 58$  seconds in time-of-measurement direction. Subtractions between the label/control conditions were performed per grid point, and then averaged per cardiac phase bin.

Arterial and gray matter masks were generated to be able to obtain separate gray matter- and arterial signal curves. To this end, the pCASL image was co-registered separately to the  $T_1$ -based gray matter segmentation and the whole-brain PCA scan. The inverse transformation matrix was consequently applied to respectively the  $T_1$ -based gray matter segmentation and PCA scan, which were then both reformatted to the same space and resolution as the ASL images (all performed in SPM12). A vascular mask was generated by thresholding of the whole-brain PCA scan. Next, an arterial mask was generated by selecting only those voxels in the vascular mask that had an intensity above a manually-determined threshold on the mean pCASL image. A gray matter mask was generated by segmenting the 3D  $T_1$ -weighted scan (SPM12). Lastly, voxels from the gray matter segmentation that were also part of the vascular mask were removed. The arterial and gray matter mask were used to generate separate arterial and gray matter signal intensity curves of all ASL images as a function of cardiac phase.

The phase-contrast quantitative flow scan provided blood flow velocity curves over the cardiac cycle relative to the moment of PPU-trigger detection, allowing temporal alignment of label generation to the cardiac cycle and corresponding blood flow velocities. From the PPU-



triggered phase-contrast quantitative flow scan, the delay in occurrence of the R-peak measured by the PPU and maximum velocity at the pCASL-labeling location, was calculated. The R-peak delay was used to correct the cardiac phase of the blood flow velocity curves as well as the ASL data points, which were then plotted on a scale of zero to  $2\pi$  to become independent of the heart rate interval.

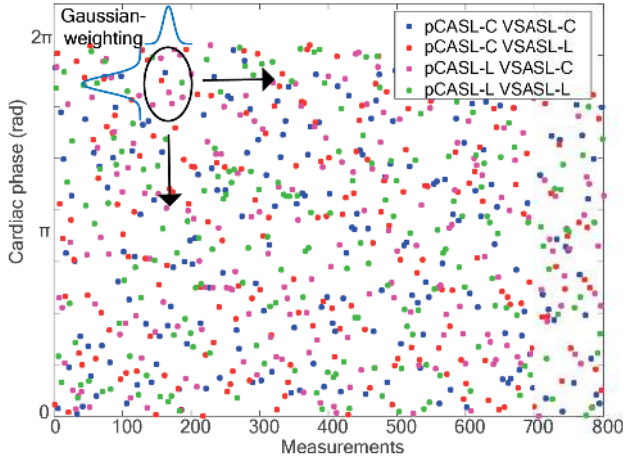


Figure 2. Averaging of the raw label/control images for the retrospectively triggered scans to obtain suitable subtraction of images with similar time-of-measurement and cardiac phase, to prevent subtraction errors from scanner drift and cardiac phase differences. Graph shows all the data points acquired in a single scan session. Four different raw images were acquired: pCASL<sub>control</sub>, pCASL<sub>label</sub>, followed by either VSASL<sub>control</sub> or VSASL<sub>label</sub>. The plot shows how a Gaussian-weighted average was taken of each of the four label/control conditions within the ellipse, which was moved over the “measurement time-cardiac phase” plane in 22 steps in time-of-measurement direction, and 10 in cardiac phase direction, to obtain a grid of  $22 \times 10$  data points for each label/control condition. Subtractions of the label/control conditions were performed per grid-point. Lastly, the data was averaged per cardiac phase bin.

To test whether the signal intensity fluctuations of the ASL images over the cardiac cycle were significantly larger than could be expected from the noise-level, a permutation test was performed where the cardiac phases were randomly reassigned to other data points before the Gaussian-weighted averaging step in the data analysis pipeline. Using the same permutations for all volunteers, the variance of the resulting signal intensity curves over the cardiac cycle ( $\text{Var}_{v,p}^{\text{norm},\text{random}}$ ) was calculated per permutation  $p$  and volunteer  $v$  and compared to the variance of the non-permuted data ( $\text{Var}_v^{\text{norm},\text{card}}$ ). In total 600 permutations were performed. Subject-specific  $\text{Var}_{v,p}^{\text{random}}$  values were normalized according to their average  $\overline{\text{Var}_v^{\text{random}}}$  over the 600 permutations allowing to pool data from all volunteers, resulting in a normalized  $\text{Var}_{v,p}^{\text{norm},\text{random}}$ . Next, a distribution was built by calculating the mean normalized variance over all volunteers per permutation  $\overline{\text{Var}_p^{\text{norm},\text{random}}}$ , representing the normalized variances that can be expected when data points are not sorted based on their correct cardiac phase. Based on this distribution, the percentile belonging to the actual measured mean normalized variance  $\overline{\text{Var}_p^{\text{norm},\text{card}}}$  over all volunteers (i.e. using the correct cardiac phase) was calculated. The measured fluctuations were deemed to be significant if the percentile was  $>95\%$  ( $\alpha$  of 0.05).

Analogous to Li et al<sup>8</sup> we examined the phase dependence of the raw label/control images to be able to rule out that the fluctuations in signal are simply caused by inflow of “fresh” spins that have not experienced presaturation. Should the fluctuations be caused by inflow of fresh spins, then the raw images would exhibit the same dependence on cardiac phase, since all will be affected similarly by fresh inflow, whereas difference in label generation would not affect all raw images in the same way.

## RESULTS

Figure 3 shows the perfusion-weighted images for: VSArt, single-VSASL, and pCASL at ten cardiac phase bins for a representative volunteer. Figure 4 shows the perfusion-weighted images for AccArt, single-AccArt and pCASL for a representative volunteer. The zoomed-in part shows that VSArt, AccArt, single-AccASL and pCASL have minimal signal in the superior sagittal sinus, the main draining vein of the brain, while single-VSASL does show some signal there. The difference between VSArt and single-VSASL indicates the expected venous labeling for single-VSASL, and shows that isolation of arterial signal in VSArt by use of pCASL as a pre-pulse was effective, see Figure 3. To focus on the signal variation over the cardiac cycle, the mean image over all cardiac phases was subtracted from the images, see Figure 5 and 6. The signal especially fluctuates in areas containing large arteries, which is supported by the signal intensity curves in Figure 7.

Results from the permutation test showed that the arterial signal variance over the cardiac cycle was significantly higher than expected by chance in most ASL images, (VSArt  $P = 0.017$ , AccArt  $P = 0.010$ , single-AccASL  $P = 0.047$ , pCASL (VS dataset)  $P = 0.015$  and pCASL (Acc dataset)  $P = 0.024$ ). Within the group of volunteers in which velocity-selective labeling was applied, a signal change up to  $\sim 36\%$  was found for VSArt, and  $\sim 26\%$  for pCASL in the arteries. Single-VSASL did not show significant signal fluctuations over the cardiac cycle ( $P = 0.202$ ), although a trend similar to the fluctuations of VSArt can be observed in Figure 7.

For the acceleration-selective experiments similar results were observed, with a signal change up to  $\sim 64\%$  for AccArt,  $29\%$  for single-AccASL and  $\sim 24\%$  for pCASL in arteries. Comparing the signal fluctuations with the blood flow velocity and acceleration shows that the blood flow velocity peak seems to coincide with the signal intensity peak of VSArt and pCASL, while the AccArt and single-AccASL peak is more similar to the peak in blood flow acceleration. The signal variance over the cardiac cycle in gray matter was not significantly increased.

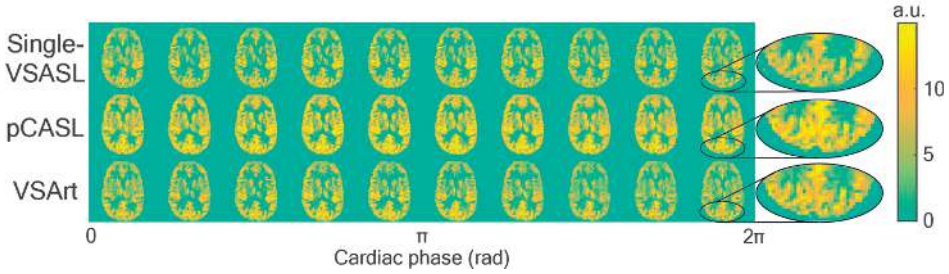


Figure 3. Perfusion-weighted images over the cardiac cycle of a representative volunteer for VSASL. The first row represents single-VSASL, the second row pCASL, the third row represents VSArt, i.e. the single-VSASL confined to the arterial blood pool as obtained by subtracting pCASL+VS (not shown) from regular pCASL (row 2). A zoom-in of the ellipse is shown to highlight the presence of venous signal in the sagittal sinus for single-VSASL, in contrast to pCASL, VSArt, single-AccASL, and AccArt.

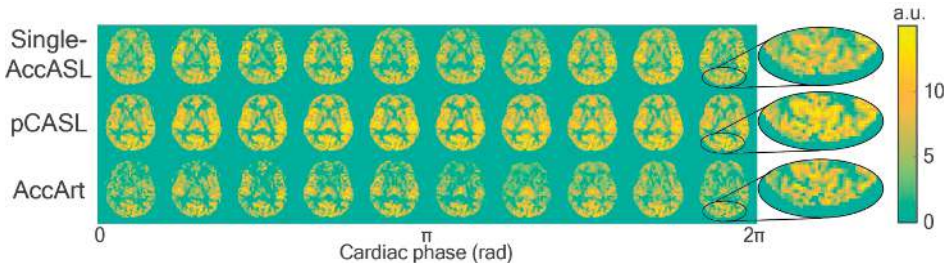


Figure 4. Perfusion-weighted images over the cardiac cycle of a representative volunteer for AccASL. The first row represents single-AccASL, the second row pCASL, the third row represents AccArt, i.e. the single-AccASL confined to the arterial blood pool as obtained by subtracting pCASL+Acc (not shown) from regular pCASL (row 2). A zoom-in of the ellipse is shown to highlight the absence of venous signal in the sagittal sinus for single-AccASL, pCASL, and AccArt, in contrast to single-VSASL.

Figure 8 shows the intensity curves of the raw label/control images before subtraction. Averaged over all volunteers, a pattern emerges, if the pCASL- and VSASL-module are both in either label or control condition,  $[pCASL_{\text{control}} VSASL(AccASL)_{\text{control}}]$  and  $[pCASL_{\text{label}} VSASL(AccASL)_{\text{label}}]$  the signal shows less fluctuations than if either one of them is in label condition and the other in control,  $[pCASL_{\text{label}} VSASL(AccASL)_{\text{control}}]$  and  $[pCASL_{\text{control}} VSASL(AccASL)_{\text{label}}]$ , this is most prominently found for AccASL.

## DISCUSSION & CONCLUSIONS

VSASL and AccASL are two promising ASL-techniques with reduced transit-time artefacts, where labeling is done based on respectively spin velocity and acceleration as opposed to location as done in traditional ASL. The fact that labeling is performed based upon velocity and acceleration raises the question whether the amount of label that is generated will vary over the cardiac cycle. In this study, the effect of the cardiac cycle on label generation by a *single* VSASL- and AccASL-module was investigated.

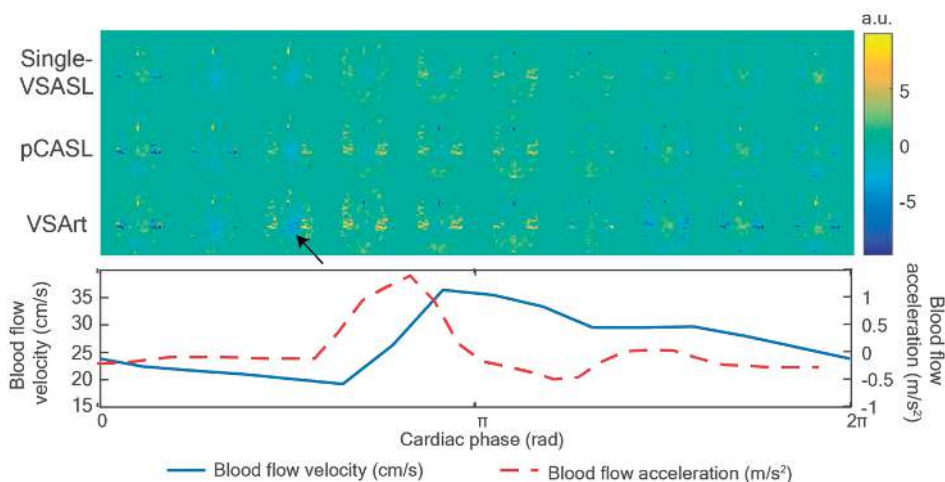


Figure 5. Perfusion-weighted images with the mean over the cardiac cycle subtracted for a representative volunteer for VSASL, showing the variation over the cardiac cycle with respect to the mean. Below, the corresponding blood flow velocity and acceleration are shown over the cardiac phases. Note that in these images negative signal means that the signal is below the average over the whole cardiac cycle. The first row represents single-VSASL, the second row pCASL, the third row represents VSArt, i.e. the single-VSASL confined to the arterial blood pool as obtained by subtracting pCASL+VS (not shown) from regular pCASL (row 2). Arrows indicate cardiac-dependent signal fluctuations in an area unrelated to perfusion, this signal is believed to stem from sub-optimal background suppression, see discussion. Bottom: corresponding blood flow velocity measurement in the carotid artery, as a function of cardiac phase.

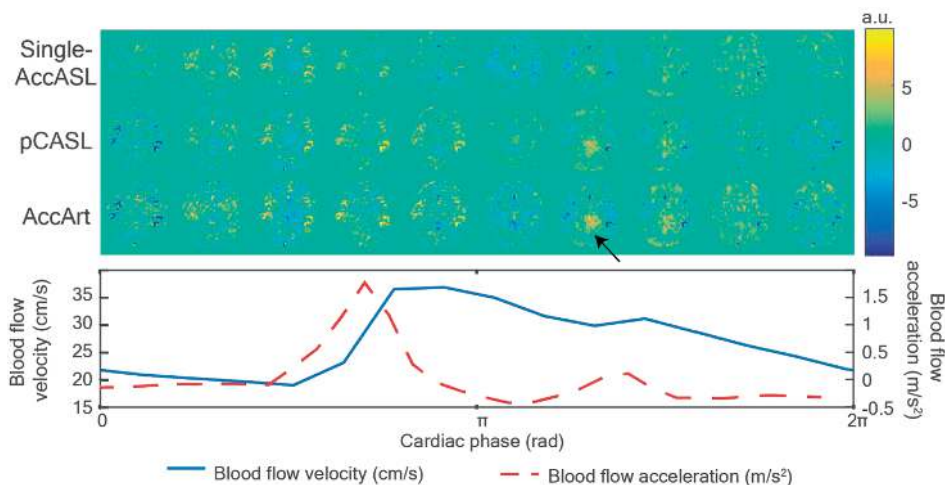


Figure 6. Perfusion-weighted images with the mean over the cardiac cycle subtracted for a representative volunteer for AccASL, showing the variation over the cardiac cycle with respect to the mean. Below, the corresponding blood flow velocity and acceleration are shown over the cardiac phases. Note that in these images negative signal means that the signal is below the average over the whole cardiac cycle. The first row represents single-AccASL, the second row pCASL, the third row represents AccArt, i.e. the single-AccASL confined to the arterial blood pool as obtained by subtracting pCASL+Acc (not shown) from regular pCASL (row 2). Arrows indicate cardiac-dependent signal fluctuations in an area unrelated to perfusion, this signal is believed to stem from sub-optimal background suppression, see discussion. Bottom: corresponding blood flow velocity measurement in the carotid artery, as a function of cardiac phase.

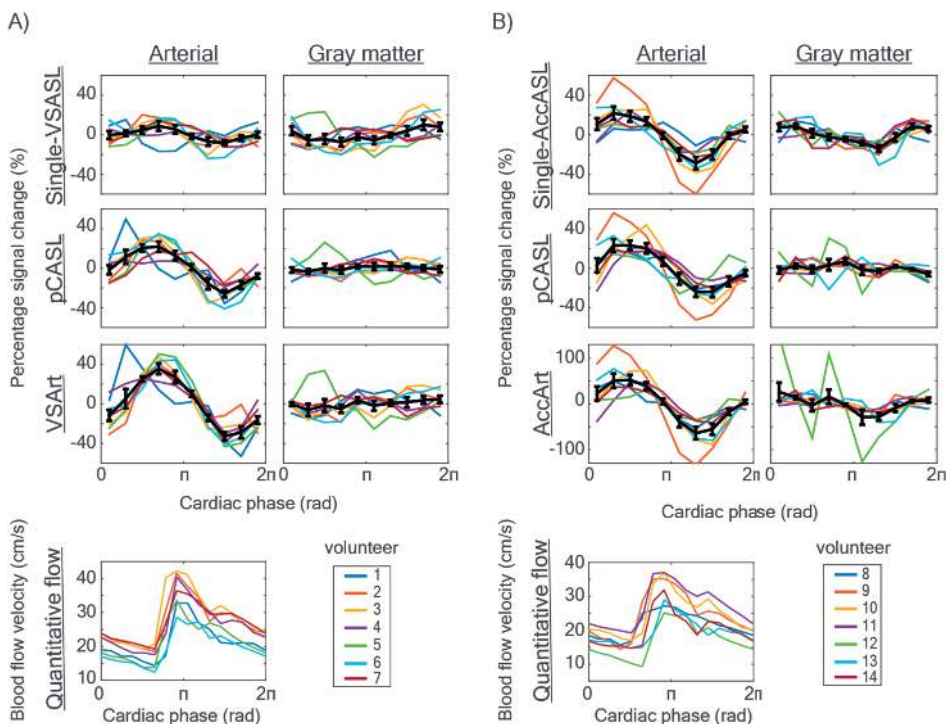


Figure 7. Signal intensity curves for A) VSASL and B) AccASL, over the ten cardiac phase bins. Left column: using arterial mask, right column: using gray matter mask. From top to bottom; the first row represents single-VSASL(AccASL), the second row pCASL, the third row represents VSArt(AccArt), i.e. the single-VSASL(AccASL) confined to the arterial blood pool as obtained by subtracting pCASL+VS(Acc) (not shown) from regular pCASL (row 2). All results are aligned according to the volunteer-specific blood velocity peak in the quantitative flow measurement, shown in the last row. Results are shown for all seven volunteers in each group. The black line in each graph represents the mean signal over the volunteers, with error bars indicating the standard error of the mean. Note that the y-axis scale of AccArt deviates from the rest. Volunteer 12 from the AccASL-dataset showed deviating signal fluctuations in the gray matter; however, exclusion of this volunteer from the analyses, neither affected statistical findings nor changed our conclusions.

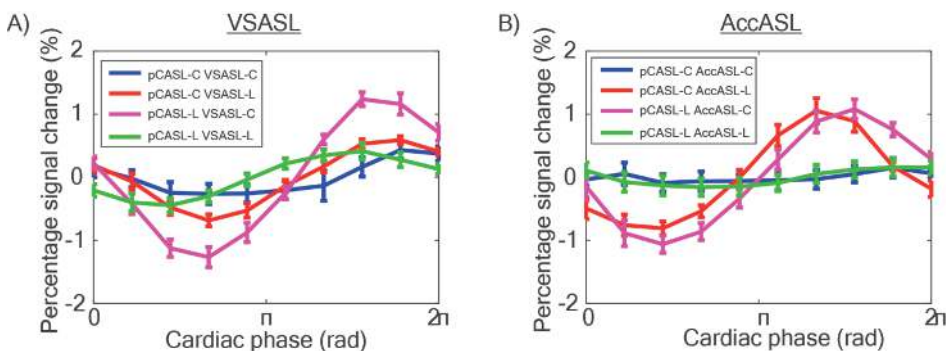


Figure 8. Arterial signal intensity plots of the four label/control images before subtraction; [pCASL<sub>control</sub> VSASL<sub>control</sub>], [pCASL<sub>control</sub> VSASL<sub>label</sub>], [pCASL<sub>label</sub> VSASL<sub>control</sub>] and [pCASL<sub>label</sub> VSASL<sub>label</sub>], of A) VSASL dataset and B) AccASL dataset. Mean intensity averaged over all volunteers is plotted, including error bars indicating the standard error of the mean. The label/control conditions are not all influenced equally by the cardiac cycle. Cardiac cycle fluctuation is less for the conditions with both pCASL and VSASL in label or control state ([pCASL<sub>control</sub> VSASL<sub>control</sub>] and [pCASL<sub>label</sub> VSASL<sub>label</sub>]), as compared to the conditions where either one of the two ASL-methods is in control state ([pCASL<sub>label</sub> VSASL<sub>control</sub>] and [pCASL<sub>control</sub> VSASL<sub>label</sub>]).

A sequence was designed to minimize cardiac-dependent effects on the signal by 1) inflow, 2) distance that the label travels into the vasculature, and 3) venous signal. Specifically, a single VSASL- or AccASL-module was combined with a pCASL preparation to limit its effect to the arterial blood pool. A short PLD was used to limit fresh inflow, and the pCASL-labeling duration was chosen longer than the average tissue transit time[85] to exclude influence of variations in the distance that label will travel into the microvasculature. Arterial label should intentionally be isolated for single VSASL(AccASL)-labeling since it also results in venous labeling, which in a regular VSASL sequence with two labeling modules is filtered out by the second labeling module. ASL images were retrospectively binned based on the cardiac phase during which labeling took place. Results confirm the hypothesis that VSASL(AccASL)-labeling of the arterial blood pool (VSASL/AccASL) depends on the cardiac cycle, where the AccASL signal showed higher signal fluctuations (up to 64%) than VSASL (up to 36%). In addition, pCASL (up to 25%), and single-AccASL (up to 29%) showed significant signal fluctuations over the cardiac cycle.

Effectiveness of the pCASL pre-pulse to isolate arterial signal is confirmed by the obtained VSASL and single-VSASL images. Single-VSASL, in contrast to VSASL, showed signal in the sagittal sinus, indicating the expected venous signal. Venous contributions can also explain why single-VSASL, in contrast to VSASL, did not show significant fluctuations over the cardiac cycle, since the venous signal will depend less on the cardiac cycle than the arterial part of the signal. Along the same lines, single-AccASL *did* show significant signal fluctuations since it has minimal venous labeling[51], further confirmed by the AccASL images of this study which hardly show signal in the superior sagittal sinus. However, single-AccASL still showed less signal fluctuations than AccASL, which suggests some additional signal contribution in the single-AccASL signal and possibly also in the single-VSASL signal, which is not cardiac-dependent and is filtered out using the pCASL-preparation, such as signal from diffusion-weighting caused by the VSASL- and AccASL-module[49], [51].

Results show that the peak in VSASL-signal coincides with the peak in blood flow velocity, indicating that signal fluctuations are not caused by inflow of 'fresh' spins, since then an inverse relation between ASL-signal and blood flow velocity would be expected. The observations support the hypothesis that at high blood flow velocity, more spins will flow faster than the cut-off velocity(acceleration), leading to an increase in signal. As would be expected, the AccASL-signal peak coincides more with the peak in blood flow acceleration. However, difference in timing between the peak in AccASL and VSASL-signal should be confirmed by performing VSASL and AccASL experiments in the same subjects. Finally, the peak in pCASL signal also coincided with the blood flow velocity peak; note that this timing is with respect to the end of pCASL-labeling. This means that the peak in pCASL-signal might be explained by an increase in the number of spins passing through the labeling plane (and therefore are inverted) at

end-of-labeling; moreover this effect will be enhanced due to minimal  $T_1$ -decay for spins at end-of-labeling. However, there is also a small effect of blood flow velocity on pCASL labeling efficiency[86].

Previous studies on the effect of the cardiac cycle on ASL have mainly focused on pulsed ASL and pCASL. Our findings confirm the general finding that cardiac influence seems to be largest in regions with large arteries[82], [83], [87]–[89]. Contrary to our results, Verbree et al[90] did not observe significant fluctuations in the pCASL signal based on the cardiac phase of end-of-labeling. This was probably due to a lack of power, because of limited averaging due to very long labeling durations and the lack of background suppression, similar to our prospectively triggered approach, described in Appendix 1. Using the retrospectively triggered approach, more repetitions could be acquired, and a significant effect of the cardiac cycle on pCASL end-of-labeling was observed.

Li et al[83] observed increased pCASL signal instability for a non-triggered sequence compared to a triggered-sequence based on the cardiac phase during the readout excitation-pulse. Using a PLD of 1800ms, Li et al[83] concluded that the pCASL-signal instability was most probably caused by cardiac-dependent inflow effects instead of label generation, since both label- and control-signal showed the same phase dependence over the cardiac cycle. In the current study, an effort was made to minimize inflow effects by using a shorter PLD of 500ms, not allowing ‘fresh’ spins to enter the imaging volume. Results show that the label/control images do not all have the same phase dependence, suggesting that the fluctuations of the signal are indeed caused by differences in the amount of label generated over the cardiac cycle, rather than inflow effects. The images where pCASL and VSASL(AccASL) are not in the same condition;  $[pCASL_{\text{control}} VSASL(AccASL)_{\text{label}}]$  and  $[pCASL_{\text{label}} VSASL(AccASL)_{\text{control}}]$ , show the highest cardiac dependence. This could be explained by the fact that label generation in both pCASL and VSASL are influenced by the cardiac cycle. A relatively high blood velocity at the start of the VSASL(AccASL) block leads to increased saturation by this module, so in case of the  $[pCASL_{\text{control}} VSASL(AccASL)_{\text{label}}]$  image a relatively low signal. Similarly, for pCASL, a relatively high blood velocity at the end-of-label will lead to an increase in inverted spins at end-of-label, so a relatively low signal for  $[pCASL_{\text{label}} VSASL(AccASL)_{\text{control}}]$ . Images where both pCASL and VSASL(AccASL) are in control-condition show less variation, indicating that there is minimal influence from inflow of ‘fresh’ spins from outside of the field-of-view. The image where both pCASL and VSASL(AccASL) are in label-condition also shows less cardiac dependence, which could be due to a cancellation of the two labeling-methods; the cardiac phase with a relatively high blood velocity, will lead to an increase in inverted spins at pCASL end-of-labeling, however, this increased inverted magnetization could in turn be saturated by the VSASL module, since more spins will have a velocity (acceleration) above the cut-off value, essentially reducing the cardiac dependence of the signal.

Some limitations should be considered when interpreting the results. Although careful consideration was given to limit confounding factors related to the cardiac cycle which might affect the data, it is possible that cardiac variations of the pCASL-signal influenced the VSArt and AccArt measurements, potentially resulting in an overestimation in the reported cardiac dependence of the VSASL and AccASL-signal. Importantly though, since VSArt(AccArt) is a subtraction of pCASL and pCASL+VS(Acc), not all of the pCASL cardiac dependence will be propagated. Specifically, all pCASL signal below the cutoff velocity(acceleration) will be subtracted out and it is expected that a large part of the bolus will be flowing below the cutoff velocity/acceleration since the pCASL labeling duration is longer than the average tissue arrival time[85].

Another limitation of the current study is that due to the 2D-readout, later-acquired slices will effectively have a longer PLD and will not have optimal background suppression. Sub-optimal background suppression of later acquired slices have possibly resulted in the cardiac phase-dependent signal fluctuations in an area unrelated to perfusion, shown in Figure 5 and 6. The signal seems to be in anti-phase with the vascular signal and in close proximity to main CSF structures, indicated by the arrows. Both features make it likely that CSF-flow is involved in these fluctuations, but the exact origin of this signal is not completely understood. This is in accordance with a recent study which showed increased physiological noise around the ventricular system for ASL, although in that study the noise seems to be located more centrally in the brain compared to our results[91].

In addition, the interpolation step (FWHM of Gaussian kernel is  $18^\circ$ ) as well as using a PPU-device instead of ECG for heart cycle recording will have introduced some smoothing of the data. The PPU could also have caused a small error in the cardiac phase if heart rate variability would have been high, since then the R-peak delay would have varied. However, heart rate variability during the scan session was found to be low (average standard deviation of RR interval = 0.11sec (VSASL) and 0.10sec (AccASL)), so we expect very minor effects on our conclusions considering the relatively low cardiac phase resolution of 10 cardiac phase bins. Lastly, it is likely that some partial volume effects will have been introduced by using arterial and gray matter masks during analysis (keeping in mind a slice thickness of 7mm). This will have led to some overestimation of the fluctuations in the gray matter accompanied by underestimation of fluctuations in the arteries, but these effects are expected to be relatively minor.

The finding that the amount of label generated by a VSASL(AccASL)-module fluctuates over the cardiac cycle is very interesting for understanding of the technique, the interpretation and quantification of it, and for optimizing SNR. For future studies, it would be interesting to investigate how cutoff velocity(acceleration) influences the cardiac phase dependence of the VSASL and AccASL-signal. By lowering this cut-off value, the label will be created further



into vascular tree, where pulsation might be decreased. However, investigating multiple cutoff velocities (accelerations) in the current study would have come at the cost of lower SNR and/or lower resolution over the cardiac cycle, when the total examination time would be kept constant. In addition, it would also be of interest to investigate whether VSASL or AccASL could be used to measure pulsatility in the microvasculature.

The pulse wave velocity has been known to increase with age, as well as in certain diseases, such as diabetes[92], and although the exact mechanism is still unknown, it has been associated with tissue damage in the brain[92], [93]. The current view is that the brain is very susceptible to the effects of increased pulse wave velocity because of the low vascular resistance of the brain, which exposes small capillaries to high-pressure fluctuations[92], [93]. The microvasculature will respond by increasing the resistance to limit the penetration of the pulsatility, but this may reduce blood flow and can lead to microscopic tissue damage[93]. Since microvascular disease is thought to be involved in strokes, dementia and white matter lesions[92], [93], it is thus very important to be able to measure the pulsatility in the microvasculature, something which only recently has been done in smaller penetrating arteries in a single slice using phase contrast MRI at ultra-high field[94].

In summary, this study has shown that the amount of arterial label generated by a single module of VSASL, AccASL, and pCASL can fluctuate up to respectively 36%, 64% and 25% over the cardiac cycle. By acquiring sufficient averages, this effect will be averaged out. Furthermore, the presented acquisition methodology could provide a valuable starting point for future measurement of the pulsatility at the tissue level, or at least more distally in the vascular tree than is currently possible.

## ACKNOWLEDGEMENTS

This work is part of the research programme Drag ‘n Drop ASL with project number 14951, which is (partly) financed by the Netherlands Organisation for Scientific Research (NWO). S.Schmid and M.J.P. van Osch are supported by the research program Innovational

Research Incentives Scheme Vici with project number 016.160.351, which is financed by the Netherlands Organisation for Scientific Research (NWO).

## SUPPORTING INFORMATION

In this paper, the influence of the cardiac cycle on the amount of label generated by VSASL and AccASL was investigated by retrospectively binning the images based on the cardiac phase at the start of the VSASL or AccASL-module. Before the retrospective method was designed a prospectively triggered method was implemented and tested, where placement of the VSASL and AccASL module with respect to the cardiac cycle was controlled using triggering. This supplementary material contains the design and results of this prospective method. Results were promising albeit inconclusive.

The methods were similar to what is described in the methods section in the main document. The main difference is that for these experiments the start of the VSASL(AccASL)-module and therefore the end of pCASL-labeling was triggered, see Supporting Information Figure S1 A. Five trigger delays were selected based on a quantitative flow phase-contrast scan performed at the pCASL-labeling location to be able to place the VSASL(AccASL)-module at five distinct cardiac phases (Supporting Information Figure S1 B). The trigger delays add an additional length to the pCASL-labeling. Since differences in labeling duration would overwhelm the effect of the cardiac cycle on VSASL(AccASL)-labeling, a very long pCASL-labeling duration of minimally 7 seconds was chosen to become independent of the extra labeling duration.

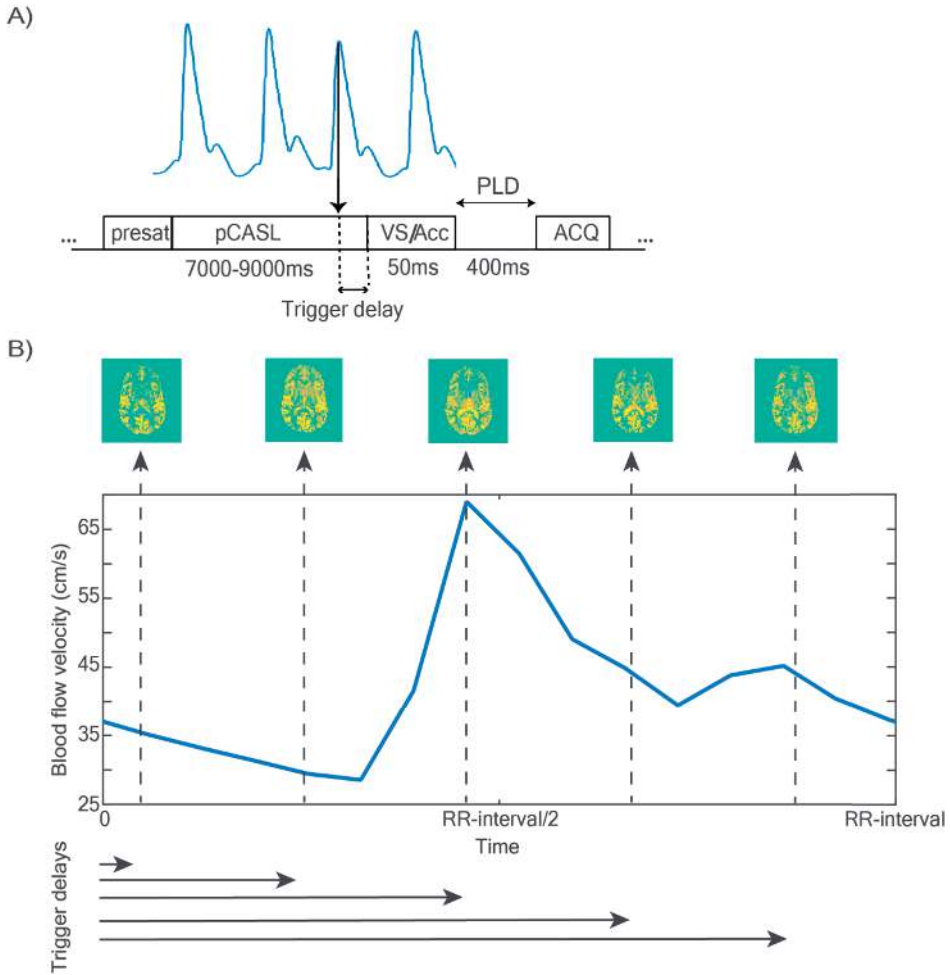
In total fifteen healthy volunteers were scanned with the prospectively triggered sequence, eight (21–35 years) with pCASL-VSASL, and seven (24–63 years) with pCASL-AccASL. In contrast to the study in the main document, considerably less averages could be acquired because of the long labeling duration of pCASL, i.e. 50 repetitions per label/control condition, resulting in a total scan time of 35 minutes. Because of the varying pCASL-labeling duration, no background suppression could be applied. Similar to the main study, a short PLD was chosen to avoid inflow of ‘fresh’ spins that did not experience pre-saturation. For the prospectively triggered study a PLD of 400ms was chosen.

Label/control images from the same cardiac phase were subtracted and averaged to obtain four ASL images, see Figure 1C in main manuscript. In contrast to the main experiments, the arterial mask was obtained by thresholding the mean pCASL-image.

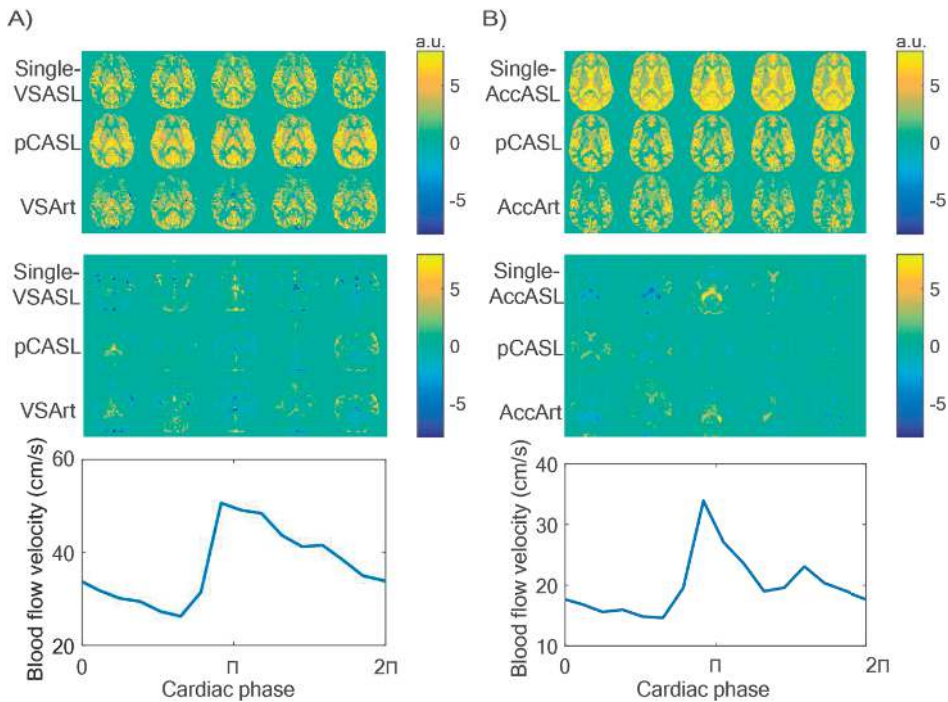
From the resulting images, main arteries can be distinguished, which show variation in signal intensity over the cardiac cycle, see Supporting Information Figure S2. Supporting Information Figure S3 shows the signal intensity curves for all images. A consistent phase dependence is visible for the single-VSASL and single-AccASL images in the arterial and gray matter mask, where the signal peak corresponds to the blood flow velocity peak. Signal curves of the other ASL images (pCASL, VSArt and AccArt) show a less consistent pattern across volunteers.

Inconsistency in results is probably due to a number of reasons, of which the most important one is the fact that few repetitions could be acquired because of the long pCASL labeling duration. Secondly, no background suppression could be applied because the prospective triggering approach introduced a varying sequence length. The effect of no background suppression is especially clear in the single-AccASL images in the top panel of Supporting Information Figure S2, which show high signal in white matter and ventricles. Thirdly, images were taken at only five different cardiac phases resulting in a coarse sampling of the cardiac cycle, making it difficult to uncover the exact shape of the cardiac phase dependence of the ASL-signal. Lastly, it is possible that due to the short PLD of 400ms there is still some instability in the signal due to residual eddy currents induced by the gradients in the VSASL- or AccASL-module. The retrospective method, described in the main section of this manuscript, was implemented to overcome these issues. With the retrospective method more averages could be acquired, background suppression could be used, the cardiac cycle could be sampled in ten steps instead of five, and we used a slightly longer PLD of 500ms to reduce influence of residual eddy currents; which resulted in a more consistent pattern over the cardiac cycle.

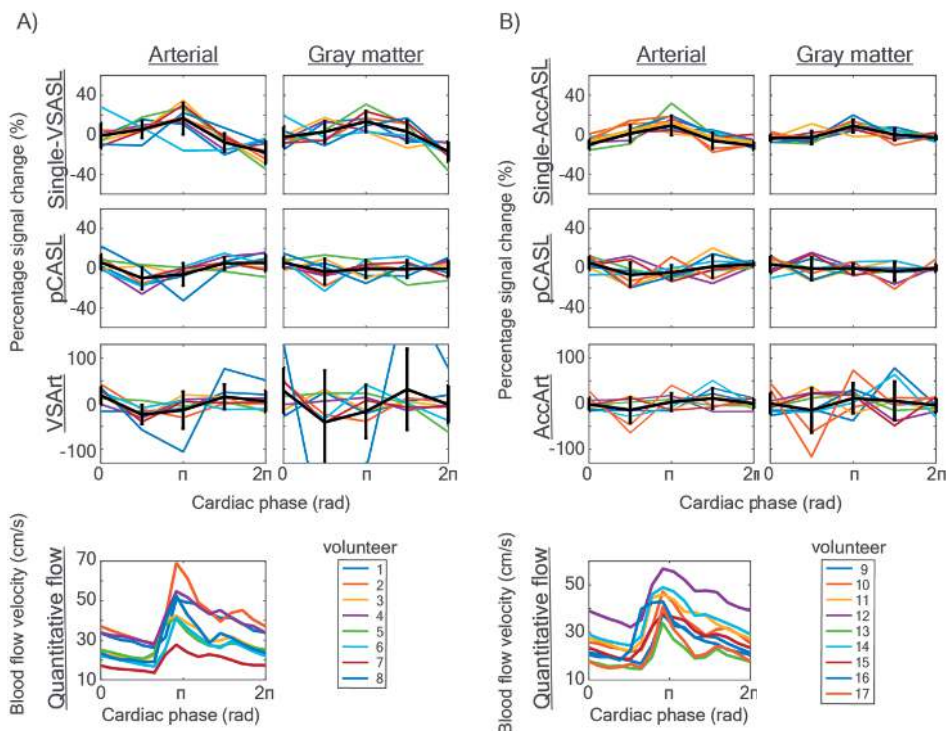
## SUPPORTING INFORMATION FIGURES



Supporting Information Figure 1. A) Sequence diagram for the prospectively triggered scans combining pCASL and a single VSASL- or AccASL-module. B) Pulse wave form as measured by a phase-contrast quantitative flow scan in the internal carotid artery at the level of the pCASL-labeling plane, used to calculate five trigger delays in the prospectively triggered scans. One trigger delay was defined on the peak of the graph, and the rest by dividing the cardiac cycle into five equal parts. Using these trigger delays, the ASL images are acquired at five different cardiac phases.



Supporting Information Figure 2. ASL images of the prospectively triggered experiments in a representative volunteer for VSASL (A) and AccASL (B), for the five cardiac phases. Top-row: original images, middle-row: images with the mean over cardiac cycle subtracted, note that a negative signal here means that the signal is below the mean signal over the whole cardiac cycle. Within each panel of images, the top row represents single-VSASL(AccASL), the second row pCASL, and the last row VSASL(AccArt); i.e. the arterial signal generated by the single VSASL(AccASL)-module as obtained by subtracting pCASL+VS(Acc) (not shown) from regular pCASL (row 2).



Supporting Information Figure 3. Signal intensity curves of the prospectively triggered data for A) VSASL and B) AccASL, over the five cardiac phases. Left column: arterial signal as obtained by using an arterial mask, right column: gray matter signal. From top to bottom; the first row represents single-VSASL(AccASL), the second row pCASL, the third row VSArt(AccArt); i.e. the arterial signal generated by the single VSASL(AccASL)-module as obtained by subtracting pCASL+VS(Acc) (not shown) from regular pCASL (row 2). All results are aligned according to the volunteer-specific blood velocity peak in the quantitative flow measurement, shown in the last row. Results are shown for all eight and nine volunteers in each group respectively. The black line in each graph represents the mean signal over the volunteers, with error bars indicating the standard error of the mean.



# Chapter 3

---

## **Multi-organ comparison of flow-based arterial spin labeling techniques: Spatially non-selective labeling for cerebral and renal perfusion imaging.**

---

S.L. Franklin<sup>1,2,3</sup>, I.K. Bones<sup>2</sup>, A.A. Harteveld<sup>2</sup>, L. Hirschler<sup>1</sup>, M. van Stralen<sup>2</sup>, Q. Qin<sup>4</sup>, A. de Boer<sup>2</sup>, H. Hoogduin<sup>2</sup>, C. Bos<sup>2</sup>, M.J.P. van Osch<sup>1,3</sup>, S. Schmid<sup>1,3</sup>.

<sup>1</sup>C.J. Gorter Center for High Field MRI, Department of Radiology, Leiden University Medical Center, Leiden, The Netherlands

<sup>2</sup>Center for Image Sciences, University Medical Center Utrecht, Utrecht, The Netherlands

<sup>3</sup>Leiden Institute for Brain and Cognition, Leiden University, Leiden, The Netherlands

<sup>4</sup>The Russell H. Morgan Department of Radiology and Radiological Science, Division of MR Research, Johns Hopkins University School of Medicine, Baltimore, Maryland, USA.



## ABSTRACT

**Purpose:** Flow-based arterial spin labeling (ASL)-techniques provide a transit-time insensitive alternative to the more conventional spatially-selective ASL-techniques. However it is not clear which flow-based ASL-technique performs best, and also, how these techniques perform outside the brain (taking into account e.g. flow-dynamics, field-inhomogeneity, organ motion). In the current study we aimed to compare four flow-based ASL-techniques (i.e. velocity selective ASL, acceleration selective ASL, multiple velocity selective saturation ASL, and velocity selective inversion prepared ASL (VSI-ASL)) to the current spatially-selective reference techniques in brain (i.e. pseudo-continuous ASL (pCASL)) and kidney (i.e. pCASL and flow alternating inversion recovery (FAIR)).

**Methods:** Brain (n=5) and kidney (n=6) scans were performed in healthy subjects at 3T. Perfusion-weighted signal (PWS-) maps were generated and ASL-techniques were compared based on temporal signal-to-noise-ratio (tSNR), sensitivity to perfusion changes using a visual stimulus (brain) and robustness to respiratory motion by comparing scans acquired in paced-breathing and free-breathing (kidney).

**Results:** In brain, all flow-based ASL-techniques showed similar tSNR as pCASL, but only VSI-ASL showed similar sensitivity to perfusion changes. In kidney, all flow-based ASL-techniques had comparable tSNR, though all lower than FAIR. In addition, VSI-ASL showed a sensitivity to  $B_1$ -inhomogeneity. All ASL-techniques were relatively robust to respiratory motion.

**Conclusion:** In both brain and kidney, flow-based ASL-techniques provide a planning-free and transit-time insensitive alternative to spatially-selective ASL-techniques. VSI-ASL shows the most potential overall, showing similar performance as the golden standard pCASL in brain. However, in kidney a reduction of  $B_1$ -sensitivity of VSI-ASL is necessary to match the performance of FAIR.

## INTRODUCTION

Arterial spin labeling (ASL) is a non-invasive technique which can be applied in various organs to measure tissue perfusion. Traditionally, ASL employs spatially-selective labeling of the blood to generate an endogenous tracer. In spatially-selective labeling techniques, label is created proximal to the region of interest (ROI), after which a delay is inserted to allow the labeled blood to travel from the labeling location to the ROI. The currently recommended spatially-selective ASL-technique in the brain is pseudo-continuous ASL (pCASL) [13].

However, quantification issues can arise due to the time it takes for the labeled blood to flow from the labeling location to the ROI, i.e. transit-time. For a subject with slow blood flow, transit-times can become so long that the label-signal has decayed before it reaches the ROI. Setting the transit-times to match the delay times would lead to severe signal-to-noise-ratio (SNR)-loss. While setting the delay times too short would lead to label still residing in the vascular compartment, making it impossible to discriminate between tissue that would be perfused later or tissue that would not be perfused at all, something which is often crucial for diagnosis or treatment selection.

Recently, a number of flow-based ASL-techniques have been introduced where blood is labeled based on its flow velocity or acceleration instead of spatial location. Flow-based ASL-techniques create label also within the ROI, making them less sensitive to transit-delays[43], [95]–[97]. Reduced sensitivity to transit-delays is especially valuable in cases where blood flow is slow, e.g. in elderly[98], patients with MoyaMoya disease[43], [95], [99] or in patients with renal artery stenosis[100], [101].

Moreover, flow-based ASL-techniques do not require planning of a spatial labeling volume, making it easier and more time-efficient to apply in practice. Planning of a spatial labeling volume can be especially challenging in the abdomen due to respiratory motion and (dynamic) field-inhomogeneities[13], [102], [103]. In the kidneys for example, ASL has been recognized as a promising tool to assess kidney function and identify pathology non-invasively[18], [100], [104], but planning of the labeling slab for renal ASL can be time-consuming and requirements for placement of the labeling slab can restrict the part of the kidney that is imaged[62]. Flow-based ASL can overcome these challenges, making it an interesting alternative to measure renal perfusion.

The first flow-based ASL-technique, which is partly based on early suggestions by Norris and Schwarzbauer[105], was proposed by Wong et al. (2006)[49]: velocity-selective ASL (VSASL) uses motion-sensitized gradients (MSGs) to saturate blood magnetization above a certain cut-off velocity in the label condition, generating ASL-signal based on the blood flow velocity.

VSASL was followed by acceleration-selective ASL (AccASL)[51], where signal is created based on differences in blood flow acceleration(deceleration) instead of velocity. In 2015, multiple velocity-selective ASL (mm-VSASL)[52] was proposed, in which additional velocity selective saturation (VSS)-labeling modules are used, to increase the amount of label created and thus increase SNR. Lastly, velocity-selective inversion prepared ASL (VSI-ASL) was proposed. VSI-ASL uses a Fourier-transform based velocity-selective pulse train to generate label based on inversion of magnetization[53], potentially doubling SNR compared to the saturation-based techniques. Whereas all of these techniques have their individual advantages and challenges, it is still unclear which technique is the most effective for perfusion measurements.

The aim of this study was to perform a direct comparison of these four flow-based techniques to the currently recommended spatially-selective labeling techniques. This comparison was made both for brain as well as for kidney applications since the use of ASL is no longer restricted to just the brain. Moreover, flow-based ASL is hypothesized to behave differently in brain and kidney, because of differences in flow-dynamics,  $B_0/B_1$  field homogeneity, and organ motion.

In brain, flow-based ASL-techniques were compared to pCASL, the golden standard in brain, based on temporal SNR (tSNR). In addition, sensitivity to identify perfusion changes was investigated using a visual task. In kidney, the flow-based techniques were compared to the recommended methods in kidney; pCASL and FAIR[62], based on tSNR. In addition, robustness to respiratory motion was investigated by performing all scans both in paced- and free-breathing. Moreover, this is to the best of our knowledge, the first time that AccASL, mm-VSASL, and VSI-ASL are applied in kidney.

## THEORY

Figure 1 shows the sequence diagrams for all flow-based ASL-techniques used in the current study. The VSASL-sequence uses VSS-labeling and control modules. VSS-modules consist of two adiabatic hyperbolic secant inversion pulses and two 90-degree hard pulses[49]. Labeling is based on MSGs. The MSGs are only present in the label-module, so that under the assumption of a laminar flow profile, the magnetization of spins flowing above a cut-off velocity is saturated[49]. The last VSS-module in the sequence, right before the image acquisition, has MSGs in both label and control-condition. It acts as a crusher for the labeled blood that has moved into the venous compartment and is accelerating, and labeled blood that is still flowing above the cut-off velocity in the large vessels; moreover, it results in a predefined temporal width of the bolus of labeled spins as required for blood flow quantification. Mm-VSASL uses the same VSS-modules, but has an additional label VSS-module (Figure 1d).

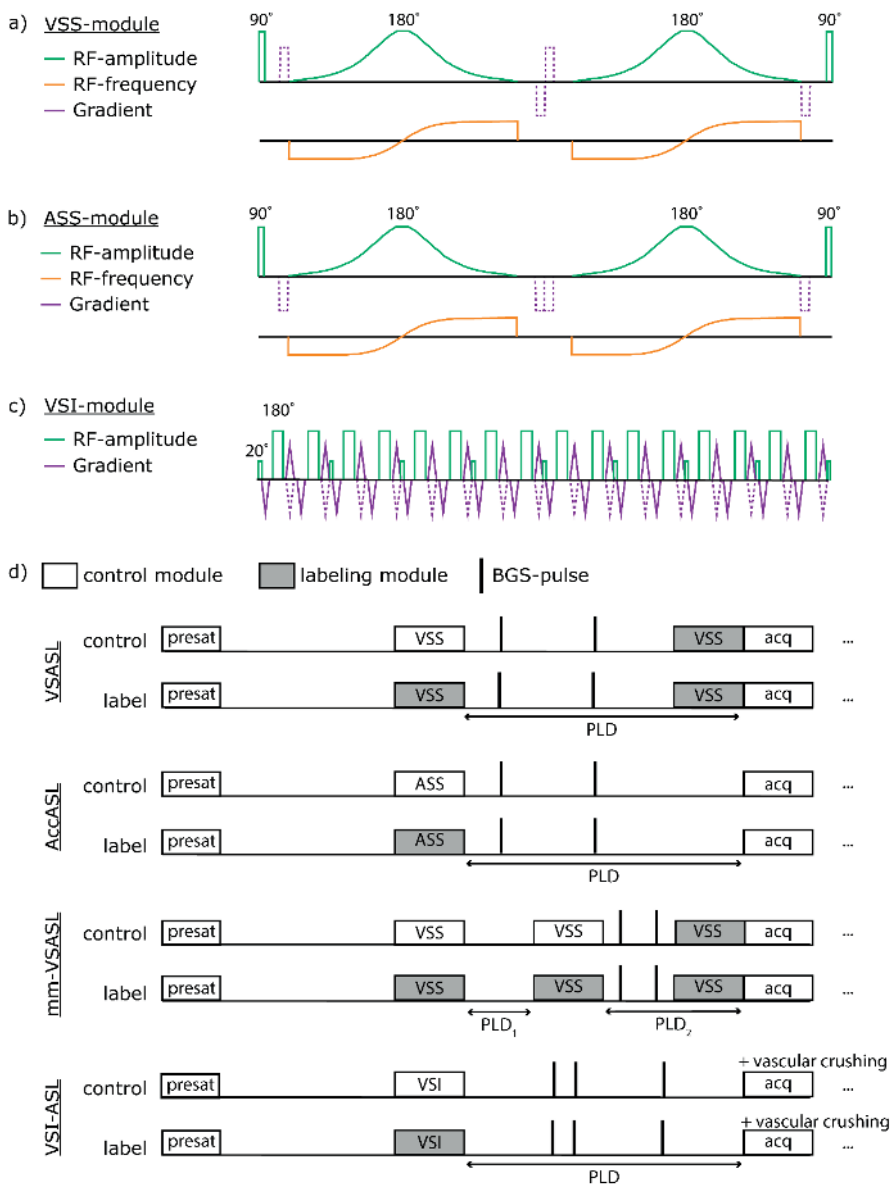


Figure 1. A) A velocity selective saturation (VSS) label/control module is shown, including two 90-degree hard RF-pulses, two adiabatic hyperbolic secant RF-pulses, and motion-sensitized gradients (MSG) in the label condition, as described in Wong et al.[49]. These VSS-modules are also used for mm-VSASL [52]. In B) an acceleration selective saturation (ASS) label/control module is shown, it consists of the same RF-pulses as in the VSS-module, only here the polarity of the MSG is only negative instead of alternating, as described in Schmid et al. [51]. Also for AccASL the MSG are only added in the label module. In C) a velocity selective inversion (VSI) label/control module is shown including nine 20-degree hard RF-pulses and sixteen phase-cycled 180-degree hard RF-pulses and eight sets of MSGs, as described in Qin and van Zijl[53]. In the label module the gradients have alternating polarity, while in the control module the polarity is solely negative. In D) Schematic sequence diagrams of the flow-based ASL-sequences; VSASL, AccASL, mm-VSASL, and VSI-ASL, incorporating the VSS, ASS and VSI-modules shown in a-c. Gray block represent the label modules, white blocks the control modules and the thick stripes represent the background suppression (BGS-) pulses. A WET module[84], [107] is used as presaturation (presat) and multi-slice single-shot GE-EPI is used for acquiring images (acq). Image is not drawn to scale.

AccASL uses acceleration-selective saturation (ASS-) modules. The MSGs in the ASS-modules are similar to ones in VSS-modules, albeit played out with a negative polarity, leading to a phase-dependence on spin acceleration(deceleration) instead of velocity (Figure 1b)[51]. By subtracting label from control signal, signal is generated only from the spins with an acceleration (or deceleration) above the cut-off[51], [106]. AccASL has not been implemented yet using a second labeling module[51]. This makes quantification of the AccASL-signal currently not possible, since the temporal width of the bolus would be unknown.

VSI-ASL is based on a slightly different principle. VSI-modules incorporate a Fourier-transform based velocity-selective pulse train in the form of nine 20-degree hard pulses in combination with sixteen phase-cycled 180-degree hard pulses to achieve inversion of the magnetization in small steps, see Figure 1c. Labeling of spins above the cut-off velocity is achieved by employing bipolar MSGs in the label-condition and negative polarity gradients in the velocity-compensated control-condition, see Figure 1d[53]. This leads to an inverted magnetization for spins flowing below the cut-off velocity during the label condition and an inverted magnetization of all spins during the control-condition[53]. In VSASL and mm-VSASL, a VSS-module right before image acquisition is used to crush the venous and vascular contribution to the ASL-signal and to enable quantification. In VSI-ASL, vascular crushing was enabled for the same purpose. Here the crushing of spins above the cut-off velocity is performed during the acquisition instead of right before. No major differences between the two approaches were found previously[49].

## METHODS

### Data acquisition

All flow-based ASL-techniques (VSASL, AccASL, mm-VSASL, VSI-ASL) were acquired in the brain and kidneys, and compared to the reference ASL-technique(s) in the respective anatomies.

Data was acquired on 3T Philips scanners and this study was performed with approval of the local institutional review board. Written informed consent was obtained from each subject before inclusion. Brain and kidney scans were acquired in separate scan sessions and separate subjects.

#### *Brain*

For brain, pCASL is currently the standardized ASL-technique[13], and was thus used as reference-technique. The brain scan sessions consisted of two conditions; all ASL-techniques were first acquired while the subject was watching a cartoon and a second time with eyes

closed. Within each condition the order of the ASL-techniques was randomized. The visual stimulus is expected to induce a perfusion increase in the visual cortex. By subtracting the perfusion signal during rest and visual stimulus, the sensitivity to detect small increases in perfusion can be measured for each ASL-technique.

Five healthy subjects (24-60 years, 2 male and 3 female) were included. Images were acquired using a 32ch-head coil and a multi-slice single-shot gradient-echo EPI acquisition. Image acquisition was planned in oblique transversal orientation, parallel to the corpus callosum in sagittal view. Scan parameters for VSASL, AccASL, mm-VSASL and VSI-ASL were chosen based on previous research[49], [51]–[53], see Table 1. The PLDs of flow-based ASL-techniques are usually shorter than those of spatially-selective techniques, since labeling takes place in or close to the microvascular bed. The PLD of flow-based ASL can, however, not be chosen too small, since the PLD also controls the bolus duration: only spins that have decelerated below the cut-off velocity during the PLD will contribute to the perfusion signal. mm-VSASL thus requires a slightly longer total PLD to also allow the spins saturated by the second module to decelerate. For the current study the PLD-settings were taken from the quoted literature.

The duration of the VSASL-, AccASL-, and mm-VSASL labeling modules were set to 50ms, to allow enough time for an adiabatic angle of 1500 degrees for the hyperbolic secant refocusing pulses. Gradient orientation for VSASL, AccASL and mm-VSASL was in the slice-direction i.e. feet-head direction. The number of repetitions was kept constant between all ASL-scans. Background suppression (BGS) using hyperbolic secant pulses was applied in all sequences, resulting in 85-90% suppression of tissue signal for the first slice. All ASL-techniques except for VSI-ASL employed two BGS-pulses. VSI-ASL employed three BGS-pulses to compensate the static-tissue inversion performed by the VSI-ASL modules. This makes sure that the static tissue signal is positive upon image acquisition. The exact BGS-pulse timings are reported in Table 1; defined from the end of the VSS-labeling module, and in case of mm-VSASL the end of the second VSS-labeling module. WET-presaturation[84], [107] was used to avoid spin history effects (Figure 1d), and the TR was adjusted to accommodate a 2s recovery of the WET-presaturation for all flow-based ASL-techniques. In case of pCASL, the WET-presaturation was placed right before labeling and thus did not require a TR-adjustment to accommodate regrowth of the magnetization.

A sagittal and coronal phase-contrast enhanced MRA localizer was used to aid planning of the pCASL labeling slab, using an encoding velocity of 40cm/s and a total scan duration of 54s. The pCASL labeling slab was planned perpendicular on the dorsal part of the vertebral arteries at the height of C1/C2.

An  $M_0$ -scan, for calibration of the ASL-signal, was acquired using the same acquisition as the ASL-scans with ASL-labeling turned off and using a TR of 10s. A 3D- $T_{1w}$  scan, for gray matter segmentation, was acquired using a multi-shot 3D-TFE acquisition, with a TR/TE of 9.7/4.6ms, acquisition voxel size of 1.2/1.2/1.2mm, resulting in a total scan duration of 5min.

### ***Kidney***

For kidney, both pCASL and FAIR are recommended[62], and thus both were used as reference-techniques. The kidney scan sessions consisted of two conditions; all ASL-techniques were first acquired in paced-breathing, and a second time in free-breathing. Within each condition the order of the ASL-techniques was randomized. In the paced-breathing condition subjects were asked to synchronize their breathing with the image acquisition, i.e. to perform a shallow breath in and out in between the acquisitions and to hold their breath briefly on exhalation during the acquisition. The researcher provided coaching for the first couple of breaths via the intercom. Subject cooperation was checked using a respiratory bellow for both breathing conditions. Robustness to breathing strategy was investigated by comparing the tSNR per unit time during paced- and free-breathing.

Six healthy subjects (23-30 years, 3 male and 3 female) were included. Images were acquired using a 28-element phased-array body coil and a multi-slice single-shot gradient-echo EPI acquisition. Image acquisition was planned in coronal-oblique orientation, parallel to the muscles anterior to the kidney, to minimize through-slice motion. Optimal scan parameters for renal imaging were not known for all flow-based ASL-techniques, so they were chosen partly based on previous research[36], [97], [108] and partly on preliminary experiments (Table 1). The durations of the VSS- and ASS-labeling modules were set to 50ms, and gradient orientation to the slice-direction, i.e. anterior-posterior direction, to minimize effects of respiratory motion on labeling[97]. FAIR was implemented as described in[108], including Q2TIPS[109] which was placed anterior to the imaging acquisition with a 10mm gap (Table 1).

For all ASL-scans the number of repetitions was kept constant. BGS using hyperbolic secant pulses was applied in all sequences, resulting in 85-90% suppression of tissue signal for the first slice. WET-presaturation[84], [107] was used to avoid spin history effects (Figure 1d) and saturation slabs were placed superior and inferior to the imaging volume to minimize fold-in artefacts. RF-shimming was performed on a volume shim box that covered the image acquisition volume with an additional 10mm on each side in the AP-direction.  $B_0$ -shim was set to automatic. A TR of 6500ms was used for the paced-breathing scans to keep the breathing-rhythm as natural as possible. For the free-breathing scans the TR was adjusted to accommodate a 3s recovery of the saturation slabs and WET-presaturation.

Scan parameter	VSASL[49]	AccASL[51]	mm-VSASL[52]	VSI-ASL[53]	pCASL[13]	FAIR[108]
<b>Brain</b>						
Voxel size (mm)	3x3x7	3x3x7	3x3x7	3x3x7	3x3x7	-
# slices	17	17	17	17	17	-
Recovery after presaturation (ms)	2000	2000	2000	2000	-	-
TR (ms)	4260	4260	4610	4160	4170	-
# repetitions	28	28	28	28	28	-
Total scan duration (min:s)	4:07	4:07	4:27	4:01	4:01	-
Post-labeling delay (ms)	1600	1600	[1150,820]	1500	1800	-
Background suppression (ms)	[50,1150]	[50,1150]	[20,620]	[560,580,1140]	[112,1350]	-
Cut-off velocity or acceleration	2cm/s	1.8m/s <sup>2</sup>	2cm/s	2.8cm/s	-	-
Duration labeling module (ms)	50	50	50	48	1800	-
# labeling modules	1	1	2	1	1	-
VS-crushing during or before acquisition (cm/s)	2	-	2	3	-	-
<b>Kidney [PB/FB]</b>						
Voxel size (mm)	3x3x6	3x3x6	3x3x6	3x3x6	3x3x6	3x3x6
# slices	5	5	5	5	5	5
Recovery after presaturation (ms)	4908/3000	4908/3000	4130/3000	4908/3000	-	-
TR (ms)	6500/4600	6500/4600	6500/5380	6500/4630	6500/6340	6500/4750
# repetitions	21	21	21	21	21	21
Total scan duration (min)	4:46/3:22	4:46/3:22	4:46/3:56	4:46/3:23	4:46/4:39	4:46/3:29
Post-labeling delay	1200	1200	[1150,820]	1200	1500	1400
Background suppression (ms)	[100,940]/ [100,925]	[100,940]/ [100,925]	[20,660]/ [20,650]	[350,650,1080]/ [350,650,1070]	[1520,2530]/ [1520,2530]	[500,1020]/ [500,1020]
Cut-off velocity or acceleration	5cm/s	1.4m/s <sup>2</sup>	5cm/s	5cm/s	-	-
Duration labeling module (ms)	50	50	50	48	1800	15
# labeling modules	1	1	2	1	1	1
VS-crushing during or before acquisition (cm/s)	5	-	5	5	-	-
Q2TIPS[109]: five 120mm saturation slabs evenly spaced	-	-	-	-	-	1200-1300ms

Table 1. Scan parameters used brain and kidney. For the bottom (kidney) panel; settings that differ between the paced and free-breathing scans are indicated as [paced-breathing]/[free-breathing]. For all scans hyperbolic secant pulses were used as background suppression pulses. Abbreviations: VSASL = velocity selective arterial spin labeling, AccASL = acceleration-selective ASL, mm-VSASL = multiple velocity selective arterial spin labeling, VSI-ASL = velocity selective inversion, pCASL = pseudo-continuous ASL and FAIR = flow alternating inversion recovery.



The flow-based ASL-techniques did not require additional planning of a labeling slab. For FAIR the selective labeling slab, and thus the imaging volume, was planned such that it excluded the aorta, to ensure labeling of the aorta. The pCASL labeling slab was planned perpendicular to the aorta. Care was taken to not place the pCASL labeling slab too inferiorly to minimize the chance of the kidneys moving into the labeling slab during breathing, and also not place it too superiorly to minimize negative effects on labeling efficiency from field-inhomogeneities at the air-tissue interface of the lungs.

In addition to the ASL-scans, an  $M_0$  and a  $T_1$ -map was acquired with the same planning as the ASL-acquisition. The  $M_0$ -scan was acquired in paced breathing for calibration of the ASL-signal, using the same acquisition as the ASL-scans, with ASL-labeling turned off and using a TR of 6500ms. The  $T_1$ -map was acquired for segmentation of kidney cortex and medulla. It was acquired using a cycled multi-slice inversion-recovery sequence[110] with 11 inversion times ranging between 42ms and 2030ms, and a multi-slice single-shot EPI acquisition. Resulting in total scan duration of 1min18.

A  $B_1$ -map was acquired in two subjects, and in one of these subjects an additional VSI-ASL scan was acquired without BGS, using 10 repetitions. These additional scans were acquired to investigate the origin of an artefact of VSI-ASL in kidney that became apparent during scanning. The  $B_1$ -map was acquired using a dual-TR method[111] with a TR of 30ms and 150ms, and a gradient spoil factor of 20. The  $B_1$ -map received the same planning as the ASL-acquisition. See the Supporting Information S1, and Supporting Information Figure S1 and S2 for these results and further simulations on the VSI-ASL artefact.

## Postprocessing

Using SPM12[112], the brain ASL-scans were first realigned and co-registered to the  $T_1$ w-scan, and later transformed to MNI space and smoothed (kernel width=8x8x8mm). Using Mevislab[113] (MeVis Medical Solutions AG, Fraunhofer MEVIS, Bremen, Germany), all kidney scans were co-registered to each other using a group-wise image registration method[114], separately for left and right kidney.

The ASL subtraction images ( $\Delta M_i$ ) were normalized by  $M_0$  and averaged over all  $n$  repetitions to obtain a perfusion-weighted signal (PWS) map and enable inter-subject comparison.

$$\text{PWS} [\%] = \frac{1}{n} \sum_{i=1}^n \frac{\Delta M_i}{M_0}$$

Voxel-wise tSNR was calculated by dividing the average ASL-signal over time ( $\mu_{\Delta M, \text{voxel}}$ ) by the standard deviation of the ASL-signal over time per voxel ( $\sigma_{\Delta M, \text{voxel}}$ ).

$$tSNR_{voxel} = \frac{\mu_{\Delta M, voxel}}{\sigma_{\Delta M, voxel}}$$

Whole-brain masks were created by thresholding the  $M_0$ -image, and whole-kidney masks were created by manually drawing kidney contours on the  $M_0$ -image. These masks were used for visualization. For the tSNR-graphs, gray matter masks were generated based on the  $T_1w$ - brain scans using the SPM12 Toolbox[112]; voxels with >70% gray matter were included in the mask. Cortex-/medulla-/ and high intense fluid masks were generated based on the kidney  $T_1$ -map using an intensity histogram to manually threshold the image. This study showed artefacts in the VSI-ASL kidney images in some subjects with the severity of the artefact varying greatly between subjects. To enable a fair comparison between results, individual artefact masks were manually drawn on the VSI-ASL images and the voxels inside the artefact mask excluded for the tSNR analysis of VSI-ASL. Additional scans and simulations on the VSI-ASL artefact in kidney can be found in the Supporting Information S1, and Supporting Figure S1 and S2.

### ***Statistical analysis***

For both the brain and kidney dataset, a repeated-measures ANOVA in combination with a Tukey post hoc test was applied to test whether there are significant differences in terms of tSNR between the different ASL-techniques, using  $P=0.05$ . Data is reported as mean  $\pm$  standard deviation (STD).

To study the effect of visual stimulation on brain PWS, a voxel-wise repeated-measures ANOVA was performed to test whether the PWS-values acquired during rest and during visual stimulation conditions significantly differed from each other. All PWS repetitions (without averaging) of all subjects were used as input, setting subjects as between-group factor. Analysis was performed after transforming the PWS-maps to MNI-space. A Bonferroni correction was applied to correct for multiple testing, resulting in  $P=2.6e-7$ .

The effect of breathing strategy was evaluated using tSNR per unit time, to compensate for the shorter TR of the free-breathing scans. The mean tSNR-values in cortex were divided by the square-root of the time it takes to acquire one label-control pair.

$$tSNR_{per\ unit\ time} [s^{-1/2}] = \frac{tSNR}{\sqrt{2 * TR}}$$

A paired Student's t-test was used to test whether the tSNR per unit time differed significantly between scans acquired in paced- and free-breathing, using  $P=0.05$ .

# RESULTS

## Brain

PWS- and tSNR-maps of a representative subject are shown in Figure 2. Comparison of PWS-maps between ASL-techniques showed that VSI-ASL had a similar spatial pattern as the reference sequence, i.e. pCASL. Mm-VSASL showed very high signal in CSF-rich areas. VSASL and AccASL also both showed higher signal in areas with CSF, although to a lesser degree than mm-VSASL.

Figure 3 shows the distribution over subjects of the mean tSNR in gray matter, for all ASL-techniques. VSASL, AccASL, mm-VSASL, VSI-ASL and pCASL all have similar mean tSNR in gray matter without significant difference ( $p > 0.05$ ), although the standard deviation of the tSNR over subjects is larger for VSASL and mm-VSASL (tSNR mean  $\pm$  standard deviation VSASL:  $1.07 \pm 0.52$ , AccASL:  $1.27 \pm 0.24$ , mm-VSASL:  $1.36 \pm 0.55$ , VSI-ASL:  $1.18 \pm 0.12$ , pCASL:  $1.10 \pm 0.09$ ).

Next, the ability to measure small increases in perfusion upon visual stimulation was compared between all ASL-techniques. VSI-ASL and pCASL detected the visual cortex most robustly, as evidenced by the highest number of voxels in the visual cortex that showed statistically significant increased PWS (Figure 4). VSASL, AccASL and mm-VSASL showed less power: less voxels showed significant increases in perfusion and p-values were higher.

## Kidney

One subject was excluded due to excessive through-plane motion during the scans, leaving five subjects available for analysis.

Figure 5a shows representative PWS-maps from one subject. The flow-based ASL-techniques all showed clear corticomedullary contrast with spatially homogeneous signal in the cortex region, similar to the two reference techniques, i.e. FAIR and pCASL. Between the flow-based techniques VSI-ASL and AccASL show a slightly higher PWS compared to the rest. In general though, flow-based techniques had a similar PWS-intensity as pCASL, but clearly lower than FAIR. The flow-based ASL-techniques displayed small abnormalities at locations that are part of the collecting system, indicated by the green arrows in Figure 5a. In addition, negative signal was sometimes observed in the medulla, especially for VSI-ASL.

A similar pattern was observed on group-level in the tSNR graphs of Figure 5b; all flow-based ASL-techniques showed a similar tSNR as pCASL, but significantly lower than FAIR in cortex (tSNR mean  $\pm$  standard deviation VSASL:  $1.59 \pm 0.21$ , AccASL:  $1.54 \pm 0.41$ , mm-VSASL:  $1.37 \pm 0.34$ , VSI-ASL:  $1.62 \pm 0.36$ , pCASL:  $1.79 \pm 0.56$ , FAIR:  $4.61 \pm 0.71$ ) ( $p < 0.05$ ) as

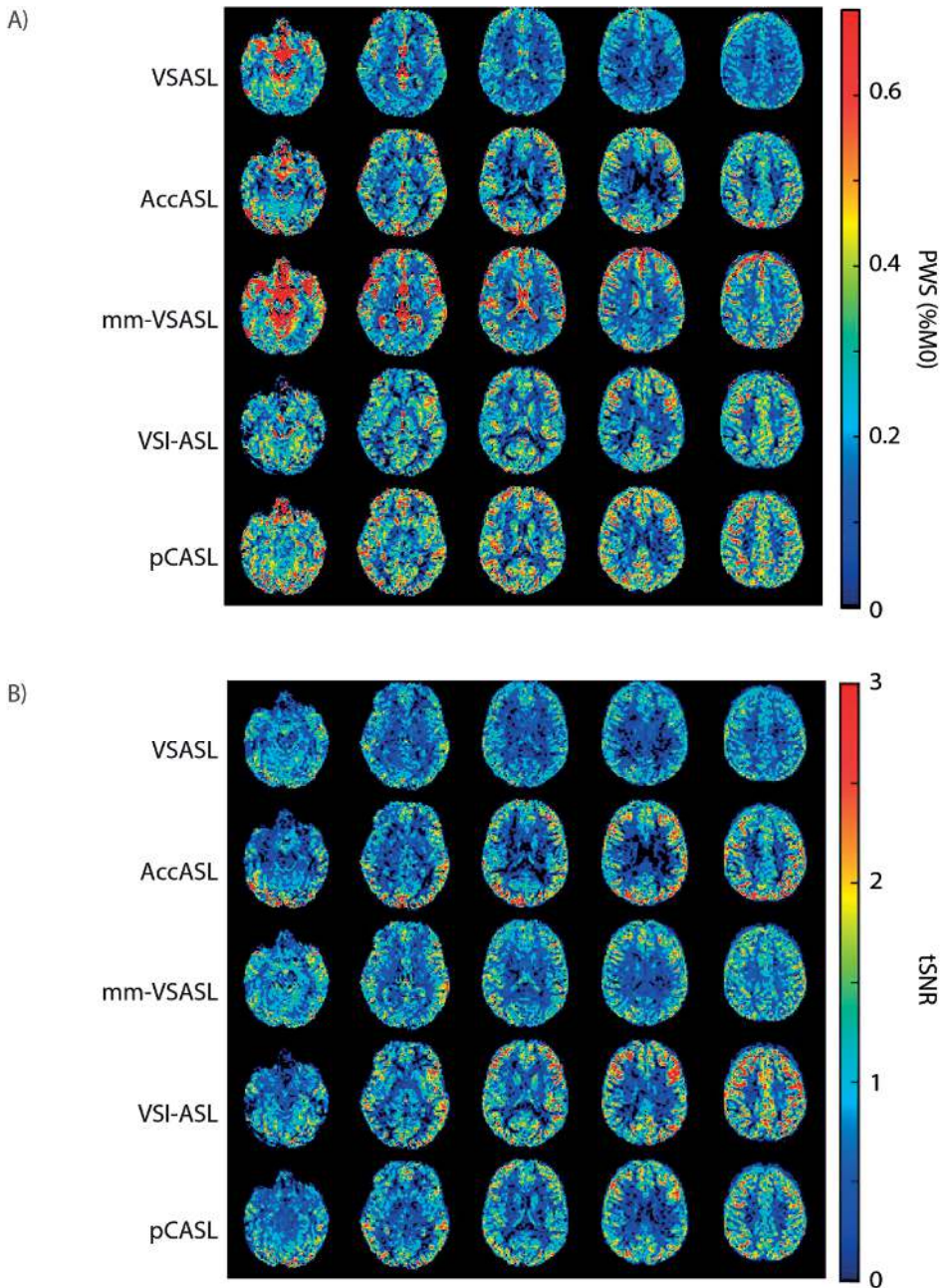


Figure 2. A) Brain perfusion-weighted signal (PWS-) maps of a representative subject. As expected, mm-VSASL and to a lesser extent VSASL and AccASL showed some  $T_2$ - and/or diffusion-weighting[43], [95], [96], illustrated by the high signal in areas rich in CSF B) Temporal signal-to-noise ratio (tSNR) maps of a representative subject.

well as medulla (VSASL:  $0.43 \pm 0.11$ , AccASL:  $0.66 \pm 0.09$ , mm-VSASL:  $0.50 \pm 0.06$ , VSI-ASL:  $0.17 \pm 0.14$ , pCASL:  $0.46 \pm 0.15$ , FAIR:  $1.42 \pm 0.55$ ) ( $p < 0.05$ ). The tSNR in the medulla is notably lower than in the cortex. Note that in the tSNR-graphs in Figure 5b voxels that are part of the VSI-ASL artefact mask were not taken into account for the VSI-ASL images, see Supporting Information Figure S3 for the tSNR graphs including all voxels.

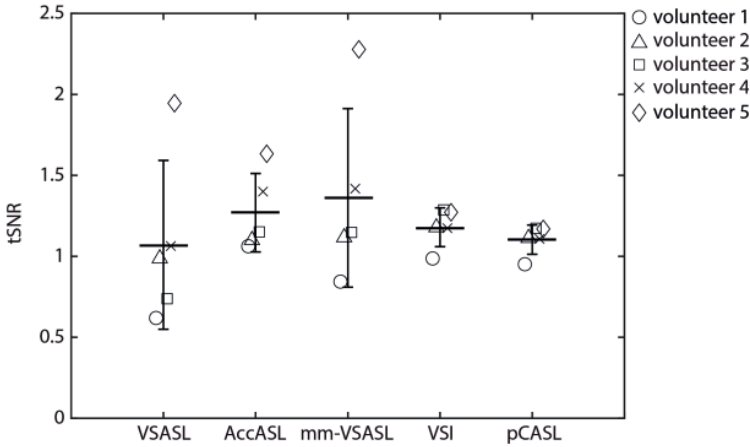


Figure 3. Distribution of mean temporal signal-to-noise ratio (tSNR) in gray matter over subjects, for all ASL-techniques. Middle bar represents the mean tSNR value over all subjects, and the vertical bars the standard deviation.

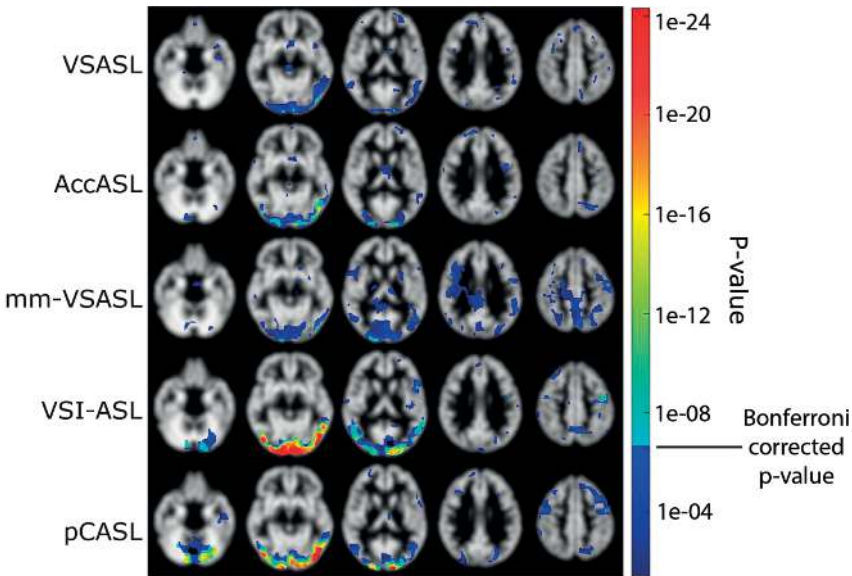


Figure 4. Visual activation maps of the brain averaged over all subjects, showing the voxels with a higher perfusion-weighted signal (PWS)-value during visual stimulus (watching cartoon) compared to rest (eyes closed). A Bonferroni correction was applied to correct for multiple testing, resulting in a significance level of  $P = 2.6e-7$ . Color indicates the P-value. Results are overlain on a gray matter segmentation. Five brain slices are shown.

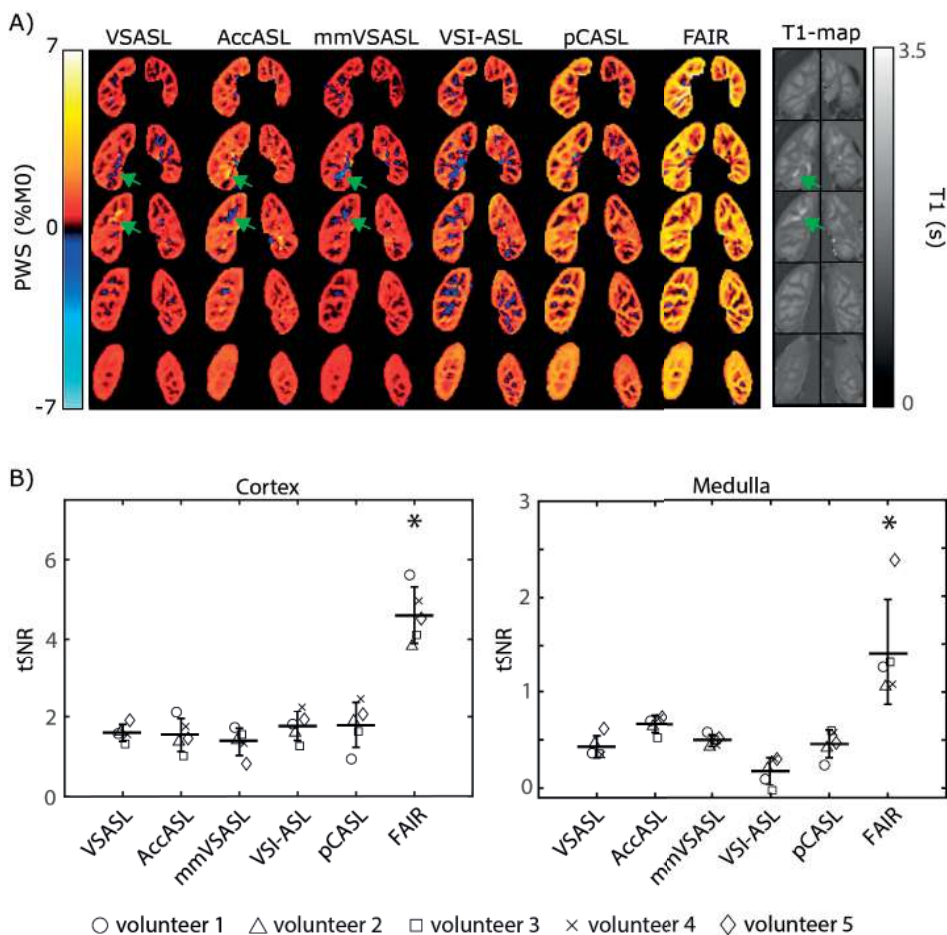


Figure 5. A) Kidney perfusion-weighted signal (PWS-) maps of a representative subject acquired during paced breathing. The green arrows indicate locations which are part of the collecting system, where the flow-based ASL-techniques displayed either intense positive or negative signal. B) Distributions of mean temporal signal-to-noise ratio (tSNR) in cortex and medulla over all subjects, for all ASL-techniques. FAIR had a statistically significant higher tSNR than all other ASL-techniques indicated by the asterisk ( $p < 0.05$ ), for both cortex and medulla. Note that for VSI-ASL the voxels that were part of the artefact mask were not taken into account.

Next, sensitivity of the flow-based ASL-scans to breathing strategy was investigated (Figure 6). VSASL, and AccASL both showed a reduction of  $\sim 14\%$  in mean tSNR per unit time for the free-breathing condition, while hardly any reduction of tSNR per unit time was observed for mm-VSASL and VSI-ASL (resp.  $< 0.01\%$  and  $-0.03\%$ ). However, none of the flow-based ASL-techniques showed a statistically significant decrease in tSNR per unit time. Only FAIR, showed a statistically significant lower tSNR per unit time for the free-breathing condition ( $P < 0.05$ ), although the difference was small  $\sim 14.2\%$ , see Figure 6.

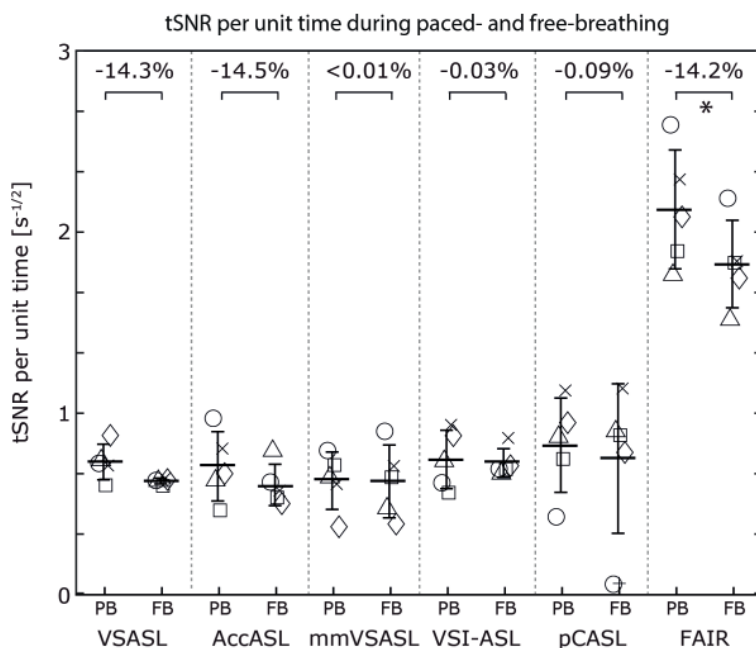


Figure 6. Temporal signal-to-noise ratio (tSNR) per unit time for all subjects in the kidney cortex, during paced- (PB) and free-breathing (FB). At the top the mean paired difference between paced and free-breathing tSNR per unit time is given in percentages. Only FAIR has a statistically significant lower tSNR per unit time during free-breathing, but this difference is small (-12.2%).

## DISCUSSION

This study has shown that flow-based ASL-techniques are feasible in both the brain and kidneys at 3T, enabling planning-free ASL-measurements with intrinsically reduced sensitivity to transit-time artefacts. In brain, results showed that all flow-based ASL-techniques had comparable robustness of the signal (tSNR) to the reference pCASL. However, only VSI-ASL showed similar sensitivity as pCASL for picking up small increases in brain perfusion. In the kidneys, all flow-based ASL-techniques showed similar PWS and good corticomedullary contrast. However, compared to the reference technique FAIR, all flow-based ASL-techniques had significantly lower tSNR. The flow-based ASL-techniques proved to be robust to respiratory motion when using image registration, enabling free-breathing acquisition.

In brain, a comparable tSNR was found for all flow-based ASL-techniques (VSASL, AccASL, mm-VASL, VSI-ASL) and pCASL. VSASL, mm-VASL and AccASL showed a higher variability of tSNR over subjects than VSI and pCASL, although this could mainly be attributed to a single subject. Further inspection showed that this subject had a deviating CSF-system compared to the other subjects, as can be seen in Supporting Information Figure S4a. Possibly partial volume effects in combination with the inherent diffusion-weighting of VSASL, Ac-

cASL and mm-VSASL, can explain the increased tSNR in this subject compared to the others. See Supporting Information Figure S4b for a representation of the ASL-data in the gray matter segmentation.

In comparison, previously, a significantly lower tSNR for VSASL was found compared to AccASL and pCASL[51]. Discrepancy in the results could be due to the use of a lower flip angle of the adiabatic refocusing pulses in Ref. 17 compared to the current study. In the current study, adiabatic refocusing pulses were used with a higher flip angle and with a slower rotation of the effective B<sub>1</sub>-field that better satisfied the adiabatic condition. This resulted in a 50ms VSS-labeling module instead of 30ms. The gains from improved adiabaticity outweighed the losses from increased T<sub>2</sub>-decay as a result of a longer duration.

Guo and Wong reported that ASL-signal of gray matter (treated as a direct indicator of spatial SNR) of mm-VSASL was significantly higher than VSASL, and was similar to that of pCASL[52]. In the current study tSNR was used to compare the different techniques instead of spatial SNR, to also take signal robustness into account. A similar tSNR for VSASL, mm-VSASL, and pCASL was found. When solely looking at the ASL-signal though, mm-VSASL did show a higher value than VSASL and pCASL, albeit with a larger standard deviation over time, see Supporting Information Figure S5. In addition, Guo and Wong used a BIR-8 implementation of VSASL[52], which has been shown to be more resistant to eddy currents and B<sub>1</sub>-inhomogeneities[57], [115], instead of the VSASL-implementation shown in Figure 1a. Qin and van Zijl (2016) reported a similar tSNR between VSI-ASL and pCASL[53], and comparable values were measured in the current study.

Results in the brain showed that all flow-based ASL-techniques have similar tSNR to pCASL. However, tSNR provides information on ASL-signal stability over time, but does not provide evidence on the sensitivity of the technique to detect small changes in CBF. To test this, a mild visual stimulus was given. From the flow-based ASL-techniques, VSI-ASL showed a similar sensitivity to pick up changes in perfusion as pCASL, confirming a recent perfusion weighted functional MRI study[79], whereas VSASL, AccASL and mm-VSASL showed less power. The reason why VSASL, AccASL and mm-VSASL showed lower sensitivity to detect CBF-changes compared to VSI, even though they have similar tSNR, is probably due to the fact that they are more prone to subtraction errors due to e.g. diffusion. These errors contribute to a high tSNR, but do not contribute to the visual activation map. This, together with previous findings that VSI-ASL produces similar CBF-maps as pCASL[53], implies that VSI-ASL is the most promising flow-based ASL-technique for brain applications.

Diffusion-weighting of the VSASL-, AccASL- and especially mm-VSASL-signal, visible as high signal in CSF-related areas, has also been observed in previous studies[49], [51], [52]. Diffu-



sion sensitivity of VSASL, AccASL and mm-VSASL is caused by the fact that the VSS- and ASS-labeling module contains motion-sensitizing gradients and the control module does not. The mm-VSASL signal is especially affected, possibly because of the additional VSS-labeling module. A diffusion correction should be applied when using VSASL or mm-VSASL for quantification[97], to prevent overestimation of the CBF. AccASL cannot be quantified at the moment, since the bolus duration is unknown[51].

In kidneys, tSNR was comparable for all flow-based ASL-techniques and pCASL. However, compared to FAIR, all flow-based techniques had a significantly lower tSNR in both cortex as well as medulla. VSASL was previously compared to pCASL at 1.5T, and a lower whole kidney tSNR for VSASL compared to pCASL was reported[97]. The discrepancy in results is likely caused by a higher  $B_0$ -inhomogeneity at 3T reducing the labeling efficiency of pCASL, thereby reducing the benefits of pCASL with respect to VSASL.

The observed lower tSNR for flow-based ASL-techniques compared to FAIR could be caused by a lower labeling efficiency of the flow-based ASL-techniques: possibly because of a higher sensitivity to field-inhomogeneity or because of the dependence on flow-direction. Labeling by flow-based ASL is only sensitive to flow in a single direction, as determined by the orientation of the labeling gradients. Labeling-directions were chosen based upon the primary directions of flow, and also orthogonal to the direction of respiratory movement to mitigate possible bulk-motion artefact, as has been observed previously[97]. Besides this, previous studies in both brain[49] and kidney[97] have found little dependence of the VSASL-signal on the labeling-direction for a cut-off velocity of  $<4\text{cm/s}$  and  $5\text{cm/s}$  in brain and kidney respectively. More research is necessary to be able to draw final conclusions the precise reason why FAIR performs better than flow-based ASL in the kidneys.

Although it was not the subject of the current study, the tSNR difference between the two standard techniques in kidney ASL: FAIR and pCASL, is noteworthy. We found a 3 times higher tSNR for FAIR compared to pCASL. Similar differences were found in a previous study[108], where a detailed discussion is provided on the reasons why pCASL performed worse than FAIR in kidney at 3Tesla, given that the opposite is true for the brain. Advantages of pCASL in brain include labeling closer to the imaging region and having a longer temporal bolus. However, these do not hold for kidneys. In the kidneys, the labeling plane of pCASL was planned 15cm above the kidneys and the temporal bolus of FAIR is increased since blood is labeled in most of the torso. This provides a possible explanation of the higher tSNR of FAIR that was found in this study. However, it is important to keep in mind that there are also downsides to using FAIR in kidneys. Coronal imaging is recommended for renal applications, so that through-slice motion due to respiration is minimized and blood is labeled closer to the kidney in the renal arteries. However, using coronal imaging comes with its own complications. First of

all, it is cumbersome to plan the selective labeling slab, since the aorta needs to be excluded. Secondly, coronal FAIR does not always allow full organ coverage, due to the constraint of excluding the aorta from the imaging region (between 54-80% of the kidney could be covered in the current study). This is why it is often used as a single-slice technique[62]. Flow-based ASL-techniques can provide a time-efficient alternative that guarantees whole organ coverage, albeit with lower tSNR.

In the current study a generally lower tSNR was found for kidney medulla compared to cortex, which was expected since the medulla has a lower perfusion than the cortex; only ~10% of renal blood flow reaches the medulla[18], [116]. However, the finding that FAIR has a significantly higher tSNR in medulla was not necessarily expected. Because of the longer transit times of medulla[108], one would expect that flow-based ASL-techniques are better suited to measure medullary perfusion than the spatially-selective ASL-techniques. However, it is likely that the cut-off velocity was still too high to label directly in the medulla. Unfortunately the cut-off velocity cannot be chosen lower than 5cm/s, without risking respiratory motion artefacts[97]. Nevertheless, results did show that the relative performance of flow-based ASL in the medulla was improved compared to that in the cortex.

Flow-based ASL in kidney also showed some artefacts in locations related to urine. This can be explained by the fact that while the ASL-module was played out, the collecting system will have high signal compared to kidney tissue, due to the short  $T_1$  of urine. Small motion or diffusion-weighting of the urine signal will subsequently generate subtraction artefacts that can either be positive or negative.

Results showed that respiratory motion only plays a small role for flow-based ASL in kidney, when using image registration. A reduction in tSNR per unit time was observed during free-breathing for all flow-based ASL-techniques, although it was not statistically significant for any of the techniques. Indicating that up to a certain point, the shorter TR of free-breathing scans compensate for the reduction in tSNR by facilitating acquisition of more repetitions. This is in line with the paper by Robson et al (2009)[117], where they conclude that rejection due to motion-artifacts during free-breathing acquisition is offset by being able to acquire more data in the same scan time. In contrast to Robson et al, in the current study a FFE-EPI acquisition was used and no repetitions needed to be rejected because of motion.

In practice, the limited reduction in tSNR per unit time is outweighed by the great improvement to patient comfort and practicability. An additional benefit of acquiring scans in free-breathing is that images will be acquired during every respiratory state, which gives a more representative sampling of the hemodynamic state.

This study has shown that the performance of flow-based ASL-techniques in kidney is still less convincing than in brain. In kidney, all flow-based ASL-techniques had a significantly lower  $tSNR$  than FAIR, while in brain flow-based VSI-ASL provides comparable performance to pCASL.

Given the results in brain, VSI-ASL holds the most promise to improve the performance of flow-based ASL in kidney. However, VSI-ASL in kidney showed severe subtraction artefacts in some individuals. Additional scans and simulations were performed to investigate the underlying cause, see Supporting Information S1 and Supporting Information Figure S1 and S2. Results indicate that the combination of suboptimal inversion of the static tissue by VSI-ASL and of the BGS-pulses is likely the cause of the negative tissue signal that were observed in low- $B_1$  areas. The precise underlying cause and possible solution for the VSI-ASL artefacts observed in kidney warrants further research.

This study has some limitations. First of all, during the paced-breathing condition subjects were asked to shortly hold their breath during the image acquisition, but not necessarily during labeling. However, effects are expected to be small since a cut-off velocity (5cm/s) was chosen to prevent subtraction artefacts due to respiratory motion, and our results indeed did not show the typical high-intensity subtraction artefacts as described by Bones et al[97]. In addition, VSASL- and AccASL-labeling have been shown to depend on the cardiac cycle[118]. Effects are expected to average out when using a sufficient number of averages, but will still lower  $tSNR$ -values.

Secondly, as mentioned before, the current study employed a VSASL-implementation as described by Wong et al.[49] instead of the BIR-8 implementation of VSASL[57], [115], which has been shown to reduce eddy current effects as well as sensitivity to  $B_1$ . However, when using a PLD of 1500ms and a cut-off velocity of 2cm/s, similar CBF-maps were produced for both VSASL-implementations[57], so this is not expected to have had a major effect on our data.

Thirdly, balanced pCASL was used as one of the reference techniques. Recently, optimized unbalanced implementations of renal pCASL were presented in a limited number of subjects, to reduce sensitivity to  $B_0$ -inhomogeneities[103], [119]. Using one of the optimized implementations could improve the performance of pCASL as reported in this study. However, a separate shimming area at the labeling location is used in our pCASL implementation, which will reduce off-resonance artefacts when using balanced pCASL.

In addition, the PLDs used in renal mm-VSASL as taken from literature, were optimized for brain applications. Possibly the renal PWS of mm-VSASL could be improved by optimizing the PLDs specifically for kidneys.

Lastly, perfusion data in this study was not quantified. The main focus of the study was to provide a comparison on the performance of techniques without too much emphasis on differences in tracer kinetics and modelling assumptions that would result in technique-specific scaling factors. By dividing by  $M_0$  inter-subject differences in scanner settings are accounted for and, without e.g. an additional subject-specific  $T_1$  and labeling efficiency measurement, quantification would only add a technique-specific scaling factor. Quantitative comparison would especially be interesting when a gold standard reference, like PET, would be available.

In conclusion, this study has shown encouraging results for flow-based ASL in both brain and kidney. Flow-based ASL thus provides a promising planning-free and transit-time insensitive alternative for spatially-selective ASL in subjects with slow flow. VSI-ASL, as flow-based ASL-technique, shows the most promising results. In brain, VSI-ASL has a similar performance as the standardized pCASL, although in kidney more technical development at 3T, i.e. reduction of  $B_1$ -sensitivity, is necessary to match the performance of FAIR.

## ACKNOWLEDGEMENTS

This work is part of the research program Drag and Drop ASL with project number 14951, which is (partly) financed by the Netherlands Organization for Scientific Research (NWO). We thank MeVis Medical Solutions AG (Bremen, Germany) for providing MeVisLab medical image processing and visualization environment, which was used for image analysis.

## SUPPORTING INFORMATION

In a subset of the subjects severe ASL subtraction artefacts were observed in the VSI-ASL kidney images, mainly at the top of the kidneys. Additional scans were performed to investigate the origin of this artefact, which indicated that VSI-ASL, in its current form, is affected by severe  $B_1$ -sensitivity. Supporting Information Figure 1 shows example images of a subject with severely affected VSI-ASL images and a subject with minimally affected VSI-ASL images. Spatial overlap was seen for locations affected by the negative signal and locations of reduced  $B_1$ . In addition, a scan without BGS was performed in the same subject showing that no negative signal was present. However, the VSI-ASL signal remained spatially inhomogeneous over the cortical region, see Figure 7a.

Previous research has described the dependency of  $B_1$  inhomogeneity with body geometry[60], [120]; larger body size with lower fat fraction is associated with a more severe  $B_1$ -inhomogeneity. This is also what we observed in this study; the VSI-images which were most affected by the inverted signal artefact were all tall lean subjects.

The spatial inhomogeneity of the VSI-ASL signal without background suppression suggests that the VSI-ASL implementation itself is affected. The current implementation of VSI-ASL is already more robust to  $B_0/B_1$  compared to previous versions[53], [96], [121], [122], with regard to the velocity-selective profile. However, the inversion degree of the VSI-ASL pulse train is still sensitive to  $B_1$ , due to the use of hard pulses with low flip angles, applied at the beginning of each velocity-encoding step (Figure 1)[123], [124]. An interesting new work demonstrated better performance with VSI-ASL after optimizing the sequence for myocardial perfusion imaging[125]. A similar approach would also be interesting for renal, or other, applications.

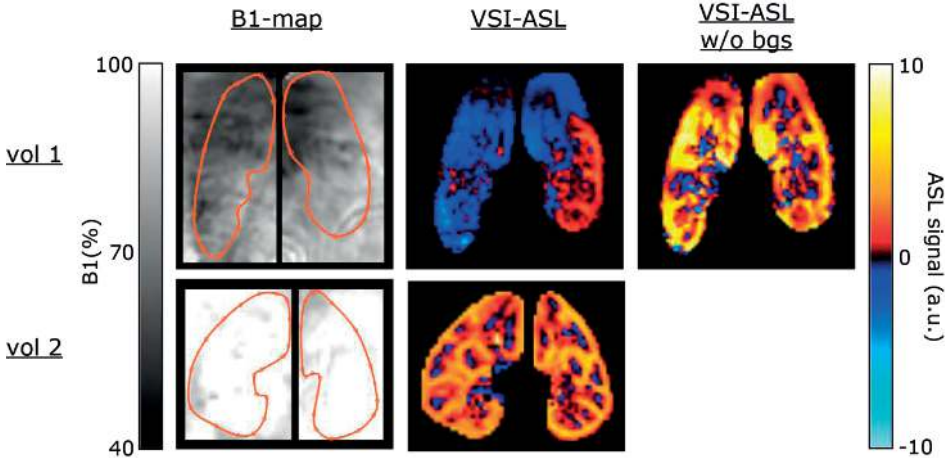
However, results indicate that the observed artefacts are not only a result of  $B_1$ -sensitivity of the VSI-labeling module, but also of the BGS-pulses. BGS is an essential element in renal perfusion ASL [36], [117], [126], but the combination of suboptimal inversion of the static tissue by VSI-ASL and suboptimal inversion of the BGS-pulses due to  $B_1$ -sensitivity could cause the tissue signal to be negative.

To further understand this, a simulation was performed for the whole VSI-sequence using the timings described in the paper for kidney and the  $T_1$  (1650ms) and  $T_2$  (150ms) values of arterial blood. The simulation was performed for a  $B_1$ - and  $B_0$ -range appropriate for the kidneys, as measured in this study and supported by previous studies[127], [128]. See figure below for the subtracted ASL-signal. Please keep in mind that the signal between ‘VSI with 3 BGS-pulses’ and ‘VSI with 2 BGS-pulses’/‘VSI without BGS’ is expected to be inverted, due to the use of

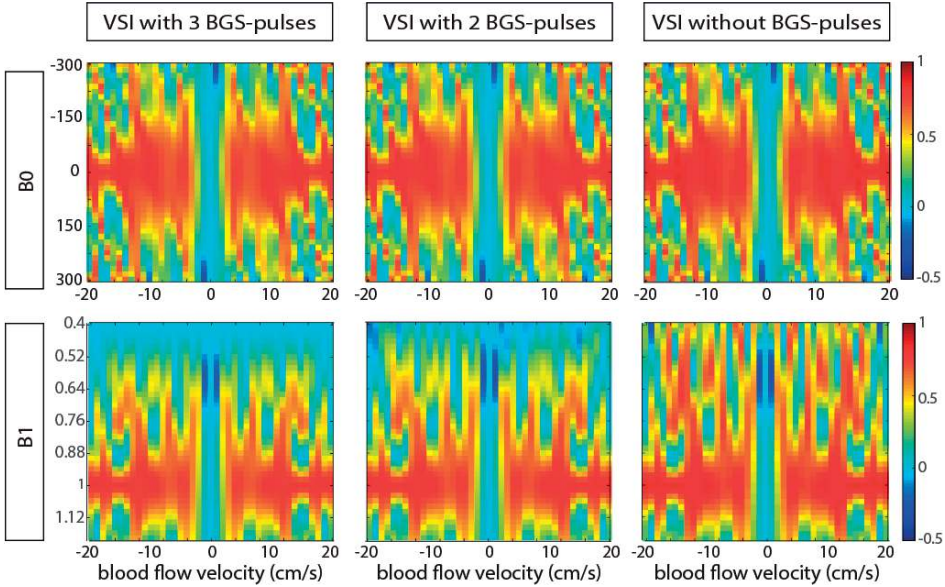
an uneven number of BGS-pulses, but the 'VSI with 2 BGS-pulses'/'VSI without BGS'-signal has been inverted to aid comparison. When looking at a  $B_1$ -values lower than 0.5 in the case of 'VSI with 3 BGS-pulses' the flowing spins have an inverted signal compared to the spins that have experienced a perfect  $B_1$ -field of 1.0. The same holds, but to a lesser degree, for 'VSI with 2 BGS-pulses'. In the case of 'VSI without BGS' this effect is not there. Furthermore the simulation shows that for non-perfect  $B_0$  or  $B_1$  variations in ASL-signal occur over velocity which may lead to variations in the ASL-signal.

The combination of imperfect inversion of the static tissue by the VSI-module in combination with imperfect inversion of the BGS-pulses could have caused the inverted ASL-signal present at the tip of the kidney found in several volunteers. This does not mean that the sequence should be run without BGS, but it does indicate that the BGS-pulses in its current shape and strength are not adequate for this application in the body.

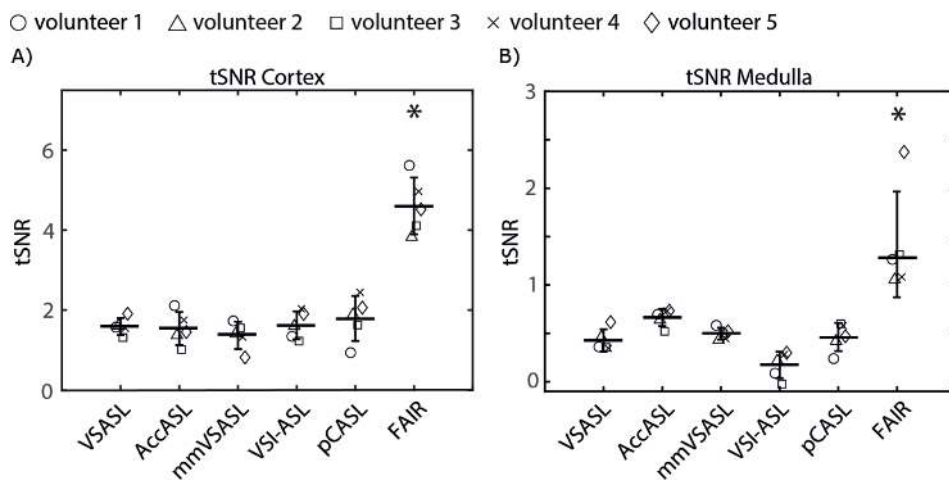
# Supporting Information Figures



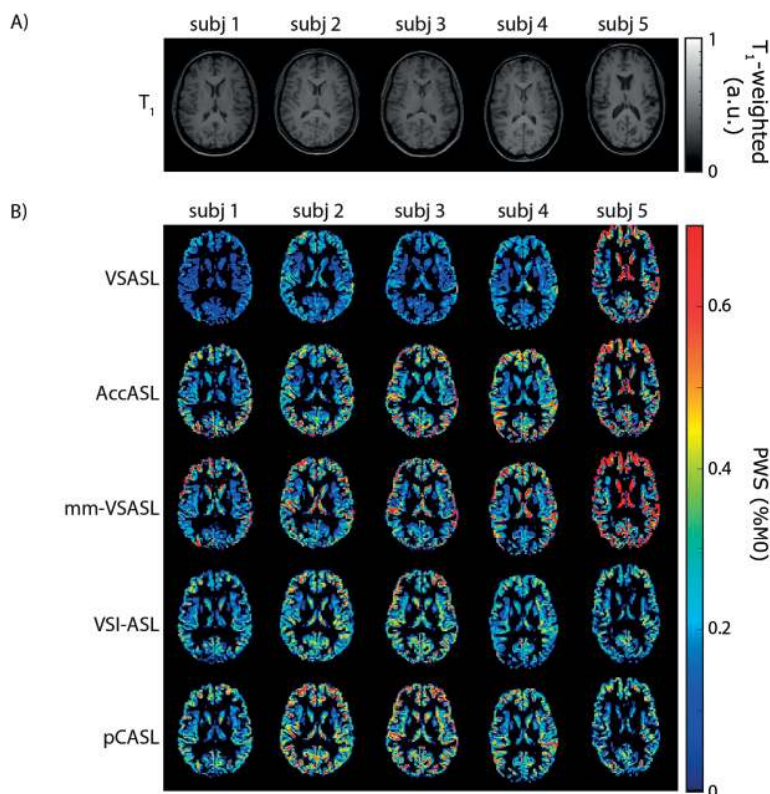
Supporting Information Figure S1. Data from a subject with severely affected VSI-ASL images (vol 1) and a subject with minimally affected VSI-ASL images (vol 2). A B1-map, including an overlay of the kidney contours, a VSI-ASL image with background suppression (BGS) and a VSI-ASL image without BGS are shown. Vol 1 shows clear negative signal in the VSI-ASL image. This artefact co-localizes with areas with reduced B1-power in the B1-map. Performing VSI-ASL without BGS showed less artefacts, although in that image there is still spatial variation of the VSI-ASL image. This indicates that the VSI-ASL artefacts are related to the B1-sensitivity of the BGS-pulses as well as the pulses in the VSI-ASL modules. These VSI-ASL images were acquired with 10 repetitions.



Supporting Information Figure S2. Simulation of the resulting ASL-signal for the whole VSI-sequence using three different background suppression (BGS) settings; with 3 BGS-pulses, with 2 BGS-pulses and without any BGS-pulses. Data was simulated using the settings for kidney, as described in the main paper. Simulation was done for a range of B0-values (top row) and a range of B1-values (bottom row). Results indicate that for VSI with 3 BGS-pulses and to a lesser degree VSI with 2 BGS-pulses negative signal can be expected for low B1-values (<0.5)

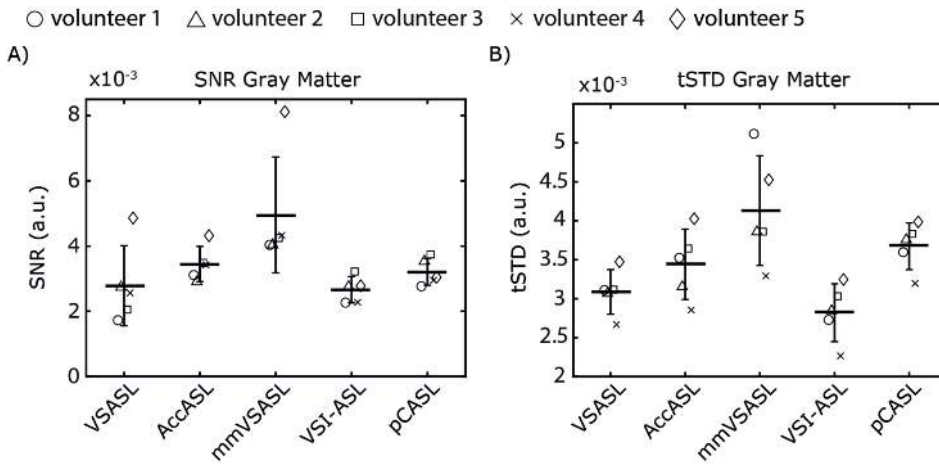


Supporting Information Figure S3. For all ASL-techniques the temporal signal-to-noise ratio (tSNR) in A) kidney cortex and B) kidney medulla using all voxels inside the mask, i.e. without excluding the artifact observed in VSI-ASL.



Supporting Information Figure S4. a)  $T_1$ -weighted scan for all five subjects. Subject 5 appears to have a deviating CSF-system with larger ventricles than the other subjects. b) perfusion-weighted signal (PWS) in the gray matter mask. Columns represent the five subjects, and rows the five ASL-techniques. One slice in the middle of the brain is shown.





Supporting Information Figure S5. For all ASL-techniques the A) ASL-signal of gray matter, treated as direct indicator of spatial signal-to-noise ratio (SNR) and B) temporal standard deviation (tSTD) in the gray matter in brain.





# Chapter 4

---

## **Feasibility of velocity-selective arterial spin labeling in breast cancer patients for non-contrast enhanced perfusion imaging**

---

Suzanne L. Franklin<sup>1,2,3</sup> MSc, Nora Voormolen<sup>4</sup> MD, Isabell K. Bones<sup>2</sup> MSc, Tijmen Korteweg<sup>4</sup> MD, PhD, Martin N.J.M. Wasser<sup>4</sup> MD, Henrike G. Dankers<sup>4</sup> BSc, Daniele Cohen<sup>5</sup> MD, PhD, Marijn van Stralen<sup>2</sup> PhD, Clemens Bos<sup>2</sup> PhD, Matthias J. P. van Osch<sup>1,3</sup> PhD.

<sup>1</sup>C.J. Gorter Center for High Field MRI, Department of Radiology, Leiden University Medical Center, Leiden, The Netherlands

<sup>2</sup>Center for Image Sciences, University Medical Centre Utrecht, Utrecht, The Netherlands

<sup>3</sup>Leiden Institute for Brain and Cognition, Leiden University, Leiden, The Netherlands

<sup>4</sup>Department of Radiology, Leiden University Medical Center, Leiden, The Netherlands

<sup>5</sup>Department of Pathology, Leiden University Medical Center, Leiden, The Netherlands

## ABSTRACT

**Background:** Dynamic contrast enhanced (DCE) MRI is the most sensitive method for detection of breast cancer. However, due to high costs and retention of intravenously injected gadolinium-based contrast agent, screening with DCE-MRI is only recommended for patients who are at high risk for developing breast cancer. Thus, a non-contrast enhanced alternative to DCE is desirable.

**Purpose:** To investigate whether velocity selective arterial spin labeling (VS-ASL) can be used to identify increased perfusion and vascularity within breast lesions compared to surrounding tissue.

**Study type:** Prospective.

**Population:** 8 breast cancer patients

**Field strength/sequence:** 3 T; VS-ASL with multi-slice single-shot GE-EPI readout.

**Assessment:** VS-ASL scans were independently assessed by three radiologists, with 3-25 years of experience in breast radiology. Scans were scored on lesion visibility and artifacts, based on a 3-point Likert scale. A score of 1 corresponded to 'lesions being distinguishable from background' (lesion visibility), and 'no or few artifacts visible, artifacts can be distinguished from blood signal' (artifact score). A distinction was made between mass and non-mass lesions (based on BI-RADS lexicon), as assessed in the standard clinical exam.

**Statistical tests:** Intra-class correlation coefficient (ICC) for inter-observer agreement.

**Results:** The ICC was 0.77 for lesion visibility and 0.84 for the artifact score. Overall, mass lesions had a mean score of 1.27 on lesion visibility, and 1.53 on the artifact score. Non-mass lesions had a mean score of 2.11 on lesion visibility, and 2.11 on the artifact score.

**Data conclusion:** We have demonstrated the technical feasibility of bilateral whole-breast perfusion imaging using VS-ASL in breast cancer patients.

## INTRODUCTION

Breast MRI is the most sensitive tool for detection of breast cancer [66] with a sensitivity at least twice as high as mammography [66]. The specificity of breast MRI is increased by use of multi-parametric (mpMRI) protocols [129], which combine information from different MR techniques [129]. It is recommended as an annual screening tool for women with an increased risk of breast cancer [130]. The backbone of breast MRI is dynamic contrast enhanced (DCE) MRI, which relies on intravenous injection of a gadolinium-based contrast agent (GBCA) and enables assessment of lesion morphology as well as tracer kinetics, both important features for lesion characterization [131]. However, an alternative technique that does not require GBCA injection is desirable because of growing concern related to use of GBCAs [29], the additional staff costs because of the time required for intravenous injection [71], costs of the contrast agent itself [71], and patient discomfort.

In conventional DCE-MR, both the wash-in and wash-out phase, minutes after contrast administration, are assessed. Studies on ultrafast DCE, with a temporal resolution of seconds in the intravenous contrast wash-in phase, showed similar results in less time [132], [133]. The early wash-in phase is mainly determined by perfusion. Later on image contrast is dominated by leakage of the contrast agent into the extravascular space, due to increased vessel wall permeability in tumors [26].

Arterial Spin Labeling (ASL) might be a promising non-contrast enhanced alternative for DCE-MRI. Similar as ultrafast DCE-MRI, ASL provides information on perfusion and vascularity, without being sensitive to vessel wall permeability. However, ASL does not require administration of contrast agent. ASL achieves perfusion contrast by labeling blood magnetically [32]. In ASL, two images are acquired alternately; a label image, where blood is labeled magnetically, and a control image. The label and control images are subtracted to obtain an ASL image, where the static tissue signals cancel out and only labeled blood signal is left. Most common ASL techniques in brain and body, such as pseudo continuous ASL (pCASL) [13], [38], and flow-sensitive alternating inversion recovery (FAIR) [62], [134], are spatially-selective. In spatially-selective techniques, labeling of blood takes place in the feeding arteries of the tissue of interest [32], resulting in a transit delay between the labeling location and arrival of labeled blood in the tissue. During the transit delay, labeled blood will not only flow from the labeling location into the tissue, but will also decay with the  $T_1$  of blood, which is around 1.65 s at  $3T$  [13]. Thus for a delay of 1.65 s, already 65% of ASL signal is lost. This poses a significant challenge for breast ASL. Blood flow in the internal mammary artery, feeding the breast is on the order of 19 cm/s [44], which is lower than the blood flow in the carotid arteries feeding the brain, i.e. 39 cm/s [78]. This complicates the use of spatially-selective ASL techniques in breast.

Velocity-selective ASL is an ASL-technique that labels blood based on flow velocity instead of spatial location [49]. All blood above a certain cutoff velocity gets labeled, so if the cutoff velocity is chosen low enough the transit delay is essentially eliminated. Hence, we hypothesized that VS-ASL can be used in breast and has the potential to serve as a non-contrast enhanced perfusion method in breast cancer patients.

In this study, the technical feasibility of VS-ASL in breast was investigated. Thus the aim of this study was to investigate whether VS-ASL generated enough contrast at a lesion location to identify increased perfusion and vascularity within breast lesions compared to surrounding tissue.

## MATERIALS AND METHODS

### Subjects

This study was approved by the local ethics committee (METC Leiden Den Haag Delft NL70510.058.19) and informed consent was obtained from all participants. Patients were recruited via the outpatient clinic for breast cancer. Inclusion criteria were: scheduled for an MRI breast exam (either for screening or staging purposes), aged 18 years or over, and mentally competent. Exclusion criteria were: unable or unwilling to comply with breathing instructions, contra-indications for gadolinium-based contrast agents, and having previously undergone breast reduction treatment.

### Image acquisition

All subjects were scanned in prone position on a 3 T Philips Ingenia Elition scanner (Philips, Best, The Netherlands), using a dedicated 16-channel bilateral breast coil. For all scans, image-based shimming (SmartBreast, Philips, Best, The Netherlands) was used to reduce  $B_0$ -related artifacts. A VS-ASL and  $M_0$  scan were acquired prior to the standard clinical protocol. To reduce motion artifacts, the VS-ASL and  $M_0$  scans were acquired with paced breathing; patients were asked to synchronize their breathing with image acquisition such that they held their breath (on exhalation) during the acquisition and then took shallow breaths in and out between acquisitions. Coaching was provided via the intercom, and patient cooperation was monitored using VitalEye (Philips, Best, The Netherlands).

The VS-ASL scan was acquired with a single-shot GE-EPI readout.

Twenty transverse slices with 5 mm thickness, a 1 mm slice gap, an acquisition resolution of  $2.75 \times 2.75 \text{ mm}^2$ . The field-of-view was bilateral and was set to  $200 \times 119 \times 196 \text{ mm}^3$ . The scan had a TE of 15 ms, and the TR was set to 6500 ms to produce a close-to-natural breathing

rhythm. The fold-over direction was right-left, to prevent fold-in signal of the heart. VS-ASL labeling was performed using a pair of hyperbolic secant pulses and bipolar gradients, as described by Wong [32], using only a single VS-ASL labeling module (i.e. excluding the second VS-ASL labeling module). The VS-ASL scans were acquired with a cutoff velocity of 2 cm/s, velocity-encoding direction feet-head, VS-ASL module duration of 50 ms, and hyperbolic secant pulses with a maximum  $B_1$  of 13.5  $\mu$ T and a duration of 20 ms. The post-label delay (PLD) was set to 1000 ms. Spectral presaturation with inversion recovery (SPIR) [135] fat suppression was used, and background suppression pulses [13] (hyperbolic secant), aimed to null fat signal, were applied 366 ms and 820 ms after labeling. Twenty-one pairs of control and labeled images were acquired, resulting in a scan duration of 4 min 46 s.

An  $M_0$  scan was acquired for calibration of the ASL signal. The  $M_0$  scan was acquired using the same readout as the VS-ASL scan but with ASL labeling turned off. Four repetitions of the  $M_0$  image were acquired, resulting in a total scan time of 40 s.

The clinical protocol included  $T_2$ -weighted turbo spin echo (TSE) Dixon, diffusion-weighted imaging (DWI), DCE, and ultrafast DCE scans. The  $T_2$ -weighted Dixon was acquired with 83 slices, an acquisition resolution of  $1.2 \times 1.2 \times 2.4 \text{ mm}^3$ , TE/TR of 140 ms/5856 ms, and a TSE-factor of 24. DWI was acquired with b-values of 500  $\text{s/mm}^2$ , 1000  $\text{s/mm}^2$ , and 1500  $\text{s/mm}^2$ , 42 slices, an acquisition resolution of  $2 \times 2 \times 4 \text{ mm}^3$ , and a 2D SE-EPI readout. Lastly, DCE and ultrafast DCE images were acquired with Dotarem (0.5 mmol/mL) as GBCA, using a dosage of 0.2 cc/kg. Ultrafast DCE was acquired with a 3D gradient-echo  $T_1$ -weighted readout without fat suppression, using 136 slices and a spatial resolution of  $1.3 \times 1.3 \times 1.3 \text{ mm}^3$ . DCE-MRI was acquired using a 3D multi-shot turbo-field echo (TFE) readout, using a TFE factor of 30, spectral attenuated inversion recovery (SPAIR) [136] fat suppression, 140 slices, and a spatial resolution of  $1.0 \times 1.0 \times 1.5 \text{ mm}^3$ . Before contrast injection, baseline DCE and ultrafast DCE-images were acquired. Directly after contrast injection, the ultrafast DCE series of 14 time points with a temporal resolution of 3.9 s was started, and subsequently the regular DCE-series of 5 time points with a temporal resolution of 1 min 12 s.

## Image analysis

Image analysis was performed using MeVisLab (MeVis Medical Solutions AG, Fraunhofer MEVIS, Bremen, Germany). The breast VS-ASL and  $M_0$  images were co-registered to each other using a group-wise image registration method [114]. For each voxel  $i$ , the ASL subtraction signal  $\Delta S_i$  was obtained by subtracting control ( $C_{r,i}$ ) and label ( $L_{r,i}$ ) images, and averaged over the total number of repetitions  $R$  (equation 1). An  $M_0$ -value was obtained by averaging over all  $N$  voxels within a manually drawn  $\text{ROI}_{\text{heart}}$  (researcher \*\* in consensus with radiologist \*\*) in the left ventricle of the heart (equation 2). The resulting perfusion-weighted signal (PWS) value for each voxel  $i$  was obtained by dividing the ASL images with the  $M_0$ -value.



$$\Delta S_i = \frac{1}{R} \sum_{r=1}^R (C_{r,i} - L_{r,i}) \quad (1)$$

$$M_0 = \frac{1}{N} \sum_{i_{ROI-heart}=1}^N M_{0,i_{ROI-heart}} \quad (2)$$

$$PWS_i = \frac{\Delta S_i}{M_0} \quad (3)$$

Scans from the standard clinical protocol were assessed as part of the standard clinical protocol. In case a lesion was present, information regarding location, size, apparent diffusion coefficient (ADC) map reduction, and whether the lesion presents itself as mass (space-occupying) or non-mass (areas of enhancement without clear space-occupancy) according to the BI-RADS lexicon [137] was extracted from the clinical report. In addition, images from the clinical DCE, ultrafast DCE scans and the ADC maps calculated from the clinical DWI-scans were obtained from the clinical patient database. Ultrafast DCE images at 10 s after enhancement of internal thoracic artery, reflecting mainly perfusion, were obtained to compare to the VS-ASL images. All patients included for staging purposes received a biopsy prior to MRI, while all patients included for screening purposes only received a biopsy post-MRI in case there was an indication based on the MRI results. When available, lesion characterization from biopsy was obtained from the clinical reports.

Three radiologists (\*\*/\*\*/\*\*) with 3-25 years of experience in breast radiology scored the PWS-maps of the VS-ASL scans on lesion visibility and artifacts, based on a 3-point Likert scale. For lesion visibility, a score of 1 was defined as: “signal at the location of the lesion can be distinguished from surrounding tissue”, 2: “suspicion that signal at the location of the lesion is deviant from surrounding tissue”, 3: “signal at the location of the lesion cannot be distinguished from surrounding tissue”. For the artifact score, a score of 1 was defined as: “no or few artifacts are visible, artifacts can be distinguished from blood signal”, 2: “artifacts are visible, most can be distinguished from blood signal”, and 3: “artifacts have similar intensity as blood signal, and obscure assessment of the image”.

In addition, ROIs were drawn at the location of the lesion (in all slices occupied by the lesion) by a researcher (\*\*) in consensus with a radiologist (\*\*). The PWS values of all  $J$  voxels in the ROI were averaged, to obtain a measure for signal enhancement of the lesion ( $PWS_{lesion}$ ) on the VS-ASL PWS images (see equation 4).

$$PWS_{lesion} = \frac{1}{J} \sum_{i_{ROI-lesion}=1}^J PWS_{i_{ROI-lesion}} \quad (4)$$

## Histopathology

Microscopic evaluation of the tissue was performed for two patients (patient 2 and patient 7). One of the two patients underwent preventive bilateral breast ablation, and the other patient underwent lumpectomy. Thin section histopathology slices were analyzed to evaluate vascularity around the lesions, to be able to check for a biological basis of the VS-ASL signal observed in these two patients.

## Statistical analysis

The Intra-class Correlation Coefficient (ICC) was calculated to assess inter-observer agreement, using SPSS Statistics (IBM Corp, Armonk, NY, USA), using a significance level of 0.05. An ICC of  $>0.74$  was considered excellent, 0.6-0.74 good, 0.4-0.59 fair, and  $< 0.4$  poor.

## RESULTS

Preliminary data comparing VS-ASL with a SE-EPI and GE-EPI readout, and comparing multi-slice VS-ASL with FAIR, a spatially-selective technique, acquired with a single as well as a multi-slice readout is presented in Figure 1, 2 and 3 in the Supplementary Material. Based on the standard clinical protocol, seven out of ten patients had a lesion on DCE-MRI, of which one patient had bilateral lesions (Table 1). Four lesions were classified as invasive carcinoma, three as DCIS and one as a benign blunt duct adenosis. In one patient (Patient 3), the lesion was not visible on DCE-MRI, since it was a small focus of DCIS grade 1, which was likely completely removed by biopsy prior to the MRI. Of these eight lesions visible on DCE-MRI, five presented as mass, with sizes ranging between 23-32 mm, and three as non-mass, with sizes ranging between 10-12 mm.

There was an excellent inter-observer agreement between the three readers for lesion visibility (ICC = 0.77, 95% confidence interval (CI) = 0.18-0.95) and artifact scoring (ICC = 0.84, IC = 0.55-0.95). Table 1 shows for all patients: the outcomes of the clinical MR exam, biopsy results, mean PWS of the lesion, and the lesion visibility and artifact scores averaged over the three observers. The mean lesion visibility score was 1.58. Mass lesions had a mean score of 1.27, and non-mass lesions 2.11.

Overall, VS-ASL showed a comparable morphology to the early time point of ultrafast DCE. Larger arteries and veins were also clearly visualized. A representative patient with bilateral mass lesions is shown in Figure 1, and a representative patient with non-mass lesions in Figure 2.

The mean artifact score was 1.9. Mass lesions had a mean artifact score of 1.53, and non-mass lesions 2.11. A representative patient with a high artifact score is shown in Figure 3.

Patient	Left/ Right breast	Indication	Clinical MR exam			Hormone receptors	Biopsy	VS-ASL	
			Size (mm)	DCE- enhancement	ADC reduction			PWS at lesion (%M0)	VS-ASL: Mean scores observers
							Lesion	Artifact	
							visibility	visibility	
1	-	Screening	-	-	-	-	-	2	
2	Left	Screening	11	Non-mass	Yes	-	DCIS 2	0.50	2
3	Left	Staging	6	Not visible*	No	-	DCIS 1	-	2.6
4	-	Screening	-	-	-	-	-	-	2.3
5	Left	Staging	27	Mass	Yes	ER+, PR-, HER2- (right)	DCIS 1 + adenosis	0.70	1.3
	Right		32	Mass	Yes	-	Invasive lobular carcinoma 2	0.32	1
6	Right	Staging	30	Mass	Yes	ER+, PR-, HER2-	Invasive carcinoma NST 2	0.76	1
7	Left	Staging	23	Mass	Yes	ER+, PR+, HER2+	Invasive carcinoma NST 2	0.78	1
8	Right	Staging	12	Non-mass	No	ER-, PR-, HER2-	Invasive carcinoma NST 3	0.17	2.3
9	Right	Staging	10	Non-mass	Yes	-	Blunt duct adenosis	0.4	2
10	Left	Staging	33	Mass	Yes	ER+, PR-, HER2-	Pleomorphic lobular carcinoma	3.34	2
									2.3

Table 1. Patient characteristics and results of clinical MR exam, biopsy, and the velocity-selective arterial spin labeling (VS-ASL) scan. The results presented for the clinical MR exam and biopsy were taken from the clinical report. Abbreviations: DCE = dynamic contrast enhanced, ADC = apparent diffusion coefficient, ER+/- = estrogen receptor positive/negative, PR+/- = progesterone receptor positive/negative, HER2+/- = human epidermal growth factor receptor-2 positive/negative, DCIS = ductal carcinoma in-situ, PWS = perfusion-weighted signal, Lesion visibility: 1 = "signal at the location of the lesion can be distinguished from surrounding tissue", 2 = "suspicion that signal at the location of the lesion is deviant from surrounding tissue", 3 = "signal at the location of the lesion cannot be distinguished from surrounding tissue". Artifact score: 1 = "no or few artifacts are visible, artifacts can be distinguished from blood signal", 2 = "artifacts are visible, most can be distinguished from blood signal", 3 = "artifacts have similar intensity as blood signal, and obscure assessment of the image". \* DCIS grade 1 was found in a stereotactic biopsy specimen of 4 mm suspicious calcifications, in which probably the whole lesion was removed.

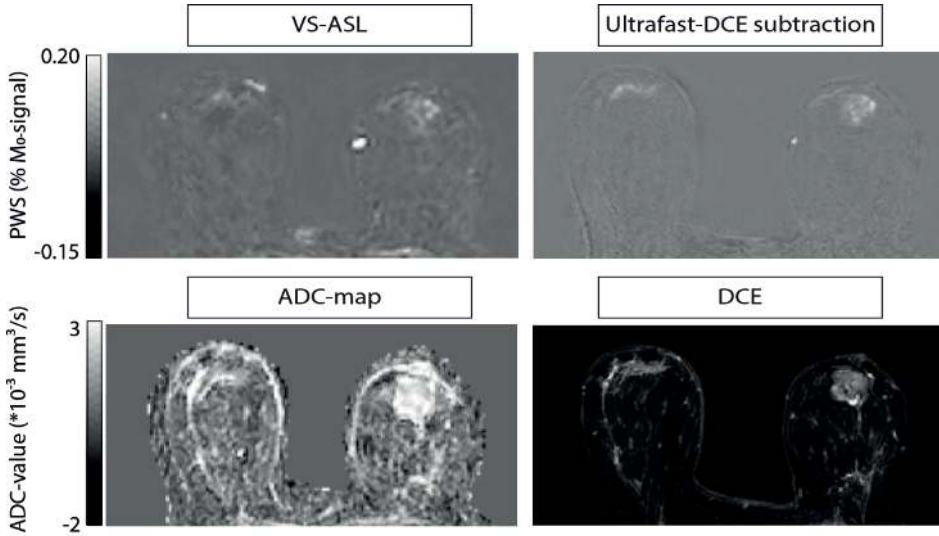


Figure 1. Representative patient with mass lesions; Patient 5 with invasive lobular carcinoma grade 2 in right breast, and ductal carcinoma in situ grade 1 with adenosis in left breast. Signal in the VS-ASL image corresponds with perfusion signal in early-phase ultrafast DCE. Top row, from left to right: VS-ASL, and the subtraction image of ultrafast DCE at a time point of 10 s after contrast agent arrival in the internal thoracic artery. Bottom row, from left to right: ADC map calculated from  $b=500-1000$  s/mm<sup>2</sup> and the first time point after contrast injection of the standard DCE scan, reflecting both perfusion and vessel wall permeability.

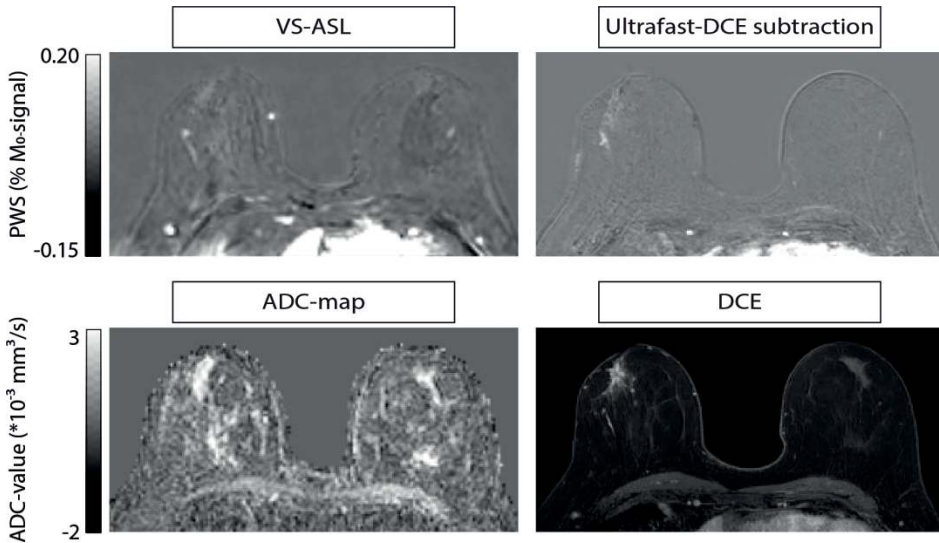


Figure 2. Representative patient with a non-mass lesion; Patient 9 with adenosis in the right breast. Signal in the VS-ASL images corresponds with perfusion signal in the early phase ultrafast DCE. Top row, from left to right: VS-ASL, and the subtraction image of ultrafast DCE at a time point of 10s after contrast agent arrival in the internal thoracic artery. Bottom row, from left to right: ADC map calculated from  $b$  500-1000 s/mm<sup>2</sup>, and the first time point approximately one minute after contrast injection of the standard DCE scan, reflecting both perfusion and vessel wall permeability.

While scoring the data, an observation was made (N.V.) concerning increased VS-ASL signal adjacent to the lesion, which was consistent with a segmental pattern. This segmental pattern of increased VS-ASL signal was observed in three patients, see Figure 4 for a representative case. No correlate was found on the ultrafast DCE images for these findings. However, on the DCE images, all three patients have notable vessels in these areas, see Figure 4(C).

Histopathological analyses were performed for two patients: one diagnosed with a DCIS lesion (patient 2) and one with an invasive carcinoma (patient 7), see Table 1. In both patients, a clear difference in the size and hypertrophy of the small vessels surrounding the lesion, compared to the healthy breast tissue in the same patient was observed, see Figure 4 in the Supplementary Material.

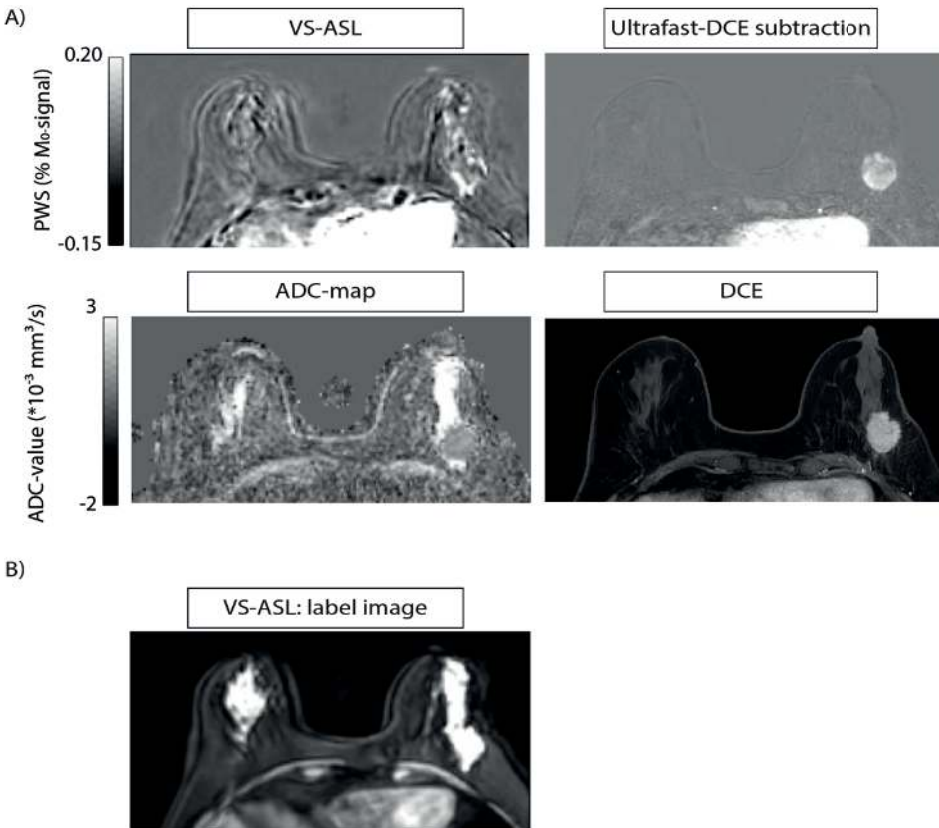


Figure 3. Representative patient with dense breast; A) patient 10 with a pleiomorphic lobular carcinoma in the left breast, and dense breast. B) The dense glandular tissue gives a relatively high signal contrast on the label-images. Thus, motion can consequently easily lead to subtraction errors in the VS-ASL image.

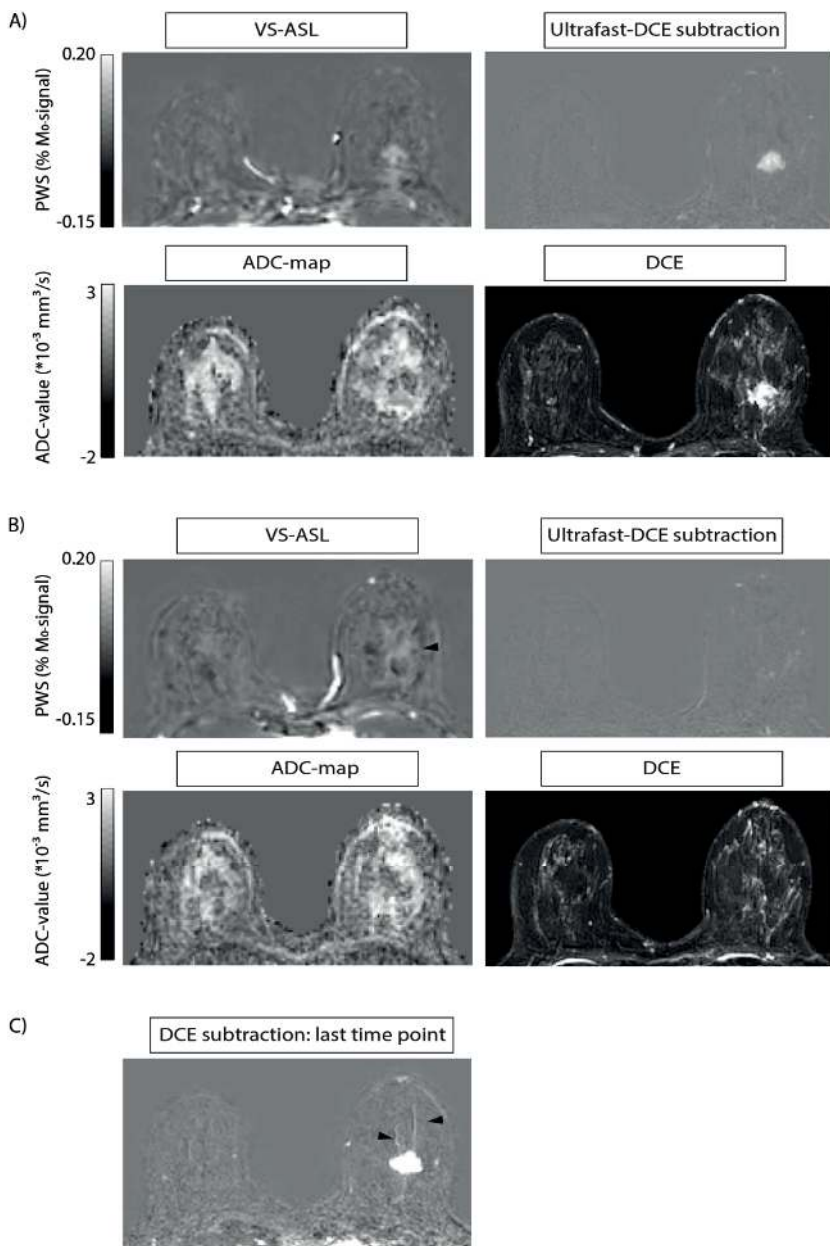


Figure 4. Representative patient with a segmental pattern of increased VS-ASL signal; patient 7 with an invasive carcinoma grade 2 in the right breast. A) slice containing the lesion, signal in the VS-ASL image corresponds with perfusion signal in the early-phase ultrafast DCE. B) Segmental pattern of increased perfusion (indicated by black arrow) on the VS-ASL images, in an adjacent slice to the tumor. There is no correlate of this pattern on the DCE, ultrafast DCE or the ADC map. However, in C) notable vessels (indicated by black arrows) in the same area can be seen on the last time point of the DCE subtraction, likely showing a biological basis for the perfusion pattern seen in B. Histopathological data of this patient is shown in Supporting Information Figure 4. Within sections A and B: Top row, from left to right: VS-ASL, and the subtraction image of ultrafast DCE at a time point of 10 s after contrast agent arrival in the internal thoracic artery. Bottom row, from left to right: ADC map calculated from  $b=500\text{-}1000 \text{ s/mm}^2$ , and the first time point after contrast injection of the standard DCE scan, reflecting both perfusion and vessel wall permeability.

# DISCUSSION

Our results demonstrated the feasibility of bilateral whole-breast perfusion imaging using VS-ASL in breast cancer patients. Moreover, a correspondence was observed in morphology of the patterns seen in VS-ASL and early-phase ultrafast DCE images.

Finding a non-contrast imaging technique to investigate tumor perfusion and vascularity is essential, as angiogenesis is one of the first signs of tumor growth and is critical for identifying breast cancers with a higher potential for invasion and metastasis [4], [138]. Compared to traditional ASL methods, VS-ASL addresses the challenging perfusion characteristics of the breast, and enables bilateral whole-breast perfusion imaging.

Previous studies investigating the feasibility of ASL in breast cancer employed spatially-selective ASL techniques with a single slice planned on the tumor, using coronal slices to label the chest wall including the heart [75]–[77], [139]. However, spatially-selective ASL can lead to low SNR in case of multi-slice scanning in breast, due to slow flow. When using a multi-slice read-out, the label is created further away from the breast tissue and the resulting prolonged transit delays, due to slow flow, will result in little label having reached the relevant slices at the time of acquisition. If the PLD is adjusted to for the prolonged transit delays, more SNR would be lost to  $T_1$ -decay of label, leading to poor image quality. Moreover, single-slice FAIR would have, in addition to arterial signal, a contribution from venous signal flowing in posterior direction. Because whole-breast coverage is a necessity for screening purposes, spatially-selective ASL is unsuitable as a non-contrast screening method.

Overall, inter-observer agreement of VS-ASL was excellent for lesion visibility, and the artifact score. The mean lesion visibility was good, indicating that signal at the lesion could either be clearly distinguished from surrounding tissue or that there was a suspicion that the signal was deviant at the location of the lesion. The results suggest that in this limited sample size, non-mass lesions were less visible. However, the non-mass lesions included in this study also had a smaller size. Visibility of the lesions on VS-ASL corresponded well with visibility on the early-phase ultrafast DCE images, confirming that VS-ASL is a measure of perfusion and vascularity, similar to early-phase ultrafast DCE [26]. Parameters derived from ultrafast DCE-MRI have been shown to be able to discriminate between benign and malignant lesions [140] and have a strong relationship with tumor subtype [141]. Thus, it would be interesting to investigate whether VS-ASL could also provide sufficient information to discriminate between benign and malignant lesions.

While scoring the data, there was an unexpected finding by one of the observers: segmental patterns of increased perfusion were observed on the VS-ASL PWS images adjacent to the

lesion for three patients. In all cases, the pattern followed prominent vessels which were visible on DCE-MR, suggesting a biological basis for the segmental perfusion patterns. The segmental perfusion patterns could indicate increased flow in the drainage area of the lesion due to a pathological vascular bed. Because vascularization has shown to be valuable in tumor diagnosis [142], [143], it would be interesting to investigate whether vascularization scores and observation of segmental perfusion patterns can aid detection of lesions in VS-ASL images.

Scoring of the artifacts showed that artifacts were present in the VS-ASL data, but that, overall, they could be distinguished from blood signal. In a few cases, the mean artifact score indicated that artifacts impacted proper assessment of the image. In all of these cases the patient had extremely dense breast, according to the American College of Radiology classification, except for one patient who had a blood edema next to the lesion which obscured visibility. The artifacts observed in patients with dense breast are likely a result of a high contrast between fat and glandular tissue in the raw VS-ASL images, which can easily lead to subtraction artifacts in case of small movements. Currently, two background suppression pulses were used. The short PLD of VS-ASL prevents optimal suppression of both fat and glandular tissue. Possible strategies to improve the background suppression would be to increase the PLD and optimize timings for both tissue types, or to increase the number of background suppression pulses to three, to be able to suppress tissues across a broader range of  $T_1$  values [144]. However, both strategies would come at the cost of SNR, by increased  $T_1$ -decay or by increased signal loss due to imperfect inversion pulses, respectively. Future studies are necessary to find out whether these proposed strategies result in a reduction of subtraction artifacts in patients with dense breast, at an acceptable SNR penalty.

Note that the VS-ASL signal we measured is a combination of arterial and venous signal. Single VS-ASL was used: meaning that only one VS-ASL module was applied, instead of two as is commonly done in VS-ASL [49]. This second labeling module acts as a vascular crusher with a matched cutoff velocity, in both label and control condition. It has the effect of removing the venous and vascular contributions to the signal, and defines the bolus duration, such that quantification of perfusion becomes possible. However, it comes at the expense of a reduction in SNR [51]. This module was not applied by us, because being able to visualize venous and vascular signal could be clinically relevant in breast cancer patients, and, because we opted for maximum SNR for these first applications of VS-ASL in breast, in view of the anticipated low ASL signal.

The single VS-ASL sequence was played out with a cutoff velocity of 2 cm/s, as has previously been done [49], while using a relatively short PLD. The choice of cutoff velocity is a trade-off between labeling as close as possible to target tissue while preventing imaging artifacts caused by the increased gradient area. The motivation for using a short PLD was twofold. First, the



low cutoff velocity provides label already within the target region. Secondly, single VS-ASL was used, i.e. there is no second VS-ASL labeling module. Conventionally in VS-ASL, a longer PLD is required to ensure deceleration of the labeled blood before the second VS-ASL module is applied. In our implementation, this was not the case, so a shorter PLD was used to prevent unnecessary loss of ASL-signal due to  $T_1$ -decay.

Histopathologic analyses confirmed more vessels as well as more hypertrophic vessels at the border of a DCIS grade 2 and an invasive carcinoma, providing a possible biological basis for the VS-ASL signal. Vascularity is an important characteristic of biologically more aggressive breast cancer subtypes[142], [143]. Sensitive to vascularization and perfusion, VS-ASL may also be sensitive to biologically aggressive breast cancer subtypes, similar as DCE-MRI[69].

## Limitations

First, as mentioned above, the background suppression should be optimized to reduce subtraction artifacts in patients with dense breast. Second, larger voxel sizes were used for VS-ASL ( $2.75 \times 2.75 \times 5 \text{ mm}^3$ ) compared to DCE-MRI ( $1 \times 1 \times 1.5 \text{ mm}^3$ ) and ultrafast DCE ( $1.3 \times 1.3 \times 3 \text{ mm}^3$ ), and since the desired detection limit of DCE-MRI is 5 mm [131], future studies are needed to determine whether that detection limit can be met by VS-ASL.

Third, in contrast to DCE-MRI, no information on kinetics and vessel wall permeability is acquired with VS-ASL. These parameters are currently used to differentiate between lesion subtypes; however, studies using ultrafast DCE-MRI have shown that similar diagnostic accuracy can be achieved by only looking at the early perfusion phase, which does not include information on vessel wall permeability[140], [141]. Future studies are necessary to investigate whether VS-ASL could provide similar information as ultrafast DCE and whether other characteristics in VS-ASL images could provide the same, or at least sufficient, discriminatory capability. Fourth, the VS-ASL technique we used may not be the optimal velocity-selective technique. For example, symmetric BIR-8 VS-ASL would be an interesting approach to limit erroneous labeling due to eddy currents and achieve higher robustness to  $B_0$  and  $B_1$  [57]. Also velocity-selective prepared inversion (VSI-) ASL, which has demonstrated similar SNR as pCASL[122], [145], would be an interesting option. An adaptation to the original VSI-ASL sequence has been published, to improve robustness for  $B_0$  and  $B_1$  [146], which could prove essential for breast applications. Finally, the aim of this study was to do a technical proof-of-concept, so a small sample group was included. Future studies should include larger patient groups to establish the sensitivity and specificity of this technique, in terms of specific populations as well as lesion size and cancer subtype.

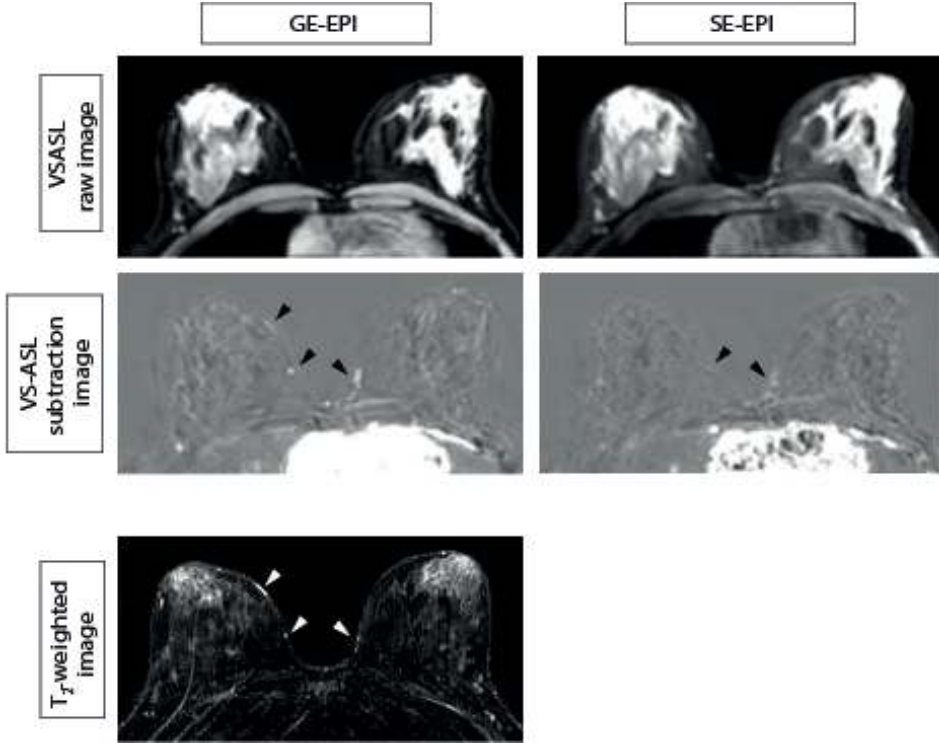
## **Conclusion**

Our results demonstrate the feasibility of VS-ASL as a non-contrast enhanced measurement of perfusion and vascularity in breast. VS-ASL is a promising technique that could add to a non-contrast mpMRI protocol for breast. A non-contrast mpMRI protocol would considerably reduce both patient discomfort and cost and could possibly be used as a pre-screening method so that only patients with suspicious findings are referred for a DCE-MRI exam.

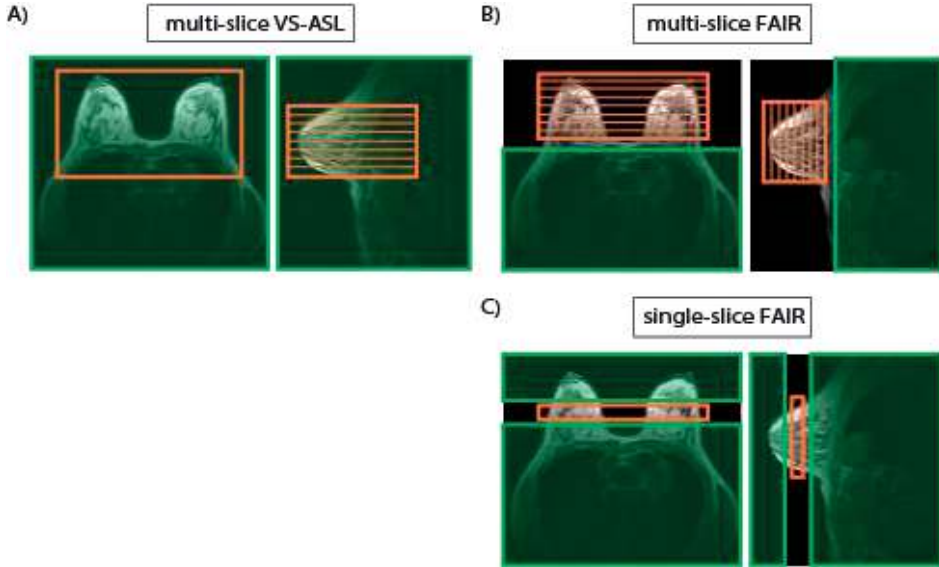
## **ACKNOWLEDGEMENTS**

The authors thank MeVis Medical Solutions AG (Bremen,Germany) for providing MeVisLab medical image processing and visualization environment, which was used for image analysis. The authors thank E. M. M. Krol-Warmerdam, J. van Leeuwen-Büttner, and G.M.C. Ranke for their valuable help in recruitments of patients. This work is part of the research program Drag and Drop ASL with project number 14951, which is (partly) financed by the Netherlands Organization for Scientific Research (NWO).

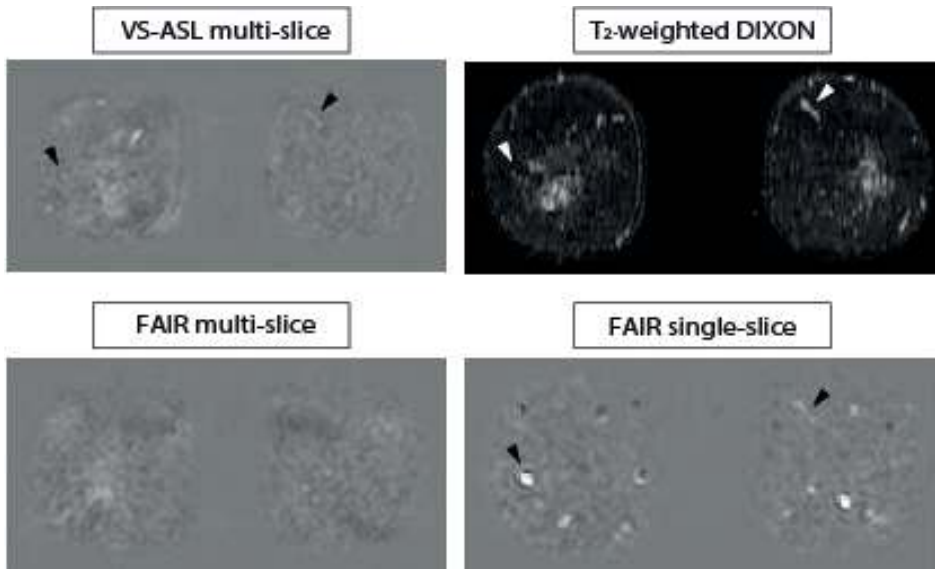
# SUPPORTING INFORMATION FIGURES



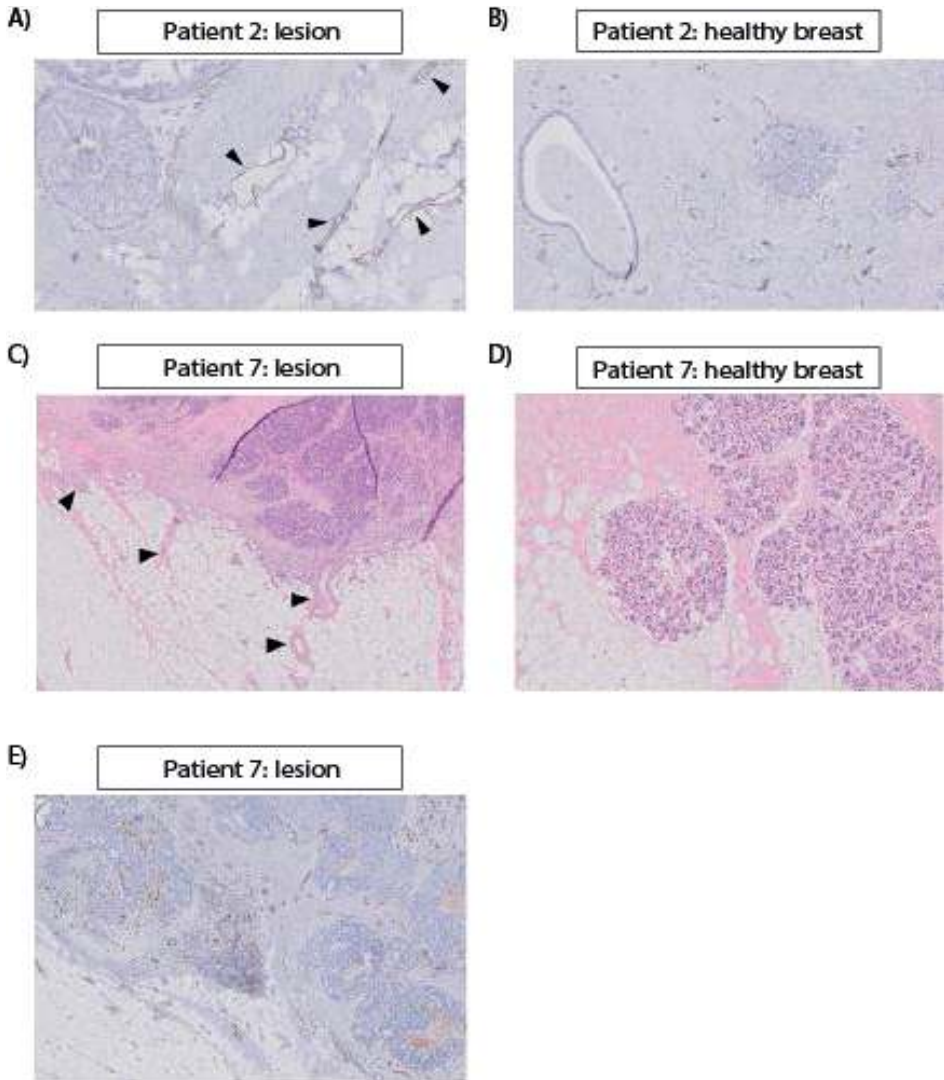
Supporting Information Figure 1. Comparison of single-shot multi-slice GE-EPI and SE-EPI readout for VS-ASL in a healthy volunteer. Top row: the VS-ASL label images, before subtraction (raw image). Second row: the VS-ASL subtraction images. Third row: the corresponding T<sub>2</sub>-weighted image. The vascular signal in VS-ASL (black arrows), which corresponds to the vascular signal in the T<sub>2</sub>-weighted image (white arrows), is more clearly visible with GE-EPI readout compared to SE-EPI readout. Therefore, a GE-EPI readout was used for patient scans. Note, that the ASL images in healthy volunteers mainly show vascular signal, because the perfusion levels of healthy tissue are too low to measure. Scan parameters for both sequences were the same as described in the main document, except that for the SE-EPI scan the TE was set to 25 ms and a half scan factor was set to 0.7.



Supporting Information Figure 2. Slice planning for A) VS-ASL, B) multi-slice FAIR and C) single-slice FAIR. The orange box represents the imaging stack, and the green box represents the area where label is created. As can be seen in A) label is created also inside the imaging region when using VS-ASL labeling, while this is not the case for FAIR. With multi-slice FAIR the labeling takes place further from the imaging region (B), leading to a reduced SNR in the resulting ASL image. In single-slice FAIR the labeling takes place close to the imaging region (C), and label is created on both sides of the imaging slice, so more signal can be expected. However, single-slice imaging is not suitable for screening purposes, making FAIR unsuitable for breast screening purposes.



Supporting Information Figure 3. Comparison of multi-slice VS-ASL and single-slice/multi-slice FAIR. Multi-slice VS-ASL and single-slice FAIR both show vascular signal (black arrows) that corresponds to vascular signal on the T2-weighted scan (white arrows), while multi-slice FAIR does not. FAIR labeling takes place outside of the field-of-view, and with multi-slice scanning this means transit delays increase. Firstly, blood flow in breast is relatively slow, so not enough ASL-signal has arrived in the region of interest yet at the time of acquisition. Secondly, label decays with T1, so it would also not be an option to match the PLD to the transit delay. Because then most ASL-signal will likely have decayed already. In addition, in contrast to single-slice FAIR there is no contribution of venous signal in multi-slice FAIR. VS-ASL labels based on velocity, non-spatially-selective, also already in the region of interest. So in case of VS-ASL there is no transit delay, making it compatible with a multi-slice readout in breast. Acquisition parameters VS-ASL: the same settings were used as described in the main document; however, the image orientation was changed from transverse to coronal to match the FAIR acquisition. Acquisition parameters FAIR: FAIR used a frequency offset corrected inversion (FOCI) pulses. The selective inversion slab was aligned with the imaging stack, with an additional width of 6 mm on both sides, and inversion time was set to 1200 ms. Single-slice FAIR was acquired using a single slice of 8 mm to achieve the shortest transit delay. Multi-slice FAIR uses the same imaging stack as used for VS-ASL (20 slices with 5 mm slice thickness and 1 mm slice gap) to achieve full breast coverage as required for screening. Acquisition parameters T2-weighted scan: T2-weighted turbo spin echo (TSE) Dixon, 47 slices, acquisition resolution of  $1.2 \times 1.2 \times 2.4$  mm<sup>3</sup>, field of view of  $300 \times 360 \times 123$  mm<sup>3</sup>, TE/TR of 140 ms / 5850 ms.



Supporting Information Figure 4. Histopathology results in two patients. A) Increased number of vessels and increased number of hypertrophic vessels (indicated by black arrows) are observed with a CD 31 vessel wall staining in patient 2 with an 11mm DCIS grade 2 lesion. B) These vessels are not visible in a similar location in the contralateral healthy breast. C) Hypertrophic vessels (indicated by black arrows) at the border of the 22mm invasive carcinoma grade 2 in patient 7, observed with a HE staining. D) These vessels are not visible in a healthy tissue of the same patient. E) CD 31 vessel wall stained section confirming the higher number of vessels at the location of the lesion.



# Chapter 5

---

## **Arterial Spin Labeling using Spatio-temporal Encoding (SPEN) readout for robust perfusion imaging in inhomogenous magnetic fields**

---

S.L. Franklin<sup>1,2</sup>, M. Schuurmans<sup>1</sup>, M. Otikovs<sup>3</sup>, P. Borman<sup>4</sup>, M.J.P. van Osch<sup>2,5</sup>, C. Bos<sup>1</sup>.

<sup>1</sup>Center for Image Sciences, University Medical Center Utrecht, Utrecht, The Netherlands

<sup>2</sup>C.J. Gorter Center for High Field MRI, Department of Radiology, Leiden University Medical Center, Leiden, The Netherlands.

<sup>3</sup>Department of Chemical and Biological Physics, Weizmann Institute of Science, Rehovot, Israel.

<sup>4</sup>Department of Radiotherapy, University Medical Center Utrecht, Utrecht, The Netherlands

<sup>5</sup>Leiden Institute for Brain and Cognition, Leiden University, Leiden, The Netherlands.



## ABSTRACT

**Purpose:** To evaluate the feasibility of spatio-temporal encoding (SPEN) readout for pseudo-continuous ASL (pCASL) in brain, and its robustness to susceptibility artifacts as introduced by aneurysm clips.

**Methods:** A 2D self-refocused  $T_2^*$ -compensated hybrid SPEN scheme, with super-resolution reconstruction, was implemented on a 1.5T Philips system.  $Q (= BW_{\text{chirp}} * T_{\text{chirp}})$  was varied, and, the aneurysm clip-induced artifact was evaluated, in a phantom (label-images) and in-vivo (perfusion-weighted signal (PWS)-maps and temporal signal-to-noise (tSNR)). In-vivo results were compared to gradient-echo echo-planar-imaging (GE-EPI) and spin-echo EPI (SE-EPI). tSNR as a function of repetition time (TR) was compared between SPEN and SE-EPI. SPEN with  $Q \sim 75$  encodes with the same off-resonance robustness and resolution as EPI.

**Results:** The clip-induced artefact with SPEN decreased as a function of  $Q$ , and was smaller than with SE-EPI and GE-EPI in-vivo. tSNR decreased with  $Q$  and the tSNR of GE-EPI and SE-EPI corresponded to SPEN with a  $Q$ -value of approximately  $\sim 85$  and  $\sim 108$ , respectively. In addition, SPEN perfusion images showed a higher tSNR ( $p < 0.05$ ) for  $TR = 4000$  ms compared to  $TR = 2100$  ms, while SE-EPI did not. tSNR remained relatively stable when the time between SPEN-excitation and start of the next labeling-module was more than  $\sim 1000$  ms.

**Conclusion:** Feasibility of combining SPEN with pCASL imaging was demonstrated, enabling cerebral perfusion measurements with a higher robustness to field inhomogeneity ( $Q > 75$ ), at no cost to tSNR and resolution compared to SE-EPI and GE-EPI. Future developments are needed to enable 3D scanning and increase acquisition speed to allow smaller voxel sizes in combination with larger FOVs.

## INTRODUCTION

Arterial Spin Labeling (ASL) is a non-contrast enhanced perfusion method, used for numerous applications both in brain[13], [147] as well as body[19], [62], [125], [148]–[150]. ASL is often used in combination with single-shot acquisition techniques, such as echo-planar imaging (EPI), because of their time efficiency, and motion insensitivity, which is especially important for body applications[19], [62]. However, EPI is especially prone to distortion and chemical shift artifacts in the phase-encoding (PE) direction, due to weak gradients. Many body applications, such as imaging of kidney[62], breast[151], but also brain applications, e.g. in patients with implants[152] or cerebral hemorrhages[153], [154], are characterized by magnetic field distortions, complicating the application of ASL.

Spatio-temporal encoding (SPEN) has been introduced in 2005[155] as an alternative to EPI and can provide increased robustness to magnetic field inhomogeneity in similar acquisition time[63]. In functional[156] as well as diffusion-weighted[157] MRI, SPEN was shown to be superior to EPI in areas associated with susceptibility-effects, such as the (orbito)frontal cortex of the brain[156], [158], breast[157] and in the vicinity of metal implants[159], [160].

SPEN uses a frequency-swept (chirp) pulse in combination with a gradient, which leads to a local excitation, that excites the field-of-view (FOV) over time. This results in a linear relationship between spatial location and time, and thus no Fourier transformation is required in the direction of this excitation gradient. Super-resolution (SR) reconstruction is performed to enable short scan times without compromising on resolution or SAR, compared to EPI[161], [162]. SPEN is characterized by a stronger mean acquisition gradient ( $G_{acq}$ ) as compared to EPI (Figure 1), which reduces image distortion (displacement ( $d$ )) as a result of susceptibility-effects:  $d = \frac{\Delta B_0}{G_{acq}}$ . Sensitivity to susceptibility-effects can further be reduced by full  $T_2^*$ -refocusing of all data, when using appropriate timings. However, the frequency swept pulse in SPEN could potentially saturate incoming blood (i.e. blood below the labeling plane), which would in turn reduce labeling efficiency during the following labeling module, thereby necessitating a longer repetition time (TR) to preserve temporal SNR (tSNR).

In this technical note, the feasibility of combining SPEN with pseudo-continuous ASL (pCASL) for cerebral perfusion imaging was explored: 1) The behavior of SPEN as a function of  $Q$  ( $= BW_{chirp} * T_{chirp}$  [-]), which determines the robustness to susceptibility-effects and SNR, is investigated in the presence of an aneurysm clip, in a phantom, and 2) in-vivo. 3) The perfusion-weighted signal (PWS)-map, in the presence of an aneurysm clip, is compared between SPEN, gradient-echo (GE-)EPI and spin-echo (SE-)EPI. 4) The effect of TR on the temporal signal-to-noise (tSNR) of the PWS-images for SPEN and SE-EPI is investigated.

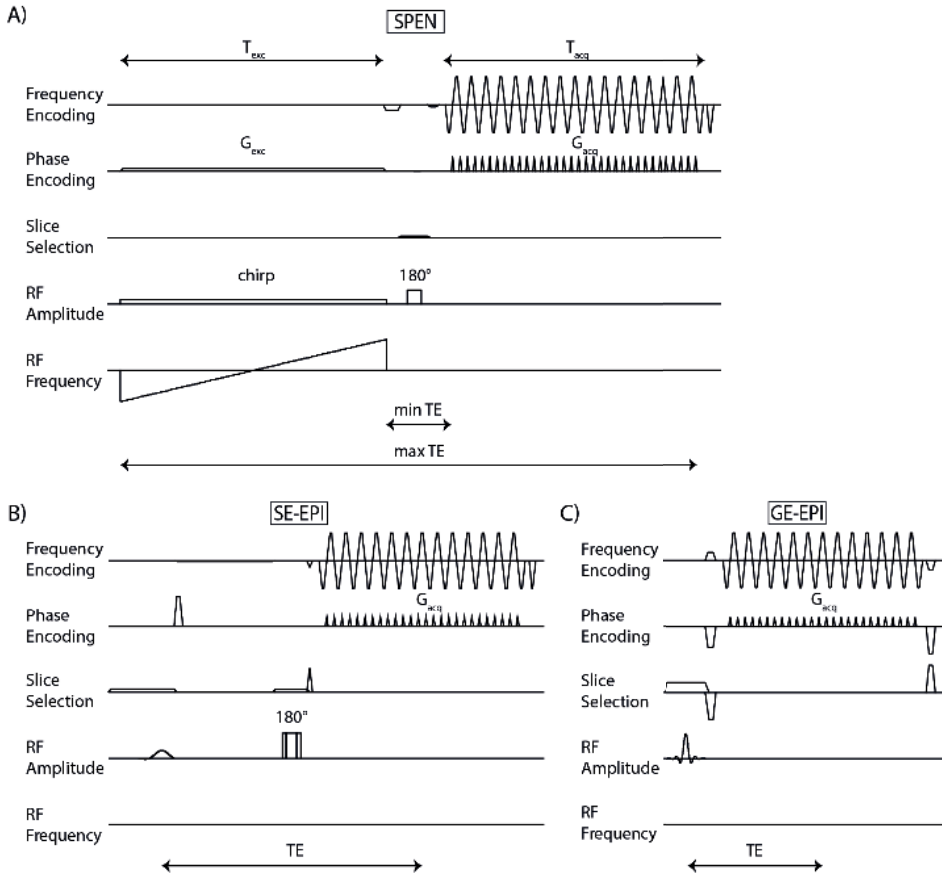


Figure 1. Scaled sequence diagrams for the A) SPEN ( $Q=125$ ), B) SE-EPI, and C) GE-EPI readout, used in this study. The acquisition gradient ( $G_{acq}$ ) in phase-encoding direction, is larger for SPEN compared to GE-EPI and SE-EPI, leading to a larger robustness for magnetic field offsets. For SPEN, the frequency-swept chirp-pulse is used as excitation pulse. The chirp-pulse in combination with the 180-degree refocusing pulse, results in sequentially generated echoes in time, related to different parts of the field-of-view. This leads to a varying  $T_2$ -weighting over the field-of-view: spins that are first excited will have a maximum TE, while spins that are excited last will have felt a minimum TE. The excitation time ( $T_{exc}$ ) was chosen equal to the acquisition time ( $T_{acq}$ ), resulting in full- $T_2^*$  refocusing.

## METHODS

### Data acquisition

This study was approved by the local ethics committee (METC Utrecht, Protocol 15-466) Informed consent was obtained from all participants. Nine healthy volunteers (six females, 26-32 years), were scanned on an 1.5T Philips Achieva scanner (Philips, Best, The Netherlands) using an 8-channel head coil.

A 2D self-refocused  $T_2^*$ -compensated hybrid SPEN scheme was used, where SPEN encoding in the original PE direction, i.e. anterior-posterior, was combined with conventional k-space

encoding in the frequency-direction[63]. The sequence included; a 90-degree chirp-pulse with a duration equal to the acquisition duration ( $T_{\text{chirp}} = T_{\text{acq}} = 20.4$  ms); and a 180-degree spin-echo pulse, positioned symmetrically in between the chirp-pulse and start of acquisition, to ensure complete  $T_2^*$ -refocusing (Figure 1). Depending on  $Q$ ,  $B_1$ ,  $G_{\text{exc}}$  and  $G_{\text{acq}}$  were adjusted according to:  $B_1 = 0.27 * \frac{\sqrt{Q}}{\gamma T_{\text{exc}}}$  [163],  $G_{\text{exc}} = \frac{Q}{\gamma L_{\text{pe}} T_{\text{exc}}}$ , and  $G_{\text{acq}} = \frac{Q}{\gamma L_{\text{pe}} T_{\text{acq}}}$  ( $L_{\text{pe}}$  = field-of-view in SPEN-direction). SPEN was acquired with a field-of-view (FOV) of 200 x 200 mm, slice thickness of 10 mm, voxel size of 3.1 mm in read-direction, and  $\Delta y_{\text{spen}}=5.7$  mm in SPEN-direction, which is defined by the shift of the quadratic phase-profile between readout lines. This results in a TE range of 5-45 ms over the FOV. All scans were acquired with slope sampling turned off, and all in-vivo scans were acquired with Spectral Presaturation with Inversion Recovery (SPIR) fat suppression.

For all in-vivo scans, separate  $M_0$ -images were acquired with the same readout and  $Q$ -value setting, by turning ASL labeling off and  $TR=2000$  ms, resulting in durations of 8 s.

### Experiment 1:

A phantom and aneurysm clip (titanium, 2 cm), see Supporting Information Figure 1, were placed in water doped with 0.4 mM Gd. SPEN was acquired with  $Q$ -values of; 50, 75, 100, 12, 150 and 200, each corresponding to an off-resonance robustness (BW/mm) of 12.3 Hz/mm, 18.3 Hz/mm, 24.7 Hz/mm, 30.7 Hz/mm, 36.6 Hz/mm and 49.4 Hz/mm. This series was acquired with and without SPIR.

### Experiment 2:

Two healthy volunteers were scanned with the aneurysm clip, positioned on the forehead and fixated by tape. ISPEN was acquired with  $Q$ -values; 50, 75, 100, 125, and 150. In volunteer 2, an image with  $Q = 175$  was additionally acquired, corresponding to 43.0 Hz/mm.

SE-EPI and GE-EPI-scans were acquired with the same FOV and slice thickness, acquired voxel size of 3.1 mm x 3.0 mm, SENSE factor of 1.3, and  $TR$  of 4000 ms. The  $TE$  was 17 ms, and 9.1 ms, for SE-EPI and GE-EPI, respectively. These settings correspond to a BW/mm of 18.7 Hz/mm. So, the off-resonance robustness, and thus PE/SPEN bandwidth, of SE-/GE-EPI is similar to SPEN with  $Q=75$ . Meaning that the resolution of SPEN with  $Q \geq 75$  after SR-reconstruction is as least as high as EPI[164].

These scans were acquired with pCASL labeling duration of 1800 ms, background suppression, and post-label delay (PLD) of 1800 ms and 30 repetitions. Background suppression included presaturation of the imaging stack just before start of labeling, and two non-selective hyperbolic secant pulses at 2250ms and 3150ms after presaturation. The total scan duration was 4 min 16 s for SPEN and SE-EPI, and 4 min 8 s for GE-EPI-scans.

In addition, in volunteer 2, a  $T_1$ -weighted scan without the aneurysm clip was acquired, using multi-slice single-shot SE-EPI, FOV of 230 x 183mm, voxel sizes of 0.9 x 1.12 x 5 mm, 21 slices, and TR/TE of 570 ms/15 ms.

### Experiment 3:

In the same volunteers of experiment 1, additional pCASL-scans with SPEN, SE-EPI and GE-EPI readout were acquired without an aneurysm clip positioned on the forehead, using the same settings. SPEN was acquired with  $Q=125$  and  $Q=175$  for volunteer 1 and 2, respectively.

### Experiment 4:

Six volunteers were scanned with a series of SPEN and SE-EPI-scans, where TR was varied according to: 2100 ms, 2300 ms, 2600 ms, 3000 ms, 3500 ms, and 4000 ms. SPEN-scans were acquired with  $Q=50$  (12.4 Hz/mm). For the SE-EPI scans, the same settings were used as described in experiment 2. Scans were acquired with a labeling duration of 1000 ms, PLD of 1000 ms, and 30 repetitions. Scan durations were the same for SPEN and SE-EPI, ranging between 2 min 14 s and 4 min 16 s for TRs of 2100 ms and 4000 ms, respectively. Background suppression was turned off. In addition, a  $T_1$ -weighted scan was acquired.

### Data analysis

K-space data of the SPEN-images were exported from the scanner, and pre-processing, up to (not including) the Fourier-transformation, of the data was done using ReconFrame (Gyrottools, Zurich, Switzerland). The data was reconstructed following steps described by Seginer et al[165], by adapting the algorithm[166], where instead of L2-regularized iterative reconstruction used in reference[166], final images were obtained by a multiplication with a SR matrix[64].

Co-registration and motion correction was performed using a rigid PCA-based registration method[114] using Mevislab (MeVis Medical Solutions, Bremen, Germany). SPEN, SE-EPI and GE-EPI-scans were all separately co-registered to the  $T_1$ -scan. Perfusion-weighted maps were calculated using:

$$\Delta S_i = \frac{1}{R} \sum_{r=1}^R (C_{r,i} - L_{r,i}) \quad (1)$$

$$PWS_i[\%] = \frac{\Delta S_i}{M_{0,i}} \quad (2)$$

Where:  $C_{r,i}$  = control-image,  $L_{r,i}$  = label-image,  $r$  = repetitions,  $i$  = voxels,  $\Delta S_i$  = subtraction-image,  $M_{0,i}$  = the scan used to calibrate the ASL-signal according to the expected blood signal[13]. Brain masks, used for visualization of the PWS-maps, were generated using SPM (Wellcome

Center for Human Neuroimaging, London, United Kingdom), based on the  $M_0$ -scans acquired without aneurysm clip. GM segmentation was performed on the  $T_1$ -weighted scans using SPM(using >70% GM contribution)

tSNR maps were generated using:

$$tSNR_i = \frac{\mu_{\Delta S,i}}{\sigma_{\Delta S,i}} \quad (3)$$

Where  $\mu_{\Delta S,i}$ = mean ASL-signal over all repetitions, and  $\sigma_{\Delta S,i}$ = standard deviation over time. The tSNR in GM was calculated by averaging the tSNR in all GM voxels.

### Experiment 1

Label-images were generated for each Q-value.

### Experiment 2

Label-images,  $M_0$ -images, PWS-maps, and tSNR-maps were generated for each Q-value. To calculate mean tSNR in GM, the part of the FOV containing the clip-induced artifact was omitted from the GM-mask, by taking out a square of 1/3 of FOV. To compare the tSNR in GM of SPEN, GE-EPI and SE-EPI, the tSNR of the EPI-images was corrected by a factor  $\Delta y_{SPEN}/\Delta y_{EPI}$  to compensate for the smaller voxel sizes, with  $\Delta y_{EPI}$  the acquired voxel size of the EPI-scans.

### Experiment 3

Label-images and PWS-maps were generated for SPEN, SE-EPI and GE-EPI with and without aneurysm clip.

### Experiment 4

tSNR maps, and the average tSNR in GM over all volunteers was calculated for each TR, for SPEN and SE-EPI. A non-parametric Wilcoxon rank sum test ( $\alpha=0.05$ ), was used to test whether the tSNR of TR=2100 ms was significantly different from TR=4000 ms.

## RESULTS

A higher Q-value decreases the aneurysm clip-induced artefact, as demonstrated in a phantom, see Figure 2A. This effect reduces when using SPIR, see Figure 2B. In both cases, additional through-plane slice-selection effects lead to signal voids near the aneurysm clip, see Supporting Information Figure 1. In-vivo, SPIR was deemed necessary, and thus the effect of Q on the clip-induced artefact size is reduced, see Supporting Information Figure 2.

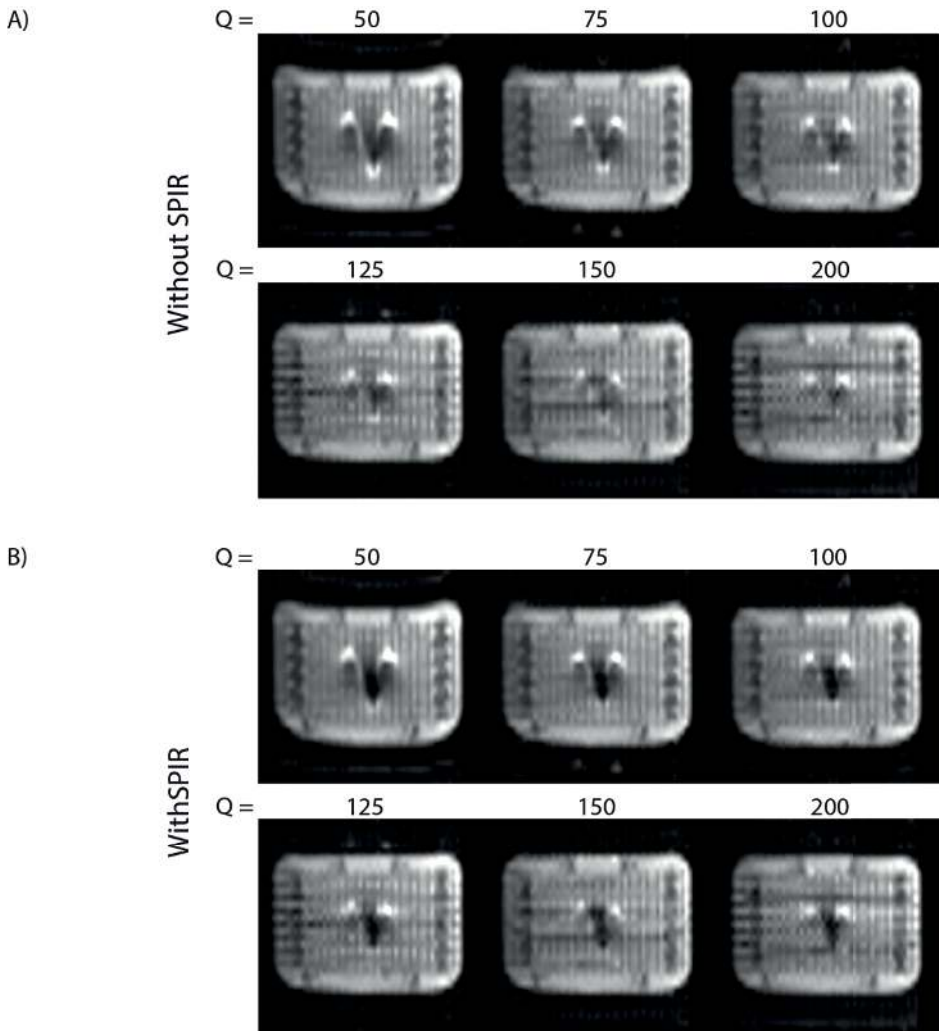


Figure 2. Phantom with aneurysm clip, acquired with a SPEN-readout at different Q-values (50,75,100,125,150,200), A) without SPIR fat suppression, B) with SPIR fat suppression. The artefact induced by the aneurysm clip is reduced for higher Q-values (A). This effect becomes less apparent when using SPIR fat suppression (B). Signal intensity is normalized per Q-value to facilitate comparison of field inhomogeneity effects between the images.

The label-images show some ghost artifacts for higher Q-values ( $> \pm 125$ ), indicated by black arrowheads in Supporting Information Figure 2A. The tSNR of the PWS-images shows a  $1/\sqrt{Q}$ -relation, and the tSNR of SE-/GE-EPI correspond to the tSNR of SPEN with  $Q=108/85$  respectively, see Figure 3.

The aneurysm clip-induced artifact is smaller for the SPEN compared to SE-/GE-EPI, and SE-EPI and GE-EPI show additional artifacts, see Figure 5. In the PWS-maps, small subtraction

artifacts can be observed at the location of the aneurysm clip for SE-EPI and GE-EPI, which are not visible for SPEN, see Figure 4.

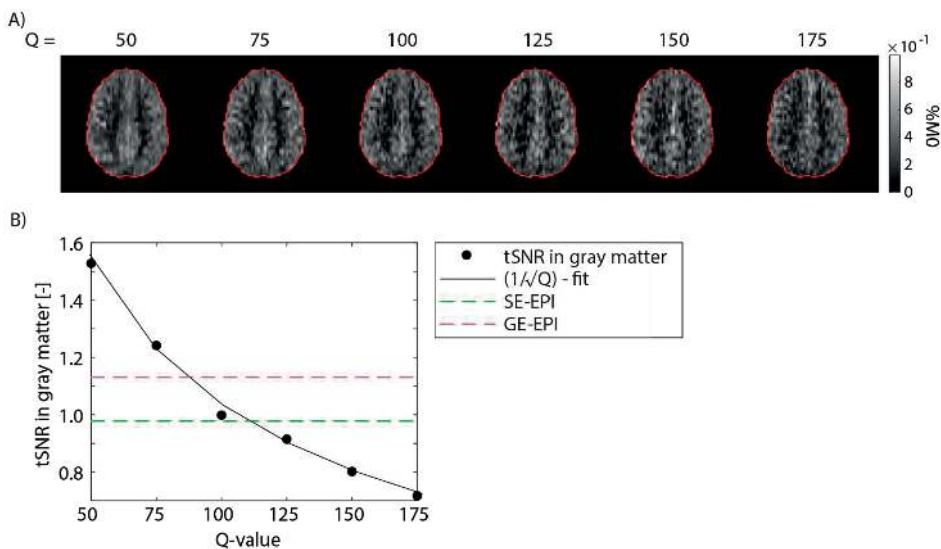


Figure 3. A) SPEN perfusion-weighted signal (PWS)-images at Q-values between 50-175. B) Mean temporal SNR (tSNR) in gray matter as a function of Q-value. The data is fitted with a  $1/\sqrt{Q}$ -function. The tSNR-value of SE-EPI and GE-EPI, corrected for acquisition voxel size, are illustrated with a dotted line in green and magenta, respectively.

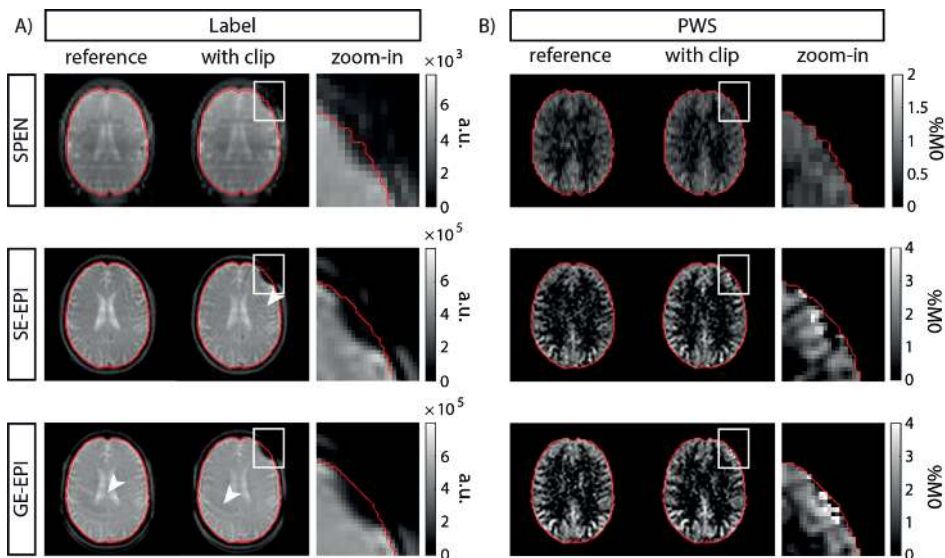


Figure 4. Comparing the effect of an aneurysm clip on SPEN with  $Q = 125$ , SE-EPI and GE-EPI. A) pCASL label images, and B) perfusion-weighted signal (PWS) maps, without (reference) and with (with clip) aneurysm clip. The last column shows a zoom-in of the artifact area, of which the exact location is depicted by the white square. The clip-induced artifact is smaller for SPEN compared to SE-EPI and GE-EPI. In addition, SE-EPI showed a Gibbs ringing artifact anterior to the aneurysm clip, and GE-EPI showed ghost artifacts, both indicated by white arrows.



tSNR increases noticeably with TR for SPEN, see Figure 5A. This trend was confirmed by quantitative evaluation of tSNR over all volunteers, see Figure 5B. tSNR was significantly different between the TR=2100 ms and TR=4000 ms for SPEN ( $p = 0.026$ , median difference = 0.551), and not for SE-EPI ( $p = 0.240$ , median difference = 0.207).

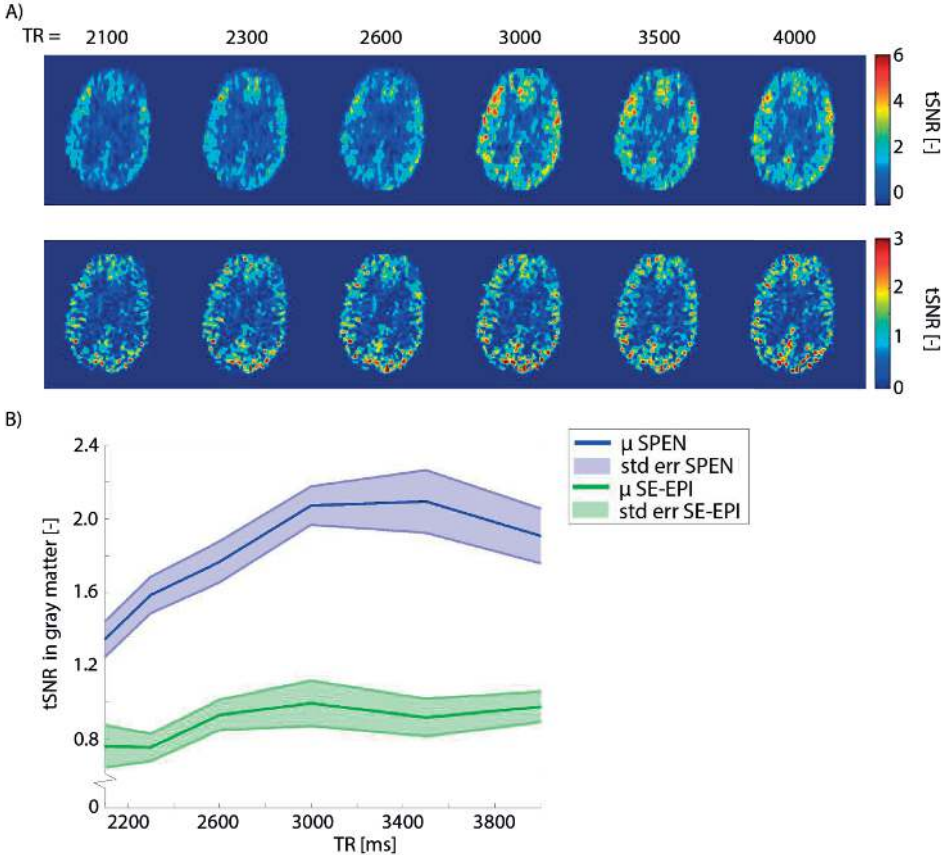


Figure 5. A) Effect of TR on SPEN and SE-EPI for a representative volunteer. B) Mean ( $\mu$ ) normalized tSNR in gray matter over all volunteers as a function of TR, for SPEN (blue) and SE-EPI (green). tSNR was normalized with respect to the value at a TR of 4000 ms. The shaded area represents the standard error (st. err.) of tSNR.

## DISCUSSION

Results showed the feasibility of SPEN in pCASL imaging, enabling cerebral perfusion measurements with a higher robustness to susceptibility-effects compared to SE-/GE-EPIPI, at no cost to tSNR or resolution, by using the appropriate Q-value. The  $1/\sqrt{Q}$ -relation between tSNR of SPEN and Q-value, as previously derived in reference[162], was confirmed. Furthermore, a dependence on TR was observed for pCASL-images acquired with SPEN.

meaning that every acquired point was close to being completely refocused (instead of just the center of k-space), reducing signal loss due to  $T_2^*$ [63]. Experiment 1 and 2 showed that SPEN had a smaller clip-induced artifact than SE-EPI and GE-EPI, for all Q-values, confirming the higher robustness to field-inhomogeneity of SPEN. Similar as was observed in the vicinity of metallic implants[160]. Increasing Q results in stronger acquisition gradients[64], so smaller distortions as a result of field inhomogeneities are expected. Results showed a reduction in the clip-induced artefact for higher Q-values, evidencing a higher robustness to susceptibility-effects. In-vivo, the clip-induced artifact remained relatively stable over Q. This is likely mainly due to the suppression of water signal, caused by sensitivity to off-resonance of SPIR, as well as through-plane effects caused by distorted excitation profiles[167] due to limited bandwidth of the slice-selective refocusing pulse, both demonstrated in the phantom data. SPEN enables robust imaging via two mechanisms: SPEN has a stronger  $G_{acq}$  resulting in reduced image distortions as a result of susceptibility-effects[63]. Secondly, SPEN was acquired in full-refocusing mode,

tSNR in GM of SPEN dropped according to  $1/\sqrt{Q}$ , confirming the theoretical derivation by Ben-Eliezer et al[162]. With Q the quadratic phase-profile narrows, resulting in a lower SNR. Using the current settings, the GM tSNR of SE-EPI and GE-EPI corresponded to SPEN with a Q-value of approximately  $\sim 85$  and  $\sim 108$ , respectively, based on the  $1/\sqrt{Q}$ -curve. Importantly, the  $G_{acq}$  of SPEN is higher than of SE-/GE-EPI, at  $Q=85$  and  $108$ , since the BW/mm of SE-EPI and GE-EPI corresponds to  $Q\sim 75$ . Meaning that if  $Q \geq 75$  and  $Q \leq 108$  (SE-EPI) or  $Q 85 \leq$  (GE-EPI) SPEN can produce perfusion images with higher robustness to field homogeneities, at no cost to tSNR and resolution.

For  $Q \geq \pm 125$ , ghost artifacts were observed. They are a result of the SR reconstruction and are akin to Nyquist ghosts seen in EPI-readouts[165]. These artifacts can be prevented by acquiring more points in the SPEN-direction or by using alternative post-processing techniques[168]. However, the former would inevitably increase ASL-signal loss due to  $T_2$ -decay. The longest TE in SPEN is equal to  $T_{exc} + T_{acq} + TE_{min}$  (time in between the chirp-pulse and the start of acquisition, see Figure 1). So the requirement to limit TE results in constraints on the maximum achievable FOV and acquisition matrix. Multi-shot 2D SPEN[160] could be an alternative, but in line with most common body ASL protocols[169], we opted to stick to a single-shot readout. In contrast to SPEN, voxel sizes of SE-/GE-EPI could be chosen smaller without a large penalty on TE, partly due to the use of parallel imaging. Recent developments exploring parallel imaging methods for SPEN have been introduced, e.g. by simultaneously acquiring separate parts of the FOV using multi-band chirp pulses[157], [161], [170] or by acquiring low-resolution images and employing k-space interpolations, based on multiple-receivers, to increase resolution[164].

Experiment 3 furthermore demonstrated that, when using a short pCASL labeling duration and PLD to become sensitive to the start of the bolus, a higher tSNR for SPEN is observed at longer TRs, which was not the case for SE-EPI. Background suppression was turned off to prevent additional effects on the signal-evolution. The tSNR of SPEN followed a recovery-like pattern over TR, approaching an equilibrium for long TR ( $> 3000$  ms). The results are in accordance with the hypothesis that the chirp-pulse of the previous SPEN readout saturates incoming blood, anterior to the labeling slab, thereby reducing pCASL labeling efficiency. Increasing the TR, and thus the time between end of the SPEN-readout and start of labeling, allows the inflow of fresh blood, removing this effect. From a TR of approximately 3000 ms, i.e. a pause of 920 ms, this effect was negligible, showing that sufficient fresh inflow, together with relaxation, can mitigate the saturation effects.

## LIMITATIONS

All scans were performed at 1.5T, even though most ASL is performed at 3T. As ASL is increasingly being used for body applications, studies will more frequently be done at 1.5T. The advantages of smaller  $B_0$ - and physiological artefacts might outweigh the SNR-loss and shorter  $T_1$  of blood. In addition, when scanning patients with implants the lower field strength might be advantageous. Still, it would be interesting to investigate the performance of SPEN at 3T in future studies.

A single-slice 2D SPEN sequence was used. The use of a frequency swept pulse is inherently challenging to combine with multi-slice imaging. Various approaches for multi-slice and 3D imaging have been published, while SAR and SNR limitations are considered [161], [171]–[173], providing an interesting future direction to enable whole-brain ASL with SPEN in an acceptable scan time.

In the comparison between SPEN, and SE-/GE-EPI, a relatively high Q-value (=125) was used for SPEN, meaning that the encoded resolution was higher for the SPEN than the EPI-readouts. This inevitably resulted in lower PWS-values for SPEN. Importantly, it is possible to acquire SPEN without a penalty on resolution and tSNR while preserving the smaller clip-induced artifact.

Next to EPI, other readouts are used for ASL. In brain, 3D segmented methods, such as relaxation enhancement (RARE) stack of spirals or GRASE are recommended[13], which are more robust to field inhomogeneity than EPI[174], [175]. Also in body ASL, RARE with various approaches to shorten acquisition time[176], [177] and single-shot 3D GRASE have been introduced[18]. Phase-encoded xSPEN has previously been shown to have similar resolution

and SNR as RARE, but in half the scan time[178]. Future studies making a direct comparison between SPEN and RARE approaches are necessary. The current study focused on brain measurements in the presence of an implant, as a first attempt for SPEN-ASL. For future studies, it would be interesting to combine SPEN with ASL in body applications.

#### Conclusion

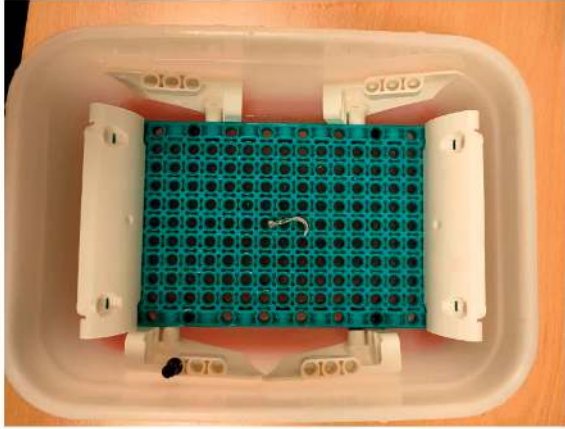
The study showed the feasibility of SPEN-ASL and demonstrated the performance in the vicinity of an aneurysm clip implant. In addition, considerations have been raised concerning a minimal pause of  $\sim 1000$  ms between the SPEN-excitation pulse and the start of the next labeling module. ASL-images acquired with SPEN benefit from a higher robustness to field inhomogeneity. By choosing an appropriate Q-value, there is no cost to tSNR or resolution, when comparing it to SE-EPI and GE-EPI. However, developments need to be made to increase acquisition speed, to allow smaller voxel sizes in combination with larger FOVs, and enable 3D-scanning.

## ACKNOWLEDGEMENTS

We would like to thank Lydiane Hirschler for her support in this project.

# SUPPORTING INFORMATION FIGURES

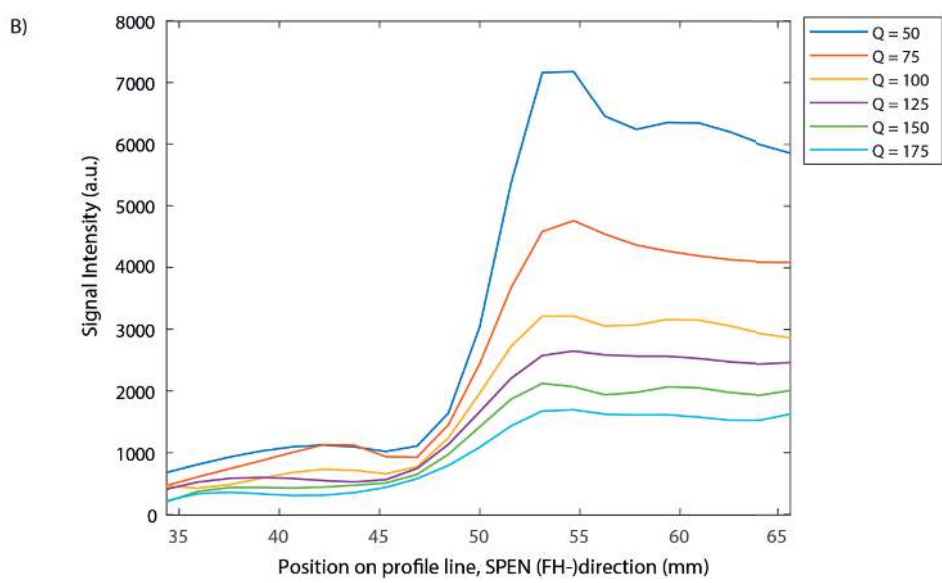
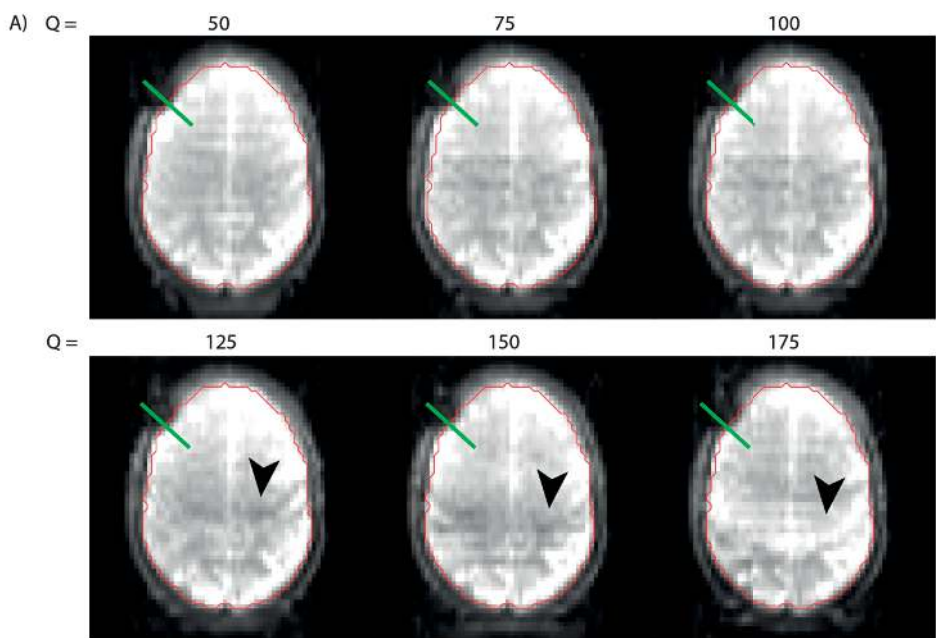
A)



B)



Supporting Information Figure 1. A) Titanium aneurysm clip (2 cm), used in the phantom and in-vivo scans, placed on the phantom; a plastic grid with 8.0 mm periodicity. B) Reformat demonstrating the distortion of the slice profile, indicated by white arrowheads, of the phantom as shown in A). Images were to demonstrate the through-plane effect.



Supporting Information Figure 2. SPEN label-images for Q-values ranging between 50 and 175. A) SPEN Label images, edge artifacts are visible for higher Q-values as a result of too few measurement points, indicated by black arrowheads B) Intensity profiles along the green line in A, for all Q-values, using a spline interpolation with a factor of 2. The intensity step remains roughly at the same location for the different Q-values.

# APPENDIX: THEORETICAL BACKGROUND OF SPATIO-TEMPORAL ENCODING

Single-shot echo planar imaging (EPI) is an often used readout method in ASL. It is mainly used because of its time efficiency and motion insensitivity, which is especially important in body imaging[19], [62]. However, the speed of EPI comes at the cost of  $B_0$ -sensitivity, especially in the phase-encoding direction. It can present itself as various artifacts: distortion; due to local changes to the Larmor frequency, chemical shift; due to shielding effects in the molecular environment of the hydrogen nuclei, and signal drop out; due to increased intra-voxel spin-dephasing which shortens the local  $T_2'$ [179].

Distortion and chemical shift artifacts occur because the strength of the acquisition gradient in phase-encoding direction  $G_{acq}$  is relatively small[179]. Which means that if there is a small deviation in the main magnetic field  $\Delta B_0$ , it leads to a large displacement  $\Delta d$ . For simplicity we will assume a constant gradient:

$$\Delta d = \frac{\Delta B_0}{G_{acq}} \quad (1)$$

The resolution in the phase-encoding direction in EPI is determined by the strength of the acquisition gradient  $G_{acq}$ . Note, here  $G_{acq}$  is defined as the time-averaged gradient, so the gradient blips are not taken into account:

$$G_{acq} = \frac{N_{pe}}{\gamma L_{pe} T_{acq}} \quad (2)$$

Where  $N_{pe}$  and  $L_{pe}$  are the number of voxels and FOV in the phase-encoding direction, respectively, and  $T_{acq}$  is the acquisition time.  $T_{acq}$  is usually minimized, based on hardware constraints. This means that  $G_{acq}$  can only be increased further by decreasing  $\Delta y_{pe}$ , which is often not possible without decreasing the FOV in phase-encoding direction, which could lead to fold-in artifacts.

Signal dropout can occur due to increased  $T_2'$ -dephasing, as a result of increased spin-spin interactions when there are large variations in the local magnetic field e.g. at air-water interfaces. Dephasing due to static field inhomogeneities can be compensated by spin-echo approaches to a certain degree; only the center of k-space is completely refocused and dephasing due to temporally changing interactions, i.e. diffusion effects, can never be refocused.

All of these artifacts; distortion, chemical shift and signal dropout are addressed in spatio-temporal encoding (SPEN). In SPEN  $G_{acq}$  does not depend on  $\Delta y_{pe}$ , as in EPI[63]. Thereby, the use of a larger  $G_{acq}$  is enabled, reducing distortion and chemical shift artefacts. In addition,

SPEN can be employed in the full-refocusing mode where every data point is refocused instead of just the center of k-space, reducing signal drop out[63].

In SPEN, excitation is performed using a combination of a frequency swept chirp pulse with a gradient, see Figure 1a. The linear dependency of frequency on space leads to a quadratic phase profile[180]. The quadratic phase profile results in excitation of the spins which are located at the vertex of the quadratic phase profile, while the spins located further away from the vertex undergo rapid dephasing. This point of excitation will move over the FOV linearly in time due to  $G_{exc}$ , resulting in a sequential excitation of voxels in time. Spins acquire a phase build-up during excitation by  $G_{exc}$ , depending on spatial location. This phase build-up is unwound sequentially by blips of  $G_{acq}$  during acquisition to create an echo, according to[64]:

$$G_{exc}T_{exc} = G_{acq}T_{acq} \quad (3)$$

Where  $G_{exc}$  and  $T_{exc}$  are the gradient strength and duration of the frequency-swept CHIRP pulse, respectively, and  $T_{acq}$  is the acquisition time.  $G_{exc}$  is defined as:

$$G_{exc} = \frac{BW_{exc}}{\gamma L_{pe}} = \frac{Q}{\gamma L_{pe} T_{exc}} \quad (4)$$

Where  $L_{pe}$  is the FOV in phase-encoding direction and  $Q$  is defined as:

$$Q = BW_{exc} T_{exc} \quad (5)$$

Using equation 3 and 4:

$$G_{acq} = \frac{Q}{\gamma L_{pe} T_{acq}} \quad (6)$$

So when scanning SPEN,  $Q$  needs to be  $> N_{pe}$ , to benefit from less distortions compared to EPI, see equation 2. Another benefit of using SPEN is that if  $T_{exc}$  is chosen such that:

$$T_{exc} = T_{acq} \quad (7)$$

and the 180-degree refocusing pulse is placed symmetrically between  $G_{exc}$  and  $G_{pe}$ : all spin packages will refocus exactly at the time of their readout. This results in full  $T_2'$ -refocusing in phase-encoding direction, preventing signal loss due to dephasing[63]. Furthermore,  $T_{exc}$  and thus  $T_{acq}$  should be kept to a minimum for a given  $Q$ , to prevent signal loss due to  $T_2$ -decay. This provides a challenge for ASL body applications, where the desired FOV is usually relatively large.

The variable  $Q$  will determine the sweep rate  $R$  of the chirp pulse, see equation 6, and the sweep rate  $R$  will in turn determine the spatial width  $\Delta y_{exc}$  of the excitation for each measurement point[64].



$$R = \frac{BW_{exc}}{T_{exc}} = \frac{Q}{(T_{exc})^2} \quad (8)$$

$$\Delta y_{exc} = \frac{\sqrt{R}}{\gamma G_{exc}} \quad (9)$$

It is important to note here that  $\Delta y_{exc}$  does not determine the voxel size  $\Delta y_{pe}$ . The width of excitation  $\Delta y_{exc}$  will determine the locality of spins that are excited for the measurement of one voxel, and thereby the encoded resolution and SNR[64]. A wider excitation will generate more signal, but will also create blurring as more signal of neighboring spins will be excited. With the use of super-resolution reconstruction[64] the acquired signal can be de-convolved, using the simulated excitation profile, to remove this blurring. When using super-resolution reconstruction it is beneficial to use a larger  $\Delta y_{exc}$ , so that multiple excitations can be averaged for one voxel, increasing SNR and allowing similar SNR-levels as EPI[156], [162]. So to increase SNR,  $R$ , and thus  $Q$ , should be minimized, since  $T_{exc}$  ( $=T_{acq}$ ) is constrained by hardware. This poses a trade-off with robustness to field inhomogeneity, which requires a higher  $Q$  to increase  $G_{pe}$ . The optimal  $Q$  is the minimum value that provides robustness to the envisioned  $\Delta B_0$ , and thus is dependent on the application.

Because the FOV is not excited at one instant in time the relationship between required  $B_1$  for a certain flip angle  $\theta$  is more complex, and is determined by simulations. For a  $\theta = \frac{\pi}{2}$  this results in[163]:

$$B_1 = 0.27 * \frac{\sqrt{R}}{\gamma} \quad (10)$$





# Chapter 6

---

## **$B_0$ and $B_1$ influence on velocity selective inversion arterial spin labeling and background suppression efficiency**

---

Suzanne L. Franklin<sup>1,2,3</sup>, Matthias J. P. van Osch<sup>1,3</sup> PhD, Clemens Bos<sup>2</sup> PhD.

<sup>1</sup>C.J. Gorter Center for High Field MRI, Department of Radiology, Leiden University Medical Center, Leiden, The Netherlands

<sup>2</sup>Center for Image Sciences, University Medical Centre Utrecht, Utrecht, The Netherlands

<sup>3</sup>Leiden Institute for Brain and Cognition, Leiden University, Leiden, The Netherlands



## INTRODUCTION

Arterial Spin Labeling is more and more used outside of the brain [19], [97], [176]. For applications in the body, flow-based ASL techniques are particularly suited, because of the easier planning procedure due to non-spatially selective labeling, and transit time insensitivity. These techniques thus enable, or simplify, ASL measurements in organs which are fed by multiple feeding vessels, and organs with relatively slow flow. In brain[53], [148], velocity selective inversion ASL (VSI-ASL) has demonstrated the highest SNR of flow-based ASL techniques thus far.

In the body, however, magnetic field inhomogeneity will start to play a role in optimization of the ASL-sequences. In a previous study we have demonstrated severe subtraction errors of VSI-ASL in some volunteers, when applied in the kidneys[148]. The subtraction errors are likely due to  $B_0/B_1$ -inhomogeneity of both the VSI-ASL module and the background suppression (BGS) pulses.

In the original implementation of VSI-ASL[53], the label module is velocity-sensitive, containing bipolar motion-sensitizing gradients, and the control module is velocity-compensated, containing unipolar gradients, see Figure 1A and B. The velocity-compensated control module prevents subtraction errors because it compensates for the diffusion contribution to the signal[53]. The downside, however, is that the velocity-compensated control module is associated with a relatively high  $B_1$ -sensitivity, which already limits inversion of static tissue for  $B_1$ -ranges encountered in brain[53]. This  $B_1$ -sensitivity is expected to lead to even more degradation of image quality in body applications, probably to the level that clinical interpretation is hampered. In addition, the velocity-selective inversion pulse train consists of hard pulses, which are increasing the sensitivity to  $B_1$  imperfections even further[53].

Besides the  $B_1$ -sensitivity of the VSI-ASL modules,  $B_1$ -sensitivity of the BGS pulses also plays a role when applying VSI-ASL in kidneys[148], and as such, likely also in other abdominal applications. The purpose of BGS is to minimize the static background signal intensity in both the label and control image, while conserving the difference in magnetization between label and control due to labeled blood[13]. BGS reduces fluctuations in the ASL-signal, which are caused by e.g. patient motion and physiological noise. BGS consists of a certain number of inversion pulses, which causes all signal to undergo  $T_1$ -recovery based on the tissue's  $T_1$  value. Image acquisition is timed close to the zero-crossing of the dominant background tissue signals[13]. Dixon et al. first proposed the use of multiple inversion pulses to minimize signal of tissues with a range of  $T_1$ 's[181]. However, the BGS pulses do not have a perfect inversion efficiency, resulting in transverse relaxation of the signal, and corresponding signal loss. Thus, the choice for the number of pulses creates a trade-off between signal loss and the width of the

suppressed  $T_1$ -range[13]. For most body ASL methods, two BGS pulses are used, but VSI is typically used with three. In VSI-ASL, static tissue is inverted, so to prevent inversion of the static tissue signal during image acquisition, VSI-ASL is employed with an odd number of BGS pulses. The higher number of BGS pulses in VSI-ASL, makes the sequence particularly sensitive to the inversion efficiency of the BGS pulses.

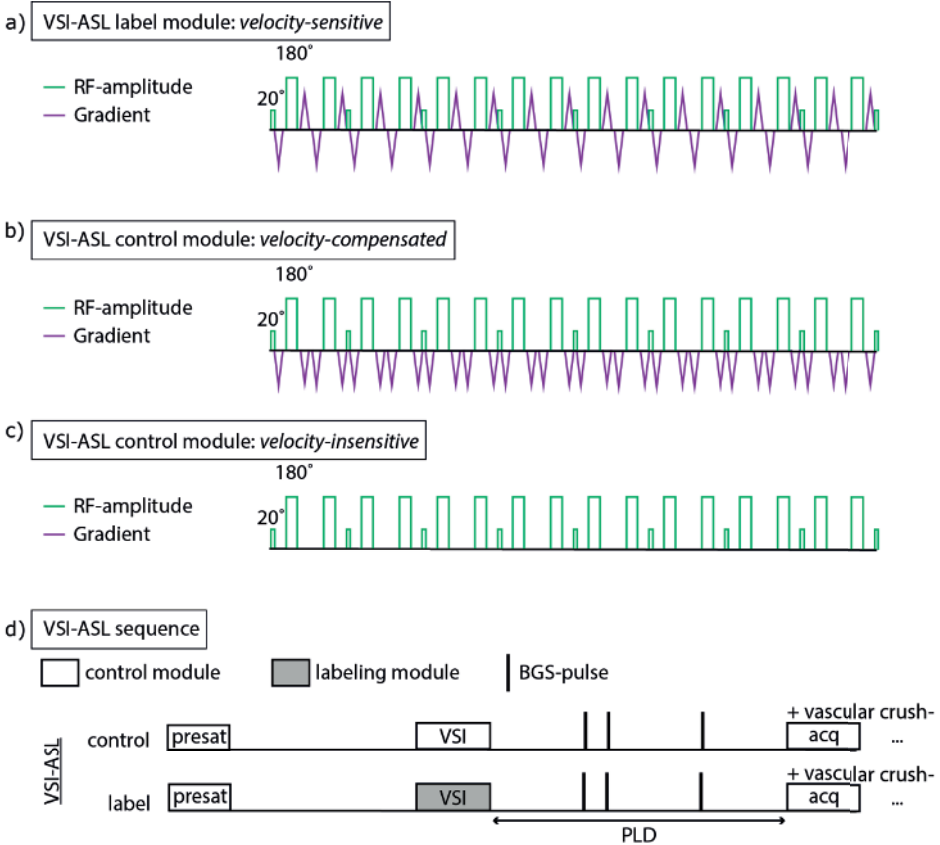


Figure 1. Velocity-selective inversion arterial spin labeling (VSI-ASL) label and control modules. A) The VSI-ASL label module is velocity-sensitive pulse train; containing alternating motion-sensitizing gradients. B) The traditional implementation of the VSI-ASL control module is velocity-insensitive and does not contain any gradients. C) The velocity-compensated VSI-ASL control module contains solely unipolar gradients. D) The VSI-ASL sequence, including presaturation of the imaging volume (presat) and three background suppression (BGS-) pulses.

The hyperbolic secant pulse (HS) is an adiabatic pulse frequently used for BGS[182]. Besides the HS, multiple other adiabatic inversion pulses exist[183], each with varying sensitivity to  $B_0$  and  $B_1$ .  $B_1$  insensitive rotation (BIR)-4[184] is for example an often used pulse, which has been developed to perform non-selective inversion in a  $B_1$ -inhomogenous environment[184]. Frequency offset corrected inversion (FOCI)[185] is another often used inversion pulse, which

has been developed to be robust for off-resonance effects[185], and has since e.g. been used as spatially-selective inversion pulse in ASL-applications[186].

The goal of the current study was to first gain insight into the sensitivity of the different parts of the VSI-ASL sequence to B<sub>0</sub>-/ and B<sub>1</sub> inhomogeneity, specifically including BGS, evaluated for B<sub>0</sub>-/ and B<sub>1</sub> conditions representative for abdominal application at 3T. Secondly, we aim to investigate whether adjustments can be made to improve the robustness to field inhomogeneity. Simulations were performed of the VSI-ASL label and control modules under realistic B<sub>0</sub> and B<sub>1</sub> field conditions, where a distinction was made between velocity-compensated and velocity-insensitive control modules. In addition, the inversion efficiency of the traditionally used BGS pulse, HS, as well as two possible alternatives, BIR-4 and FOCI, was investigated for the same range of field conditions, at two maximum B<sub>1</sub>-levels, to find out which BGS pulse is most suitable for abdominal applications at 3T.

## METHODS

All simulations were performed based on 3T conditions, using a T<sub>1</sub> = 1650 ms[187] and T<sub>2</sub> = 150 ms[188] of arterial blood. The B<sub>0</sub> and B<sub>1</sub> range were based on the field inhomogeneity that can be expected for anatomies in the vicinity of the lungs[127], [128], [145]. The B<sub>0</sub> was varied between -300 and +300 Hz, the B<sub>1</sub> was varied between 0.4 and 1.2 (= 40%/120% of the intended B<sub>1</sub>).

First, Bloch-simulations for the inversion efficiency of VSI-ASL label and velocity-compensated/ velocity-insensitive control modules were performed at a velocity range of -20 cm/s to 20 cm/s.

Second, optimization of BGS pulse parameters was done based on a constrained nonlinear optimization algorithm, with sum of squares as loss function. The optimization parameters were pulse duration, maximum B<sub>1</sub> and maximum frequency offset for all pulses. BIR-4 additionally had the phase-step (defining the flip angle) and  $\beta$  (defining the shape)[184] as parameters.

The BGS pulse optimizations were performed for two different maximum B<sub>1</sub>-conditions: 13.5  $\mu$ T, which is the maximum B<sub>1</sub> that can be used on our 3T Philips system with a body transmit coil, and 23  $\mu$ T, as has been used in previous implementations of BIR-4[57]. The other constraints included a maximum duration of 30ms, maximum frequency offset of 1 MHz, a maximum phase-step of  $\pi$ , and a maximum  $\beta$  of 200.

Starting values of the HS pulse were set to the standard values as implemented by the vendor on our 3T Philips system, see Table 1. For the BIR-4 pulse, the starting values were set to the



settings used by Guo et al[57]. For the FOCI pulse, the starting values were set to the settings that were used previously by our group when implemented as labeling pulse in a flow-sensitive alternating inversion recovery (FAIR) ASL-sequence[108], [145]. The starting values of the maximum  $B_1$  were always set to the maximum available  $B_1$ , i.e. either 13.5  $\mu\text{T}$  or 23  $\mu\text{T}$ .

Parameter	Standard setting	Optimized with max $B_1$ of 13.5 $\mu\text{T}$			Optimized with max $B_1$ of 23 $\mu\text{T}$		
	HS	HS	BIR-4	FOCI	HS	BIR-4	FOCI
Max $B_1$ ( $\mu\text{T}$ )	13.5	13.5	13.5	13.5	23.0	23.0	23.0
Max frequency (Hz)	597	597	42.5E3	6.40E3	597	42.5E3	6.40E3
Duration (ms)	13.3	13.1	4.90	13.9	11.3	3.60	14.3
Phase step (rad)	-	-	1.63	-	-	1.64	-
$\boxtimes$	-	-	189	-	-	164	-

Table 1. Sequence parameters of the standard hyperbolic secant (HS), and HS,  $B_1$  insensitive rotation (BIR)-4, and frequency offset corrected inversion (FOCI) pulse optimized for two maximum  $B_1$  conditions.

## RESULTS

The traditionally implemented VSI-ASL label module shows reduced labeling efficiency at  $B_1$ -levels  $< -0.7$ , while there is only a very limited effect of  $B_0$ -inhomogeneity, see Figure 2. The traditionally implemented VSI-ASL control module is motion-compensated, this module shows severe sensitivity to both  $B_0$ - and  $B_1$ -inhomogeneity. In contrast, the motion-insensitive control module is robust to  $B_0$  inhomogeneity, and only shows reduced inversion efficiency for  $B_1$ -levels  $< -0.7$ .

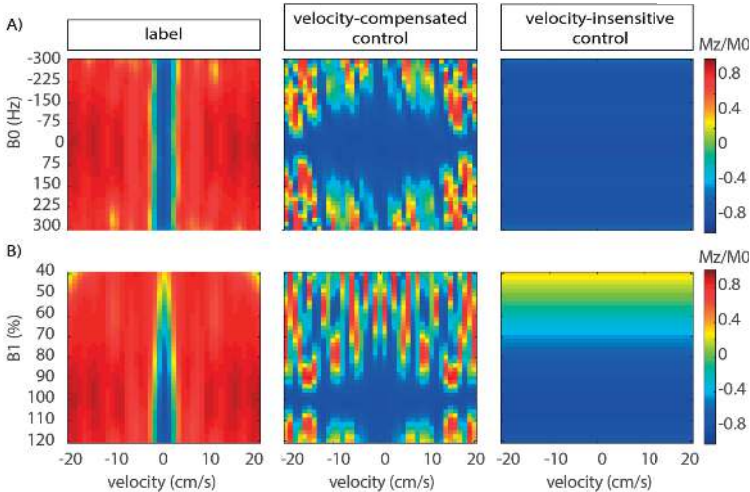


Figure 2. Effect of A)  $B_0$  and B)  $B_1$  inhomogeneity on the VSI labeling module, velocity-compensated module (traditionally used), and velocity-insensitive module. Reduced labeling efficiency due to  $B_1$ -sensitivity can lead to subtraction artefacts in poor  $B_1$  conditions, as was previously observed in kidneys[145].

Optimization of the BGS pulses, for the two maximum B<sub>1</sub> constraints, resulted in the sequence parameters shown in Table 1. Comparing the results for the two different B<sub>1</sub> constraints, it is clear that all optimized pulses use their maximum B<sub>1</sub>. Besides B<sub>1</sub>, the optimized settings for the two B<sub>1</sub>-constraints differ in their duration, while the other parameters stayed relatively constant. Note, that optimizing the HS pulse for B<sub>0</sub> and B<sub>1</sub> inhomogeneity expected in the abdomen, did not result in any significant changes to the pulse parameters at a maximum B<sub>1</sub> of 13.5 μT, compared to the standard settings. The resulting amplitude and frequency diagrams of the optimized sequence parameters for maximum B<sub>1</sub> of 13.5 μT are shown in Figure 3.

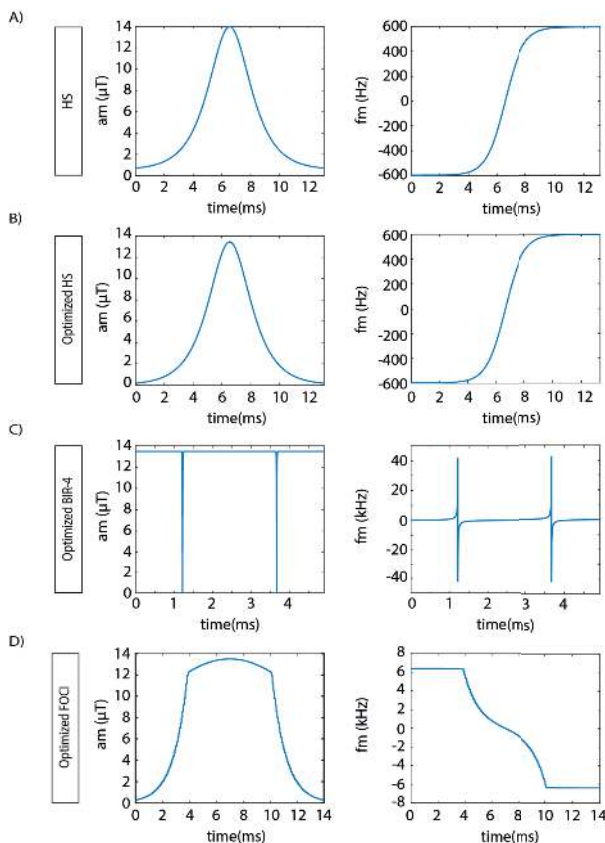


Figure 3. Pulse sequences of A) standard hyperbolic secant (HS), B) HS, C) B<sub>1</sub> insensitive rotation (BIR-4), and D) frequency offset corrected inversion (FOCI) pulse optimized with a maximum B<sub>1</sub> of 13.5 μT.

Comparing the four pulses at maximum B<sub>1</sub> of 13.5 μT, reveals that the optimized HS pulse overall shows the highest robustness to B<sub>0</sub> and B<sub>1</sub>, see Figure 4. For a maximum B<sub>1</sub> of 13.5 μT, there is no visible improvement in inversion efficiency of the optimized HS compared to the standard one, see Figure 3, as expected from Table 1. Only in cases where solely B<sub>1</sub>-

inhomogeneity plays a role, while the  $B_0$  homogeneity is near perfect, and the maximum available  $B_1$  is  $13.5 \mu\text{T}$ , BIR-4 could show a better inversion efficiency than HS, see Figure 4.

Having a maximum  $B_1$  of  $23 \mu\text{T}$ , instead  $13.5 \mu\text{T}$ , available improves inversion efficiency considerably, see Figure 5. Also in this condition, the optimized HS pulse shows the best performance.

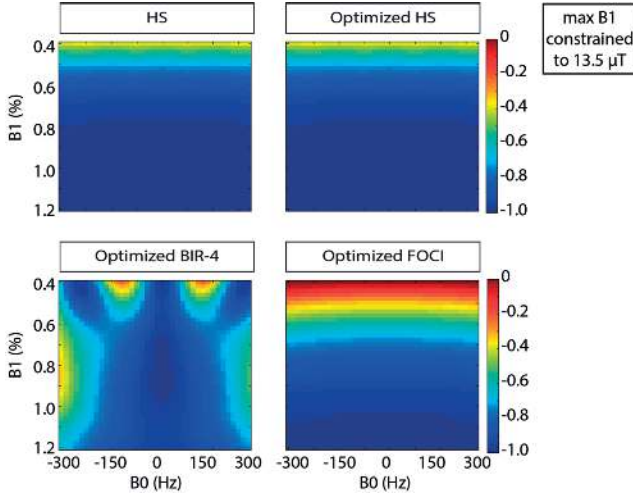


Figure 4. Inversion efficiency, for a range of  $B_0/B_1$ -levels corresponding to anatomies in the vicinity of the lungs, of the standard hyperbolic secant (HS) and HS,  $B_1$  insensitive rotation (BIR)-4, and frequency offset corrected inversion (FOCI) pulse. These pulses were optimized with a maximum  $B_1$  of  $13.5 \mu\text{T}$ . Pulses correspond to the pulse shapes shown in Figure 3.

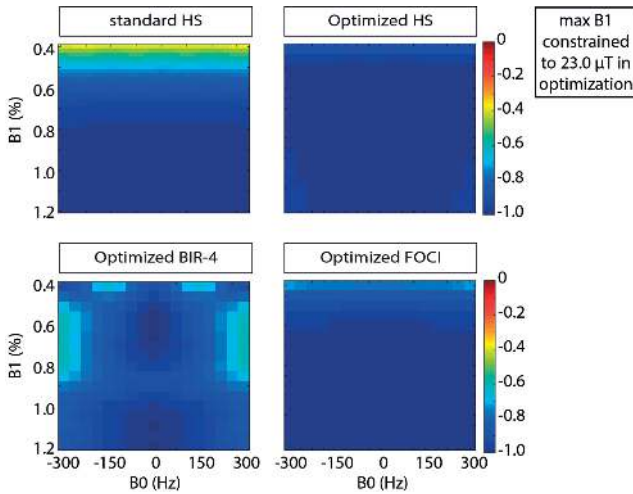


Figure 5. Inversion efficiency, for a range of  $B_0/B_1$ -levels corresponding to anatomies in the vicinity of the lungs, of the standard hyperbolic secant (HS) and HS,  $B_1$  insensitive rotation (BIR)-4, and frequency offset corrected inversion (FOCI) pulse. These pulses were optimized with a maximum  $B_1$  of  $23 \mu\text{T}$ .

## DISCUSSION

In this study  $B_0/B_1$ -simulations were performed to gain insight into which parts of the VSI-ASL sequence require further optimization, and to explore possible solutions, to eliminate subtraction errors in body applications, such as in kidneys. First of all, the  $B_0$  and  $B_1$  sensitivity of the VSI-ASL sequence was considered. Simulations show that there is a severe sensitivity to  $B_0$  and  $B_1$  inhomogeneity with the default implementation of the VSI-ASL sequence, especially due to the motion-compensated control. Secondly, simulations were performed to study the  $B_0$  and  $B_1$  sensitivity of various BGS pulses. The standardly used BGS pulse (HS) shows  $B_1$ -sensitivity, but no remarkable  $B_0$ -sensitivity. Optimized versions of the HS, BIR-4, and FOCI, do not show an overall improved performance when considering both  $B_0$  and  $B_1$ -field inhomogeneity at a maximum  $B_1$  of 13.5  $\mu\text{T}$ . The BIR-4 could provide an improved performance, only in cases where there is only  $B_1$ -inhomogeneity and where the maximum available  $B_1$  is 13.5  $\mu\text{T}$ . Allowing a maximum  $B_1$  of 23.0  $\mu\text{T}$ , and using optimized settings for HS would improve the inversion efficiency under  $B_1$ -inhomogeneity considerably.

These results confirm the previously found  $B_0$ - and  $B_1$  sensitivity of the motion-compensated VSI-control module described by Qin et al. [53]. In the current study, a broader range of  $B_0$  and  $B_1$  were employed, to simulate the field conditions in the abdomen. In these field conditions there is an even more severe disturbance of the inversion efficiency of the motion-compensated VSI-control module. In contrast, the motion-insensitive control module is robust to these field conditions. The motion-insensitive control module does introduce an imbalance in diffusion-weighting between the label and control module, potentially leading to an overestimation of the blood flow due to a diffusion-related signal contribution. Although, this effect was previously found to be negligible[122]. For abdomen, the tradeoff likely favors the motion-insensitive control with increased inversion efficiency, and consequently fewer subtraction artefacts, including a possible diffusion contribution, over the subtraction artefacts associated with motion-compensated VSI-control module. In a more recent study in the myocardium, a motion-insensitive control module was employed for these reasons[125]. This study further improved labeling efficiency by optimizing the amplitudes of the VSI-sub pulses, based on the expected off-resonance and  $B_1$  condition in the heart, as well as the intended velocity field of view[125]. A separate study has demonstrated a reduction in eddy currents and  $B_1$ -sensitivity by replacing the hard refocusing pulses in the VSI-module to composite pulses[189]. Optimizing the amplitudes and/or pulse shape of the VSI-sub pulses would, in addition to using a velocity-compensated control module, also for other body applications be an interesting approach to reduce the sensitivity for field inhomogeneity even further.

The BGS simulations show that there is no clear alternative to the HS pulse for applications in challenging  $B_0$ - and  $B_1$ -conditions, both in case of a maximum  $B_1$  of 13.5  $\mu\text{T}$  and of 23

$\mu\text{T}$ . BIR-4 only has a better inversion efficiency when solely the  $B_1$ -field is disturbed, without perturbation of  $B_0$  (at a maximum available  $B_1$  of  $13.5 \mu\text{T}$ ), which is not realistic for abdominal applications with the current  $B_0$ -shimming possibilities. Furthermore, results have shown that the inversion efficiency improves drastically when a higher  $B_1$  ( $23.0 \mu\text{T}$ ) is available, as is the case in ref[57], or can be achieved by using local transmit coils. In those cases, an optimized implementation of the HS-pulse has the best performance.

To reduce the effect of field inhomogeneity on the ASL-measurements, going to a lower field strength could also be considered. Magnetic susceptibility effects halve at  $1.5\text{T}$ [61]. In addition, the  $B_1$ -field is also more homogenous[61]. For example, a  $B_0$  of  $\pm 80 \text{ Hz}$  and  $B_1$ -levels of  $0.8\text{-}1.1$  have been measured in liver at  $1.5\text{T}$ [190]. However, future studies could indicate whether the improvement in field conditions at  $1.5\text{T}$  outweigh the expected reduction in SNR[61] and shortening in  $T_1$ [61], and how the performance compares to spatially-selective techniques, such as flow-sensitive alternating inversion recovery (FAIR)[148], at  $3\text{T}$ .

This study also has some important limitations. First, the study only consisted of simulations. In-vivo studies, showing the performance of the different VSI-ASL modules and BGS pulses in-vivo would be very valuable and would enable inspection of the ASL subtraction artefacts. Second, this study only considered the field conditions at  $3\text{T}$ . In-vivo studies comparing  $1.5\text{T}$  and  $3.0\text{T}$  could provide more insight in what the optimal setting would be for abdominal VSI-ASL. Third, only a limited number of inversion pulses have been considered for BGS in this study. Multiple other adiabatic inversion pulses exist and should be considered, although differences in performance were mostly shown to be subtle[191]. Lastly, this study solely performed simulations for the traditional VSI-ASL sequence. Previously, specific optimizations for myocardium of the amplitudes of the hard pulses that make up the VSI-ASL pulse train, have shown promising results[125]. The concept of optimizing the VSI-ASL pulse train for specific organs should be considered for other body applications.

In conclusion, this study has shown that there is a  $B_0$ - and  $B_1$ -sensitivity of both the VSI-module and the BGS pulses for VSI-ASL. Several improvements of the VSI-sequence should be considered in future body applications of VSI-ASL, to prevent subtraction errors as demonstrated in ref[145]. For example, our simulations have shown that using a velocity-insensitive instead of a velocity-compensated control module will increase labeling efficiency considerably. Furthermore, optimization of the VSI sub-pulse amplitudes under the expected field conditions, and/or usage of composite refocusing pulses could potentially make VSI-ASL labeling efficiency less dependent on field homogeneity, and thus further improve robustness. In terms of BGS pulses, no superior alternative to HS pulses were found. In vivo studies investigating the effect of these recommended adjustments to the VSI-sequence, and possibly investigating other alternatives to BGS-pulses, at  $1.5\text{T}$  and  $3.0\text{T}$  are warranted.





# Chapter 7

---

**Summary and general discussion**

---





This thesis presents research done on the translation of MRI perfusion techniques from brain to body applications. In the section below the main findings and implications are summarized and discussed, followed by key points that need to be addressed in future work to take the next steps in body ASL.

Flow-based ASL forms a promising set of techniques for body applications due to their inherent properties of labeling non-spatially selective (i.e. no labeling slab needs to be planned), and transit time insensitivity, enabling application in organs with multiple feeding vessels and/or slow flow. First, a more general property, which is not limited to body applications, was studied in brain, where the technique is already more established. **Chapter 2** describes the work done on measurement of the cardiac cycle sensitivity of a single VS-ASL and Acc-ASL module. The sequence was designed in such a way to minimize other contributions to the signal, that are influenced by the cardiac cycle, i.e.: inflow of 'fresh' unlabeled spins, the distance that the label travels into the vasculature, and venous signal. Results showed that the amount of arterial label generated by a single VS-ASL and Acc-ASL module differed by ~36% and 64%, respectively, over the cardiac cycle. However, because in ASL, multiple repetitions are acquired, this effect is expected to average out and not have a major effect on the resulting perfusion measurement. On the other hand, these results provide an interesting starting point to develop a measure for microvascular pulsatility, by mapping variation of the generated ASL-signal over the cardiac cycle, i.e. highly pulsatile blood flow will lead to high variation, and low pulsatility will lead to low variation over the cardiac cycle. Scan time, however, would need to be shortened dramatically to make it clinically feasible.

In **Chapter 3**, different flow-based ASL techniques (VS-ASL, Acc-ASL, mm-VSASL, and VSI-ASL) were compared to spatially-selective ASL techniques in brain (pCASL) and kidney (pCASL and FAIR). In brain, volunteers were presented with a visual task to induce a perfusion increase in the visual cortex, which was used to validate the measurements. Results showed that VSI-ASL had a similar sensitivity as pCASL for picking up this perfusion increase, while the other flow-based techniques showed less sensitivity. In kidney, FAIR had a higher temporal SNR (tSNR) than all other techniques. All flow-based ASL-techniques showed a similar tSNR. For VSI-ASL, severe subtraction artefacts were observed in areas with low  $B_1$ , which were likely related to a combination of reduced inversion efficiency of the background suppression pulses as well as VSI-ASL labeling efficiency. From the results in the brain it is clear that VSI-ASL has the highest potential as flow-based technique, but only when used in relatively homogenous magnetic field conditions. However, for body applications, it is vital that adjustments are made so that VSI-ASL becomes more robust to field imperfections. Because of the issues regarding field imperfections, VS-ASL, instead of VSI-ASL, was used in a following study in breast cancer patients.

Feasibility of VS-ASL in breast cancer patients is described in **Chapter 4**. Overall, lesions were well visible with VS-ASL, and artifacts could be distinguished from the ASL-signal. Importantly, by using a flow-based ASL technique, the whole breast could be covered, while this is not feasible when using spatial-selective ASL techniques as FAIR. A comparable morphology was seen for the signal observed with VS-ASL as for the early phases of the ultrafast DCE scan. This confirms that VS-ASL is a measure for perfusion and vascularity, similar as the early phases of ultrafast DCE. In addition, an unexpected observation was made concerning segmental patterns of increased perfusion around some lesions, which corresponded to areas including prominent vessels, which seemed to form either feeding or draining vessels of the lesion. In patients with dense breast, VS-ASL exhibited stronger artifacts, due to the high contrast between glandular and fat tissue on the raw images, leading to subtraction artefacts when even minor motion was present. This first attempt at applying VS-ASL in breast cancer patients showed promising results for the development of a non-contrast alternative for perfusion imaging for breast cancer. Therefore, VS-ASL holds the potential to have a major impact on breast cancer screening, since it could limit the use of gadolinium-based contrast agents. Such an approach would be in line with the current attempts to employ a multi-parametric breast protocol to improve diagnostic accuracy, in which several non-contrast enhanced scans are added to the traditional breast exam. This allows integration of different and complementary information contained in these images. Until now there was no non-contrast alternative to DCE-MRI, that is sensitive to blood flow and perfusion. By replacing DCE-MRI by VS-ASL, all scans would be non-contrast enhanced: reducing costs and patient discomfort considerably. Now we have established the feasibility of VS-ASL in breast cancer patients, the repeatability and sensitivity of the method should be investigated in larger patient groups, especially for smaller lesions. To improve SNR it would be interesting to use VSI-ASL, although then, either the field imperfections in breast or the sensitivity of VSI-ASL to  $B_0/B_1$  inhomogeneity would likely need to be reduced. In addition, it would be desirable to reduce the occurrence of subtraction artifacts, which were especially observed in patients with dense breast. A possible approach would be to optimize background suppression to, in addition to fat signal, also minimize glandular tissue signal.

In both the kidney as well as the breast study, EPI was used as readout technique, because of its time efficiency and thus motion insensitivity. However, EPI is also known for its sensitivity to off-resonance effects in the phase-encoding direction, leading to signal loss and image distortions. In both the kidney as well as breast study, artefacts were observed as a result of this off-resonance sensitivity. In kidneys, distortions, i.e. elongation of the kidneys were observed with EPI-readouts. Elongation of the kidneys was relatively stable, thereby not producing noticeable subtraction artifacts. However, occasional signal voids around the colon due to pockets of air, obscured parts of the kidneys in some volunteers. In breast, EPI-induced distortions due to the filling and emptying of the lungs during the respiratory cycle were observed. These distortions

were dealt with by performing a non-rigid motion correction. However, even when performing non-rigid motion correction, there is always the chance of residual registration errors, leading to subtraction artifacts in the resulting ASL-image. An additional source of subtraction artifacts were fat signal ghosts, which still occurred even though an image-based shimming tool, dedicated to breast MRI, SPAIR fat suppression and background suppression were used. Although in most cases the subtraction artifacts could be easily distinguished from ASL-signal, it would be desirable to have a readout method that is less sensitive to off-resonance.

These  $B_0$ -related problems for body ASL are addressed in **Chapter 5**. Here an alternative readout to EPI was implemented that is more robust to  $B_0$  field inhomogeneity and susceptibility-induced  $T_2^*$  dephasing, i.e. spatio-temporal encoding (SPEN). The feasibility of combining SPEN with ASL was demonstrated for brain perfusion imaging, confirming the higher robustness of SPEN to susceptibility-induced artifacts compared to spin echo (SE)-EPI and gradient echo (GE)-EPI, without a cost in SNR. A TR-dependence was observed for ASL-images with SPEN readout: a minimal delay of  $\sim 1000$  ms is advised between the SPEN-excitation pulse and start of the next labeling module, to prevent SNR loss. The TR-dependence is likely caused by the chirp pulse as used in SPEN, which affects all spins within reach of the transmit coil. The chirp pulse will have a saturation effect on the hydrogen nuclei in blood proximal to the labeling plane, reducing the labeling efficiency of pCASL of the following repetition. This study did have some limitations: it was performed with a single-slice readout, and used relatively large voxels for the SPEN-images.  $T_2$ -decay during readout prevented a smaller voxel size. Improvements to the sequence are necessary to enable multi-slice/3D-scanning and allow improved resolution in combination with larger FOVs, such as parallel imaging approaches.

In **Chapter 6**, we studied the  $B_0/B_1$ -sensitivity of VSI-ASL that lead to significant artefacts as observed in Chapter 3, especially focusing on the hyperbolic secant background suppression pulses and the VSI-ASL labeling module. Simulations using the Bloch equations were performed for field conditions that can be expected at 3T in anatomies close to the lungs, such as kidneys and breast ( $B_1$ -level = [0.4, 1.2], and  $B_0 = \pm 300$  Hz[127], [128], [190]). Simulations of the VSI-ASL label- and control modules showed that there is a severe reduction in labeling efficiency for the expected  $B_0$  and  $B_1$ -levels, when using a velocity-compensated control module. They furthermore show that velocity-insensitive control modules are more robust to  $B_0$  and  $B_1$  inhomogeneity and thereby provide a good alternative. Simulations of the inversion efficiency of background suppression pulses were performed for hyperbolic secant (standard), BIR-4, and FOCI, at two different  $B_1$ -levels. Results showed that BIR-4 pulses can provide a higher robustness in terms of  $B_1$ , but only in areas where there is almost no frequency offset. For both  $B_1$ -levels hyperbolic secant provided the best inversion efficiency when both  $B_0$  and  $B_1$ -imperfections are present. Therefore, it was concluded that the hyperbolic secant pulse still provides the best compromise for background suppression for ASL in body applications.

In conclusion, the studies of this thesis demonstrated great potential for flow-based ASL for body applications in general, and breast and kidney specifically. Considering the next steps, there are two main technical domains where improvements are warranted to improve performance of flow-based ASL in body applications:

- 1) Improvements need to be made to the labeling method; to get a  $B_0/B_1$ -robust flow-based ASL method that matches the SNR of the standard spatially-selective technique, e.g. pCASL and/or FAIR.
- 2) Improvements need to be made to the readout technique, to make it more  $B_0/B_1$ -robust than EPI without a cost in SNR, resolution, or affecting labeling efficiency of the next measurement.

These technical topics, as well as the next steps for flow-based ASL in clinical studies, will be discussed in more detail below.

#### Future outlook: Improving $B_0/B_1$ -sensitivity of VSI-ASL

This work has shown that ASL, and in particular flow-based ASL is feasible in kidney and breast applications. It has also unveiled prevailing issues that prevent the widespread use of flow-based ASL in the body at the moment and especially at 3 Tesla. VSI-ASL is the most promising flow-based ASL technique in brain, showing a similar sensitivity as pCASL to pick up on regional perfusion increases, as demonstrated in chapter 2. However, when applied in kidneys, as described in chapter 2 and 5,  $B_1$ -sensitivity of the VSI-labeling sequence compromised labeling efficiency as well as decreased inversion efficiency of background suppression pulses. This is likely also an issue for other anatomies associated with reduced  $B_1$ , i.e. organs in proximity to the lungs, such as breast. By using a VS-ASL technique based on saturation, promising results were obtained in breast cancer patients, as reported in chapter 4. However, to be able to also visualize smaller, and more early-stage lesions, as well as make a clearer distinction between ASL-signal and subtraction artifacts, it is necessary to improve the SNR of the labeling technique. VSI-ASL has the potential to provide such increased perfusion sensitivity, if the  $B_0/B_1$ -robustness can be improved for these body applications. Because currently, VSI-ASL still has a higher sensitivity to field imperfections than VS-ASL[192].

The VSI-ASL sequence used in this work already included MLEV phase-cycling of the refocusing pulses inside each VSI-module to improve  $B_0/B_1$ -robustness[122]. Recently, dynamic phase-cycling of the refocusing pulses was introduced to further improve the field robustness[193]. Here, VSI-ASL is used with an additional 90-degree phase-increment to the refocusing pulses for every dynamic. In addition, a velocity-insensitive control module is employed, which, as also shown in chapter 5, enhances the robustness to  $B_0$  and  $B_1$ -inhomogeneity considerably [53]. This results in  $B_0/B_1$ -robustness for field conditions typical for brain at 3T, i.e.  $B_0$  of

$\pm 300$  Hz and  $B_1$ -level of  $1.0 \pm 0.2$ . It is yet unclear how this technique would perform in more challenging anatomies in terms of field inhomogeneity, as well as movement. Dynamic phase-cycling relies on averaging of the four dynamics to average out signal from static spins and the so-called stripe artifact[193], which is likely not compatible with organ movement as encountered in e.g. kidney ASL.

An alternative adaptation of the VSI-ASL sequence, i.e. “sinc-VSI-ASL”, was presented for measuring perfusion in myocardium[125]. Here, the amplitude of the VSI-ASL sub-pulses were optimized based on the expected  $B_0/B_1$ -range and motion in the myocardium, to improve labeling efficiency and prevent spurious labeling of myocardial tissue[125]. Here the amplitude of the VSI-ASL sub-pulses followed a windowed sinc-modulation, instead of the more traditional rectangular shape. This resulted in a more rectangular  $M_z$ -velocity profile (instead of a sinc-profile), providing sharper edges of the velocity field-of-view. In addition, a velocity-insensitive control module was used. The superior  $B_0/B_1$ -robustness of this sinc-modulated VSI-ASL method with velocity-insensitive control was confirmed in a later study [192], although it still has a higher sensitivity to field imperfections compared to the saturation-based BIR-8 VS-ASL approach[192].

Although a separate optimization per anatomy might be undesirable, due to the added complexity, labeling efficiency could in a similar manner be improved for other organs by optimizing for the specific motion and field conditions[125]. Myocardium has stringent constraints on the stopband due to the amount of motion, but this is less of an issue in e.g. breast, potentially allowing a higher labeling efficiency. This would be an interesting area to pursue in future studies.

## **FUTURE OUTLOOK: IMPROVING $B_0$ -SENSITIVITY OF THE READOUT**

In this work we have demonstrated the feasibility of combining SPEN with ASL in brain, enabling a higher robustness to susceptibility-induced artifacts. This thesis furthermore discussed off-resonance related artifacts and distortions for kidneys as well as breast. A logical next step would be to investigate SPEN-ASL in abdomen applications. Alterations to the SPEN implementation, used in this thesis, have been proposed to enable multi-slice[164]: 3D scanning[178], and improve spatial resolution. Multi-slice scanning is enabled by the use of an additional pulse after excitation that returns all spins outside of the slice back to equilibrium. This has the added benefit that, when combined with ASL, the saturation effect of the chirp pulse on incoming unlabeled blood, as shown in chapter 5, will likely be minimal in the smaller arteries. However, imperfections will exist in the reinversion of the spins in the larger

arteries, where flow is higher. Using these state-of-the-art SPEN-implementations for ASL body applications is an interesting approach which could potentially form a solution for the off-resonance and distortion artifacts discussed in this thesis.

Besides SPEN and multi-slice 2D EPI, various 3D readouts have been developed specifically for ASL body applications, to deal with the challenges of movement and field inhomogeneity. Compared to EPI and GRASE, 3D fast spin echo (FSE) is inherently more robust to susceptibility artifacts[194], making it an interesting candidate for body applications. To limit its scan time, 3D FSE has been combined with compressed sensing in renal ASL[176]. In another approach, 3D segmented FSE was combined with a Cartesian acquisition and spiral profile reordering to improve robustness[177]. Further research is needed to compare these readout approaches with SPEN for ASL measurements in body.

## FUTURE OUTLOOK: CLINICAL STUDIES

This work has shown feasibility of flow-based ASL in body, mostly on healthy volunteers, with the exception of the study in breast cancer patients. Before these techniques can be used in a clinical setting, a comparison of spatially selective and flow-based ASL techniques is needed in specific patient groups. Alterations in flow conditions can occur depending on the pathology and organ, e.g. increased transit times in case of a stenosis.

In addition, it is essential to have acceptable repeatability and reliability for a specific application, measured in larger patient cohorts, before the technique can have a widespread clinical use. Repeatability can be measured, e.g. by performing repeated measures on different days. Reliability is more complicated to measure because of a lack of a golden standard perfusion technique [18] to compare ASL to. Care should be taken when validating the ASL against DCE-MRI, because these techniques do not measure exactly the same phenomena. ASL is a pure perfusion technique, while the signal of DCE-MRI is a mixture of perfusion and vessel wall permeability. Because vessel wall permeability is an effect that mainly comes into play at later phases after contrast injection, ASL signal can be compared to the flow-dominated early-phases of ultrafast DCE-MRI, as was done in chapter 4. In a recent study, ASL, as measured by FAIR, was shown to be the most repeatable perfusion method in kidney [195].

To further develop flow-based ASL in specific patient groups, it would be helpful when vendors would provide research institutes with ‘works-in-progress’ versions, so that these new approaches can easily be tested in clinical patients. Harmonization of such sequences among vendors would also be needed, similar as what has been achieved with pCASL for brain applications[13].

In summary, this thesis provides a major step in the application of flow-based ASL in body applications, and describes challenges that need to be overcome before widespread clinical use is possible.





# Chapter 8

---

**Dutch summary**

---



Stroming-gebaseerde ASL vormt een veelbelovende groep technieken die ook uitermate geschikt is voor toepassingen buiten het brein vanwege de inherente eigenschappen dat ze niet spatieel-selectief labelen (d.w.z. er hoeft geen labeling plak te worden gepland), en dat ze ongevoelig zijn voor de arteriële transitie tijd (ATT), wat toepassing in organen met verschillende toevoerende vaten en/of langzame bloedstroom mogelijk maakt.

Allereerst is een meer algemeen kenmerk bestudeerd in het brein, waar de techniek al verder ontwikkeld is. **Hoofdstuk 2** beschrijft het onderzoek naar het meten van de hartslaggevoeligheid van een enkele snelheid-selectieve arteriële spin labeling (VS-ASL) en versnelling-selectieve arteriële spin labeling (Acc-ASL) module. De sequentie is specifiek ontworpen zodat andere contributies aan het signaal, die ook beïnvloed worden door de hartslag, geminimaliseerd zijn, d.w.z.: de instroom van 'verse' ongelabelde spins, de afstand dat het label stroomt in het vasculaire netwerk, en het veneuze signaal. Resultaten hebben aangetoond dat de hoeveelheid arterieel label dat gegenereerd wordt door een enkele VS-AL en Acc-ASL module met respectievelijk ~36% en ~64% varieert over de hartcyclus. Echter, omdat in ASL altijd wordt gemiddeld over verschillende herhalingen van de meting, wordt er verwacht dat dit effect zich uitmiddelt en dat het geen grote effecten heeft op de resulterende perfusie meting. Aan de andere kant geven deze resultaten een interessant uitgangspunt voor het ontwikkelen van een techniek om de pulsatiliteit van de microvasculatuur te meten. Het kan de variatie van het gegenereerde ASL-signaal over de hartslag in kaart brengen, d.w.z. hoog pulsatiele bloed stroom leidt tot hoge variatie, en laag pulsatiele bloedstroom tot lage variatie over de hartcyclus. Voordat de techniek klinisch haalbaar wordt, moet de scantijd echter drastisch omlaag gebracht worden.

In **hoofdstuk 3** zijn verschillende stroming-gebaseerde ASL technieken (VS-ASL, Acc-ASL, VS-ASL met meerdere VSASL modules (mm-VSASL) en snelheid-selectieve ASL gebaseerd op inversie (VSI-ASL)) vergeleken met spatieel-selectieve ASL technieken, in het brein (pseudo continue ASL (pCASL)), en in de nieren (pCASL en bloedstroom alternerende inversie herstel (FAIR)). Bij de scans in het brein zijn vrijwilligers gepresenteerd met een visuele taak, wat een perfusieverhoging induceert in de visuele cortex, om de resultaten te valideren. Het onderzoek heeft aangetoond dat VSI-ASL een vergelijkbare gevoeligheid heeft als pCASL voor het oppikken van deze perfusieverhoging, terwijl de andere bloedstroom-gebaseerde technieken minder sensitief zijn. In de nieren had FAIR een hogere temporele signaal-ruis verhouding (tSNR) dan de andere technieken. Alle stroming-gebaseerde ASL technieken lieten een vergelijkbare tSNR zien. Ernstige subtractieartefacten waren zichtbaar in gebieden met lage  $B_1$  voor VSI-ASL. Deze waren waarschijnlijk gerelateerd aan een combinatie van verminderde inversie efficiëntie van de achtergrondpulsen en de VSI-ASL labelingefficiëntie. De resultaten in het brein laten duidelijk zien dat VSI-ASL de meeste potentie heeft als bloedstroom-gebaseerde techniek, maar alleen in het geval van een relatief homogeen magnetisch veld. Voor toepassingen in de rest van het lichaam is het van essentieel belang dat VSI-ASL meer robuust wordt voor veldimperfecties.

Door deze bevindingen rondom veldimperfecties, is er voor gekozen om VS-ASL te gebruiken in plaats van VSI-ASL in de opeenvolgende studie in borstkanker patiënten.

De studie naar de haalbaarheid van VS-ASL in borstkanker patiënten is beschreven in **hoofdstuk 4**. De resultaten hebben laten zien dat, over het algemeen, laesies goed zichtbaar waren met VS-ASL en dat artefacten konden worden onderscheiden van het ASL-sigitaal. Belangrijk om te noemen is dat door het gebruik van een stroming-gebaseerde ASL techniek de hele borst kon worden afgebeeld, terwijl dit niet haalbaar is voor een spatieel-selectieve ASL techniek, zoals FAIR. Bovendien hebben de resultaten laten zien dat er een vergelijkbare morfologie zichtbaar was voor het signaal geobserveerd met VS-ASL als voor de eerste fases van de ultrasnelle dynamische contrast versterkte (DCE) scan. Dit bevestigd dat VS-ASL een maat is voor perfusie en vasculariteit, vergelijkbaar met de eerste fases van de ultrasnelle DCE scan. Daarnaast is er een onverwachte observatie gemaakt omtrent segmentale patronen van verhoogde perfusie rondom een aantal laesies, die overeenkomen met gebieden waar prominente vaten doorheen lopen, wat voedende of afvoerende vaten leken van de laesie. VS-ASL vertoonde sterkere artefacten in patiënten met dicht borstweefsel door het hoge contrast tussen klier- en vet weefsel op de ruwe beelden, wat zelfs met een kleine hoeveelheid beweging tot subtractie-artefacten leidt. Deze eerste poging tot het toepassen van VS-ASL in borstkanker patiënten heeft veelbelovende resultaten laten zien voor de ontwikkeling van een contrastmiddel-vrij alternatief voor de beeldvorming van perfusie voor borstkanker. VS-ASL heeft de potentie om een enorme impact te maken op borstkanker screening, aangezien VS-ASL het gebruik van gadolinium-gebaseerde-contrastmiddelen potentieel zou kunnen limiteren. Deze aanpak zou in lijn zijn met het huidige pogingen om een multi-parametrisch borstprotocol in te zetten om diagnostieke accuraatheid te verbeteren. Daarbij worden meerdere contrastmiddel-vrije scans toegevoegd aan het traditionele borst examen. Dit maakt de integratie van verschillende en complementaire informatie uit deze beelden mogelijk. Tot nu toe was er geen contrastmiddel-vrij alternatief voor DCE-MRI, dat sensitief is voor perfusie en vasculariteit. Het vervangen van DCE-MRI door VS-ASL, zou alle scans contrastmiddel-vrij maken: wat de kosten en het ongemak van patiënten zou verminderen. Nu we de haalbaarheid van VS-ASL in borstkanker patiënten hebben aangetoond, zou de herhaalbaarheid en sensitiviteit van de methode moeten worden onderzocht in grotere patiëntgroepen, vooral voor kleinere laesies. Ook zou het interessant zijn om VSI-ASL te gebruiken om de SNR te verbeteren. Echter, is het dan van belang om ofwel de veldimperfecties in de borst te reduceren ofwel de sensitiviteit van VSI-ASL voor  $B_0/B_1$  inhomogeniteit te verminderen. Daarnaast zou het wenselijk zijn de hoeveelheid subtractie-artefacten te verminderen, die met name zijn geobserveerd in patiënten met dicht borstweefsel. Een mogelijke aanpak zou zijn om de achtergrondsuppressie te optimaliseren, zodat het naast het signaal van vet- ook klierweefsel minimaliseert.

In zowel de nieren als de borststudie is EPI gebruikt als acquisitietechniek, voornamelijk om de tijdsefficiëntie en zodoende robuustheid voor beweging. Echter, EPI is ook bekend om de sensitiviteit voor buiten-resonantie effecten in de fase-encoding richting, wat leidt tot signaalverlies en beeldverstoring. In zowel de nieren als de borststudie, zijn artefacten geobserveerd als het resultaat van deze buiten-resonantie effecten. In nieren, zijn vervormingen, d.w.z. verlenging van de nieren geobserveerd met een EPI acquisitie. De verlenging van de nieren was relatief stabiel, waardoor het geen merkbare subtractie-artefacten produceert. Echter, in sommige vrijwilligers was er signaalverlies rondom de darmen door lucht, waardoor ook signaal in sommige delen van de nieren is weggevalen. In de borst zijn EPI-geïnduceerde vervormingen geobserveerd die veroorzaakt worden door het vullen en legen van de longen tijdens de ademhalingscyclus. Om hier mee om te gaan wordt niet-rigide bewegingscorrectie toegepast. Echter is het gebruik van niet-rigide bewegingscorrectie geassocieerd met een kans op residuele registratie fouten in het ASL beeld. Een andere bron van subtractiefouten waren de herhalingen, of 'ghosts', van het vetsignaal, die voorkwamen ondanks het gebruik van een beeld-gebaseerde shimming methode die specifiek is ontwikkeld voor borst MRI, spectrale geattenuerde inversie herstel (SPAIR) vetsuppressie en achtergrondsuppressie.

Deze  $B_0$ -gerelateerde uitdagingen van ASL bij toepassingen buiten het brein zijn aangesproken in **hoofdstuk 5**. In dit onderzoek is een alternatieve acquisitietechniek geïmplementeerd dat meer robuust is voor  $B_0$ -veld inhomogeniteiten en susceptibiliteit-geïnduceerde  $T_2^*$  defasering, d.w.z. spatio-temporele encoding (SPEN). De haalbaarheid van het combineren van SPEN met ASL is gedemonstreerd voor perfusie beeldvorming in het brein. Dit bevestigt de hogere robuustheid van SPEN voor susceptibiliteit-geïnduceerde artefacten, vergeleken met een spin-echo echo-planaire-beeldvorming (SE-EPI) en gradient echo (GE-)EPI, zonder in te leveren op SNR. Een repetitie tijd (TR) afhankelijkheid was geobserveerd voor de ASL-beelden met SPEN acquisitie; een minimale tijd van  $\sim 1000$ ms wordt geadviseerd tussen de SPEN-excitatie puls en de start van de volgende labeling module, om SNR verlies te voorkomen. De TR-afhankelijkheid is waarschijnlijk veroorzaakt door de chirp-pulse (d.w.z. met lineaire frequentie opbouw) zoals gebruikt in SPEN. Deze heeft invloed op alle spins die in het bereik van de verzendende spoel liggen. De chirp-puls zal een saturatie-effect hebben op de waterstof nuclei in het bloed proximaal aan het labelingvlak, wat de labelingefficiëntie van pCASL vermindert bij de opeenvolgende repetitie. Deze studie heeft een aantal limitaties: het is uitgevoerd met een enkele-plak acquisitie en gebruikte relatief grote voxels voor de SPEN-beelden.  $T_2$ -verval tijdens de acquisitie heeft het gebruik van grotere voxels onhaalbaar gemaakt. Verbeteringen aan de sequentie zijn nodig om multi-plak/3D-scannen en een verbeterde resolutie in combinatie met een groter gezichtsveld (FOV), mogelijk te maken, zoals bijvoorbeeld parallelle beeldvormingstechnieken.

In **hoofdstuk 6** hebben we de  $B_0/B_1$ -sensitiviteit van VSI-ASL, wat kan leiden tot significante artefacten zoals geobserveerd in hoofdstuk 3, bestudeerd. Daarbij is specifiek ingezoomd op de hyperbolische secant achtergrondpuls en de VSI-ASL labelingmodule. Simulaties, die gebaseerd zijn op de Bloch-vergelijkingen, zijn uitgevoerd voor de veldcondities zoals die verwacht kunnen worden bij 3T in anatomieën dicht bij de longen, zoals de nieren en borst ( $B_1$ -niveau = [0.4, 1.2], en  $B_0 = \pm 300$  Hz[127], [128], [190]). Simulaties van de VSI-ASL label- en control modules laten zien dat er een sterke vermindering is van de labelingefficiëntie voor de verwachte  $B_0$ - en  $B_1$ -niveaus wanneer er gebruik gemaakt wordt van een snelheid-gecompenseerde controlmodule. Ze laten verder zien dat snelheid-insensitieve controlmodules meer robuust zijn voor  $B_0$ - en  $B_1$ -inhomogeniteiten en daarmee een goed alternatief vormen. Simulaties van de inversie-efficiëntie van de achtergrondpuls zijn uitgevoerd voor de hyperbolische secant (standaard),  $B_1$ -insensitieve rotatie (BIR)-4, en frequentie afwijking gecorrigeerde inversie (FOCI) pulsen, op twee verschillende  $B_1$ -niveaus. Resultaten hebben laten zien dat BIR-4 pulsen een hogere robuustheid kunnen vormen in termen van  $B_1$ , maar alleen in gebieden waar er bijna geen afwijkende frequentie is. Voor beide  $B_1$ -niveaus heeft de hyperbolische secant puls de beste inversie-efficiëntie wanneer zowel  $B_0$ - als  $B_1$ -imperfecties aanwezig zijn. Daarom is geconcludeerd dat de hyperbolische secant puls nog steeds het beste optie is als achtergrondsuppressiepuls voor ASL bij toepassingen buiten het brein.

In conclusie, de studies van deze thesis hebben de grote potentie voor stroming-gebaseerde ASL voor toepassingen buiten het brein in het algemeen gedemonstreerd, en specifiek voor de nieren en de borst. Veranderingen zijn nodig op twee technische domeinen om de prestatie van stroming-gebaseerde ASL bij toepassingen buiten het brein te verbeteren:

1. Verbeteringen aan de labelingmethode: om een  $B_0/B_1$ -robuuste stroming-gebaseerde ASL-methode te realiseren dat de SNR van standaard spatieel-selectieve technieken, zoals bijvoorbeeld pCASL en/of FAIR, kan evenaren.
2. Verbeteringen aan de acquisitietechniek, om het meer  $B_0/B_1$ -robuust te maken dan EPI, zonder dat het een negatief effect geeft op SNR, resolutie, of de labelingefficiëntie van de opeenvolgende meting.







# Chapter 9

---

## References

---



- [1] A. J. Pappano and W. Gil Wier, "The Microcirculation and Lymphatics," in *Cardiovascular Physiology*, Elsevier, 2013, pp. 153–170.
- [2] V. Paruchuri *et al.*, "Aortic Size Distribution in the General Population: Explaining the Size Paradox in Aortic Dissection," *Cardiology*, vol. 131, no. 4, pp. 265–272, Jul. 2015.
- [3] "Clinical Perfusion MRI: Techniques and Applications - Google Books." [Online]. Available: [https://books.google.nl/books?id=Kbg0elHMDh4C&printsec=frontcover&source=gbs\\_ge\\_summary\\_r&cad=0#v=onepage&q&f=false](https://books.google.nl/books?id=Kbg0elHMDh4C&printsec=frontcover&source=gbs_ge_summary_r&cad=0#v=onepage&q&f=false). [Accessed: 05-Mar-2021].
- [4] D. Hanahan and R. A. Weinberg, "Hallmarks of cancer: The next generation," *Cell*, vol. 144, no. 5, Cell, pp. 646–674, 04-Mar-2011.
- [5] P. Singh, S.-E. Ricksten, G. Bragadottir, B. Redfors, and L. Nordquist, "Renal oxygenation and haemodynamics in acute kidney injury and chronic kidney disease," *Clin. Exp. Pharmacol. Physiol.*, vol. 40, no. 2, pp. 138–147, Feb. 2013.
- [6] M. Wintermark *et al.*, "Comparative overview of brain perfusion imaging techniques.," *Stroke*, vol. 36, no. 9, pp. e83-99, Sep. 2005.
- [7] P. Sminia *et al.*, "NCS Report 26: Human exposure to ionising radiation for clinical and research purposes: radiation dose and risk estimates," Aug. 2020.
- [8] J. Hendrikse, E. T. Petersen, and X. Golay, "Vascular Disorders: Insights from Arterial Spin Labeling," *Neuroimaging Clinics of North America*, vol. 22, no. 2, Neuroimaging Clin N Am, pp. 259–269, May-2012.
- [9] J. Naqvi, K. H. Yap, G. Ahmad, and J. Ghosh, "Transcranial Doppler ultrasound: A review of the physical principles and major applications in critical care," *International Journal of Vascular Medicine*, vol. 2013, Int J Vasc Med, 2013.
- [10] J. Lohrke *et al.*, "25 Years of Contrast-Enhanced MRI: Developments, Current Challenges and Future Perspectives," *Adv. Ther.*, vol. 33, pp. 1–28, 2016.
- [11] R. Erlemann *et al.*, "Musculoskeletal neoplasms: static and dynamic Gd-DTPA-enhanced MR imaging," *Radiology*, vol. 171, no. 3, pp. 767–773, 1989.
- [12] B. R. Rosen, J. W. Belliveau, J. M. Vevea, and T. J. Brady, "Perfusion imaging with NMR contrast agents," *Magn. Reson. Med.*, vol. 14, no. 2, pp. 249–265, 1990.
- [13] D. C. Alsop *et al.*, "Recommended implementation of arterial spin-labeled perfusion MRI for clinical applications: A consensus of the ISMRM perfusion study group and the European consortium for ASL in dementia," *Magn. Reson. Med.*, vol. 73, no. 1, pp. 102–116, Jan. 2015.
- [14] N. A. Telischak, J. A. Detre, and G. Zaharchuk, "Arterial spin labeling MRI: Clinical applications in the brain," *J. Magn. Reson. Imaging*, vol. 41, no. 5, pp. 1165–1180, May 2015.
- [15] R. P. H. Bokkers, M. J. P. Van Osch, H. B. Van Der Worp, G. J. De Borst, W. P. T. M. Mali, and J. Hendrikse, "Symptomatic carotid artery stenosis: Impairment of cerebral autoregulation measured at the brain tissue level with arterial spin-labeling MR imaging," *Radiology*, vol. 256, no. 1, pp. 201–208, Jul. 2010.
- [16] G. Zaharchuk, "Arterial spin-labeled perfusion imaging in acute ischemic stroke," *Stroke*, vol. 45, no. 4, Lippincott Williams and Wilkins, pp. 1202–1207, 2014.
- [17] D. A. Wolk and J. A. Detre, "Arterial spin labeling MRI: An emerging biomarker for Alzheimer's disease and other neurodegenerative conditions," *Current Opinion in Neurology*, vol. 25, no. 4, NIH Public Access, pp. 421–428, Aug-2012.
- [18] A. Odudu *et al.*, "Arterial spin labelling MRI to measure renal perfusion: a systematic review and statement paper," *Nephrol. Dial. Transplant.*, vol. 33, pp. 15–21, 2018.
- [19] Z. Zun and C. Limperopoulos, "Placental perfusion imaging using velocity-selective arterial spin labeling," *Magn. Reson. Med.*, vol. 80, no. 3, pp. 1036–1047, Sep. 2018.

- [20] R. B. Lauffer, "Paramagnetic Metal Complexes as Water Proton Relaxation Agents for NMR Imaging: Theory and Design," *Chem. Rev.*, vol. 87, no. 5, pp. 901–927, Aug. 1987.
- [21] L. Østergaard, "Principles of cerebral perfusion imaging by bolus tracking," in *Journal of Magnetic Resonance Imaging*, 2005, vol. 22, no. 6, pp. 710–717.
- [22] G. H. Jahng, K. L. Li, L. Østergaard, and F. Calamante, "Perfusion magnetic resonance imaging: A comprehensive update on principles and techniques," *Korean Journal of Radiology*, vol. 15, no. 5. Korean Radiological Society, pp. 554–577, 01-Sep-2014.
- [23] F. Khalifa *et al.*, "Models and methods for analyzing DCE-MRI: A review," *Med. Phys.*, vol. 41, no. 12, p. 124301, Dec. 2014.
- [24] J. M. Provenzale, G. R. Wang, T. Brenner, J. R. Petrella, and A. G. Sorensen, "Comparison of permeability in high-grade and low-grade brain tumors using dynamic susceptibility contrast MR imaging," *Am. J. Roentgenol.*, vol. 178, no. 3, pp. 711–716, Nov. 2002.
- [25] F. Yuan *et al.*, "Vascular Permeability in a Human Tumor Xenograft: Molecular Size Dependence and Cutoff Size," *Cancer Res.*, vol. 55, no. 17, 1995.
- [26] Y. Gao and S. L. Heller, "Abbreviated and ultrafast breast MRI in clinical practice," *Radiographics*, vol. 40, no. 6. Radiological Society of North America Inc., pp. 1507–1527, 01-Oct-2020.
- [27] T. J. Fraum, D. R. Ludwig, M. R. Bashir, and K. J. Fowler, "Gadolinium-based contrast agents: A comprehensive risk assessment," *J. Magn. Reson. Imaging*, vol. 46, no. 2, pp. 338–353, Aug. 2017.
- [28] E. Kanal, "Gadolinium based contrast agents (GBCA): Safety overview after 3 decades of clinical experience," *Magn. Reson. Imaging*, vol. 34, no. 10, pp. 1341–1345, Dec. 2016.
- [29] R. J. McDonald *et al.*, "Gadolinium Retention: A Research Roadmap from the 2018 NIH/ACR/RSNA Workshop on Gadolinium Chelates," *Radiology*, vol. 289, no. 2, pp. 517–534, Nov. 2018.
- [30] A. Radbruch *et al.*, "Gadolinium retention in the dentate nucleus and globus pallidus is dependent on the class of contrast agent," *Radiology*, vol. 275, no. 3, pp. 783–791, Jun. 2015.
- [31] J. A. Detre, J. S. Leigh, D. S. Williams, and A. P. Koretsky, "Perfusion imaging.," *Magn. Reson. Med.*, vol. 23, no. 1, pp. 37–45, Jan. 1992.
- [32] E. C. Wong, "An introduction to ASL labeling techniques," *J. Magn. Reson. Imaging*, vol. 40, no. 1, pp. 1–10, 2014.
- [33] K. L. LEENDERS *et al.*, "CEREBRAL BLOOD FLOW, BLOOD VOLUME AND OXYGEN UTILIZATION," *Brain*, vol. 113, no. 1, pp. 27–47, Feb. 1990.
- [34] L. R. Williams and R. W. Leggett, "Reference values for resting blood flow to organs of man," *Clinical Physics and Physiological Measurement*, vol. 10, no. 3. Clin Phys Physiol Meas, pp. 187–217, 1989.
- [35] M. Taso, A. Guidon, and D. C. Alsop, "Influence of background suppression and retrospective realignment on free-breathing renal perfusion measurement using pseudo-continuous ASL," *Magn. Reson. Med.*, vol. 81, no. 4, pp. 2439–2449, Apr. 2019.
- [36] I. K. Bones *et al.*, "Enabling free-breathing background suppressed renal pCASL using fat imaging and retrospective motion correction," *Magn. Reson. Med.*, vol. 82, pp. 276–288, Mar. 2019.
- [37] D. M. Garcia, G. Duhamel, and D. C. Alsop, "Efficiency of inversion pulses for background suppressed arterial spin labeling," *Magn. Reson. Med.*, vol. 54, no. 2, pp. 366–372, Aug. 2005.
- [38] W. Dai, D. Garcia, C. de Bazelaire, and D. C. Alsop, "Continuous flow-driven inversion for arterial spin labeling using pulsed radio frequency and gradient fields.," *Magn. Reson. Med.*, vol. 60, no. 6, pp. 1488–97, Dec. 2008.
- [39] D. W. Kim *et al.*, "Measurement of arterial transit time and renal blood flow using pseudocontinuous ASL MRI with multiple post-labeling delays: Feasibility, reproducibility, and variation," *J. Magn. Reson. Imaging*, vol. 46, no. 3, pp. 813–819, Sep. 2017.

- [40] E. T. Petersen, K. Mouridsen, and X. Golay, "The QUASAR reproducibility study, Part II: Results from a multi-center Arterial Spin Labeling test-retest study," *Neuroimage*, vol. 49, no. 1, pp. 104–113, Jan. 2010.
- [41] J. Hendrikse, E. T. Petersen, P. J. Van Laar, and X. Golay, "Cerebral border zones between distal end branches of intracranial arteries: MR imaging," *Radiology*, vol. 246, no. 2, pp. 572–580, Feb. 2008.
- [42] R. P. H. Bokkers, H. B. Van Der Worp, W. P. T. M. Mali, and J. Hendrikse, "Noninvasive MR imaging of cerebral perfusion in patients with a carotid artery stenosis," *Neurology*, vol. 73, no. 11, pp. 869–875, Sep. 2009.
- [43] D. S. Bolar *et al.*, "Comparison of CBF measured with combined velocity-selective arterial spin-labeling and pulsed arterial spin-labeling to blood flow patterns assessed by conventional angiography in pediatric Moyamoya," *Am. J. Neuroradiol.*, vol. 40, no. 11, pp. 1842–1849, 2019.
- [44] P. Korovessis, P. Iliopoulos, A. Misiris, and G. Koureas, "Color Doppler Ultrasonography for Evaluation of Internal Mammary Artery Application in Adolescent Female Patients with Right-Convex Thoracic Idiopathic Scoliosis," *Spine (Phila. Pa. 1976)*, vol. 28, no. 15, pp. 1746–1748, Aug. 2003.
- [45] R. A. Jesinger, G. E. Lattin, E. A. Ballard, S. M. Zelasko, and L. M. Glassman, "Vascular abnormalities of the breast: Arterial and venous disorders, vascular masses, and mimic lesions with radiologic-pathologic correlation," *Radiographics*, vol. 31, no. 7. Radiological Society of North America , 08-Dec-2011.
- [46] L. Zhao, M. Vidorreta, S. Soman, J. A. Detre, and D. C. Alsop, "Improving the robustness of pseudo-continuous arterial spin labeling to off-resonance and pulsatile flow velocity," *Magn. Reson. Med.*, vol. 78, no. 4, pp. 1342–1351, Oct. 2017.
- [47] H. Jahanian, D. C. Noll, and L. Hernandez-Garcia, " $B_0$  field inhomogeneity considerations in pseudo-continuous arterial spin labeling (pCASL): effects on tagging efficiency and correction strategy," *NMR Biomed.*, vol. 24, no. 10, pp. 1202–1209, Dec. 2011.
- [48] S.-G. Kim, "Quantification of relative cerebral blood flow change by flow sensitive alternating inversion recovery (FAIR) technique: Application to functional mapping," *Magn. Reson. Med.*, vol. 34, no. 3, pp. 293–301, 1995.
- [49] E. C. Wong, M. Cronin, W. C. Wu, B. Inglis, L. R. Frank, and T. T. Liu, "Velocity-selective arterial spin labeling," *Magn. Reson. Med.*, vol. 55, no. 6, pp. 1334–1341, Jun. 2006.
- [50] W. C. Wu and E. C. Wong, "Intravascular effect in velocity-selective arterial spin labeling: The choice of inflow time and cutoff velocity," *Neuroimage*, 2006.
- [51] S. Schmid, E. Ghariq, W. M. Teeuwisse, A. Webb, and M. J. P. van Osch, "Acceleration-selective arterial spin labeling," *Magn. Reson. Med.*, vol. 71, no. 1, pp. 191–199, Jan. 2014.
- [52] J. Guo and E. C. Wong, "Increased SNR efficiency in velocity selective arterial spin labeling using multiple velocity selective saturation modules (mm-VSASL)," *Magn. Reson. Med.*, vol. 74, pp. 694–705, 2015.
- [53] Q. Qin and P. C. M. van Zijl, "Velocity-selective-inversion prepared arterial spin labeling," *Magn. Reson. Med.*, vol. 76, no. 4, pp. 1136–1148, 2016.
- [54] R. W. Brown, Y. C. N. Cheng, E. M. Haacke, M. R. Thompson, and R. Venkatesan, *Magnetic Resonance Imaging: Physical Principles and Sequence Design: Second Edition*, vol. 9780471720. Chichester, UK: John Wiley & Sons Ltd, 2014.
- [55] M. Kobari, F. Gotoh, Y. Fukuuchi, K. Tanaka, N. Suzuki, and D. Uematsu, "Blood Flow Velocity in the Pial Arteries of Cats, with Particular Reference to the Vessel Diameter," *J. Cereb. Blood Flow Metab.*, vol. 4, pp. 110–114, 1984.
- [56] W.-C. Wu and E. C. Wong, "Intravascular effect in velocity-selective arterial spin labeling: The choice of inflow time and cutoff velocity," 2006.

- [57] J. Guo, J. A. Meakin, P. Jezzard, and E. C. Wong, "An optimized design to reduce eddy current sensitivity in velocity-selective arterial spin labeling using symmetric BIR-8 pulses," *Magn. Reson. Med.*, vol. 73, no. 3, pp. 1085–1094, Mar. 2015.
- [58] L. De Rochefort, X. Maitre, J. Bittoun, and E. Durand, "Velocity-selective RF pulses in MRI," *Magn. Reson. Med.*, vol. 55, no. 1, pp. 171–176, 2006.
- [59] J. F. Schenck, "The role of magnetic susceptibility in magnetic resonance imaging: MRI magnetic compatibility of the first and second kinds," *Med. Phys.*, vol. 23, no. 6, pp. 815–850, Jun. 1996.
- [60] M. A. Bernstein, J. Huston, and H. A. Ward, "Imaging artifacts at 3.0T," *Journal of Magnetic Resonance Imaging*, vol. 24, no. 4. John Wiley & Sons, Ltd, pp. 735–746, 01-Oct-2006.
- [61] K. J. Chang, I. R. Kamel, K. J. Macura, and D. A. Bluemke, "3.0-T MR imaging of the Abdomen: Comparison with 1.5 T," *Radiographics*, vol. 28, no. 7, pp. 1983–1998, Nov. 2008.
- [62] F. Nery *et al.*, "Consensus-based technical recommendations for clinical translation of renal ASL MRI," *Magn. Reson. Mater. Physics, Biol. Med.*, vol. 33, pp. 141–161, 2020.
- [63] N. Ben-Eliezer, Y. Shrot, and L. Frydman, "High-definition, single-scan 2D MRI in inhomogeneous fields using spatial encoding methods," *Magn. Reson. Imaging*, vol. 28, no. 1, pp. 77–86, Jan. 2010.
- [64] N. Ben-Eliezer, M. Irani, and L. Frydman, "Super-resolved spatially encoded single-scan 2D MRI," *Magn. Reson. Med.*, vol. 63, no. 6, pp. 1594–1600, 2010.
- [65] C. H. Lee *et al.*, "Breast Cancer Screening With Imaging: Recommendations From the Society of Breast Imaging and the ACR on the Use of Mammography, Breast MRI, Breast Ultrasound, and Other Technologies for the Detection of Clinically Occult Breast Cancer," *J. Am. Coll. Radiol.*, vol. 7, no. 1, pp. 18–27, Jan. 2010.
- [66] R. M. Mann, C. K. Kuhl, and L. Moy, "Contrast-enhanced MRI for breast cancer screening," *Journal of Magnetic Resonance Imaging*, vol. 50, no. 2. John Wiley and Sons Inc., pp. 377–390, 01-Aug-2019.
- [67] J. O. P. Wanders *et al.*, "Volumetric breast density affects performance of digital screening mammography," *Breast Cancer Res. Treat.*, vol. 162, no. 1, pp. 95–103, Feb. 2017.
- [68] S. G. A. Veenhuizen *et al.*, "Supplemental breast MRI for women with extremely dense breasts: Results of the second screening round of the DENSE trial," *Radiology*, vol. 299, no. 2, pp. 278–286, Mar. 2021.
- [69] J. S. Sung *et al.*, "Breast cancers detected at screening mr imaging and mammography in patients at high risk: Method of detection reflects tumor histopathologic results," *Radiology*, vol. 280, no. 3, pp. 716–722, Sep. 2016.
- [70] J. Folkman, "Clinical Applications of Research on Angiogenesis," *N. Engl. J. Med.*, vol. 333, no. 26, pp. 1757–1763, Dec. 1995.
- [71] I. Griebisch *et al.*, "Cost-effectiveness of screening with contrast enhanced magnetic resonance imaging vs X-ray mammography of women at a high familial risk of breast cancer," *Br. J. Cancer*, vol. 95, no. 7, pp. 801–810, Oct. 2006.
- [72] S. J. Lord *et al.*, "A systematic review of the effectiveness of magnetic resonance imaging (MRI) as an addition to mammography and ultrasound in screening young women at high risk of breast cancer," *Eur. J. Cancer*, vol. 43, no. 13, pp. 1905–1917, Sep. 2007.
- [73] T. Kanda, K. Ishii, H. Kawaguchi, K. Kitajima, and D. Takenaka, "High signal intensity in the dentate nucleus and globus pallidus on unenhanced T1-weighted MR images: Relationship with increasing cumulative dose of a gadoliniumbased contrast material," *Radiology*, vol. 270, no. 3, pp. 834–841, 2014.
- [74] W. C. Wu, S. Englander, S. M. D., and D.-J. Wang, "Feasibility of arterial spin labeling in the measurement of breast perfusion," in *Proceedings of the International Society for Magnetic Resonance in Medicine*, 2007, vol. 13, p. 2801.
- [75] S. Buchbender *et al.*, "Arterial spin labelling perfusion MRI of breast cancer using FAIR TrueFISP: Initial results," *Clin. Radiol.*, vol. 68, no. 3, pp. e123–e127, Mar. 2013.

- [76] M. Han *et al.*, “Breast Perfusion Imaging Using Arterial Spin Labeling,” *Proc. Int. Soc. Magn. Reson. Med.*, vol. 18, 2010.
- [77] M. Kawashima, Y. Katada, T. Shukuya, M. Kojima, and M. Nozaki, “MR perfusion imaging using the arterial spin labeling technique for breast cancer,” *J. Magn. Reson. Imaging*, vol. 35, no. 2, pp. 436–440, Feb. 2012.
- [78] D. W. Holdsworth, C. J. D. Norley, R. Frayne, D. A. Steinman, and B. K. Rutt, “Characterization of common carotid artery blood-flow waveforms in normal human subjects,” *Physiol. Meas.*, vol. 20, no. 3, pp. 219–240, Aug. 1999.
- [79] L. Hernandez-Garcia, J.-F. Nielsen, and D. C. Noll, “Improved sensitivity and temporal resolution in perfusion fMRI using velocity selective inversion ASL,” *Magn. Reson. Med.*, Sep. 2018.
- [80] W.-C. Wu and E. C. Wong, “Feasibility of Velocity Selective Arterial Spin Labeling in Functional MRI,” *J. Cereb. Blood Flow Metab.*, vol. 27, no. 4, pp. 831–838, Apr. 2007.
- [81] W.-C. Wu, Y. Mazaheri, and E. C. Wong, “The effects of flow dispersion and cardiac pulsation in arterial spin labeling,” *IEEE Trans. Med. Imaging*, vol. 26, no. 1, pp. 84–92, 2007.
- [82] Y. Fushimi, T. Okada, A. Yamamoto, M. Kanagaki, K. Fujimoto, and K. Togashi, “Timing dependence of peripheral pulse-wave-triggered pulsed arterial spin labeling,” *NMR Biomed.*, vol. 26, no. 11, pp. 1527–1533, 2013.
- [83] Y. Li *et al.*, “Cardiac-triggered pseudo-continuous arterial-spin-labeling: A cost-effective scheme to further enhance the reliability of arterial-spin-labeling MRI,” *Magn. Reson. Med.*, vol. 975, no. January, pp. 969–975, 2018.
- [84] X. Golay, E. T. Petersen, and F. Hui, “Pulsed Star Labeling of Arterial Regions (PULSAR): A robust regional perfusion technique for high field imaging,” *Magn. Reson. Med.*, vol. 53, no. 1, pp. 15–21, Jan. 2005.
- [85] P. Liu, J. Uh, and H. Lu, “Determination of spin compartment in arterial spin labeling MRI,” *Magn. Reson. Med.*, vol. 65, no. 1, pp. 120–127, Jan. 2011.
- [86] Z. Chen, X. Zhang, C. Yuan, X. Zhao, and M. J. P. van Osch, “Measuring the labeling efficiency of pseudocontinuous arterial spin labeling,” *Magn. Reson. Med.*, vol. 77, no. 5, pp. 1841–1852, May 2017.
- [87] M. S. Dagli, J. E. Ingeholm, and J. V Haxby, “Localization of Cardiac-Induced Signal Change in fMRI.”
- [88] W.-C. Wen-Chau Wu, B. L. Edlow, M. A. Elliot, J. Jiongjiang Wang, and J. A. Detre, “Physiological Modulations in Arterial Spin Labeling Perfusion Magnetic Resonance Imaging,” *IEEE Trans. Med. Imaging*, vol. 28, no. 5, pp. 703–709, May 2009.
- [89] K. Restom, Y. Behzadi, and T. T. Liu, “Physiological noise reduction for arterial spin labeling functional MRI,” 2006.
- [90] J. Verbree and M. J. P. Van Osch, “Magnetic Resonance Materials in Physics , Biology and Medicine Influence of the cardiac cycle on pCASL : cardiac triggering of the end-of-labeling,” *Magn. Reson. Mater. Physics, Biol. Med.*, 2017.
- [91] M. S. Hassanpour *et al.*, “Cardiorespiratory noise correction improves the ASL signal,” *Hum. Brain Mapp.*, vol. 39, no. 6, pp. 2353–2367, Jun. 2018.
- [92] M. F. O’Rourke and M. E. Safar, “Relationship between aortic stiffening and microvascular disease in brain and kidney: Cause and logic of therapy,” *Hypertension*, vol. 46, no. 1, pp. 200–204, 2005.
- [93] G. F. Mitchell, “Effects of central arterial aging on the structure and function of the peripheral vasculature: implications for end-organ damage,” *J Appl Physiol*, vol. 105, no. 4, pp. 1652–1660, 2008.
- [94] W. H. Bouvy *et al.*, “Assessment of blood flow velocity and pulsatility in cerebral perforating arteries with 7-T quantitative flow MRI,” *NMR Biomed.*, vol. 29, no. 9, pp. 1295–1304, Sep. 2016.
- [95] D. Qiu, M. Straka, Z. Zun, R. Bammer, M. E. Moseley, and G. Zaharchuk, “CBF measurements using multidelay pseudocontinuous and velocity-selective arterial spin labeling in patients with long arterial



transit delays: Comparison with xenon CT CBF," *J. Magn. Reson. Imaging*, vol. 36, no. 1, pp. 110–119, Jul. 2012.

- [96] T. Shin, P. W. Worters, B. S. Hu, and D. G. Nishimura, "Non-contrast-enhanced renal and abdominal MR angiography using velocity-selective inversion preparation," *Magn. Reson. Med.*, vol. 69, no. 5, pp. 1268–1275, 2013.
- [97] I. K. Bones *et al.*, "Influence of labeling parameters of velocity selective arterial spin labeling for renal perfusion imaging," *Magn. Reson. Med.*, pp. 1–26, 2020.
- [98] W. Dai *et al.*, "Effects of arterial transit delay on cerebral blood flow quantification using arterial spin labeling in an elderly cohort," *J. Magn. Reson. Imaging*, vol. 45, no. 2, pp. 472–481, Feb. 2017.
- [99] O. Togao *et al.*, "Acceleration-selective Arterial Spin-labeling MR Angiography Used to Visualize Distal Cerebral Arteries and Collateral Vessels in Moyamoya Disease," *Radiology*, vol. 286, no. 2, pp. 611–621, Feb. 2018.
- [100] R. D. Safian and S. C. Textor, "Renal-Artery Stenosis," *N. Engl. J. Med.*, vol. 344, no. 6, pp. 431–442, Feb. 2001.
- [101] R. R. Edelman and I. Koztzoğlu, "Noncontrast MR angiography: An update," *Journal of Magnetic Resonance Imaging*, vol. 49, no. 2. John Wiley and Sons Inc., pp. 355–373, 01-Feb-2019.
- [102] H. Jahanian, D. C. Noll, and L. Hernandez-Garcia, "B<sub>0</sub> field inhomogeneity considerations in pseudo-continuous arterial spin labeling (pCASL): Effects on tagging efficiency and correction strategy," *NMR Biomed.*, vol. 24, no. 10, pp. 1202–1209, Dec. 2011.
- [103] J. S. Greer, Y. Wang, I. Pedrosa, and A. J. Madhuranthakam, "Pseudo-continuous arterial spin labeled renal perfusion imaging at 3T with improved robustness to off-resonance," *Proc. Int. Soc. Magn. Reson. Med. Montr. Canada#4959*, pp. 1–4, 2019.
- [104] N. M. Selby *et al.*, "Magnetic resonance imaging biomarkers for chronic kidney disease: a position paper from the European Cooperation in Science and Technology Action PARENCHIMA," *Nephrol. Dial. Transplant.*, vol. 33, no. suppl\_2, pp. ii4–ii14, Sep. 2018.
- [105] D. G. Norris and C. Schwarzbauer, "Velocity Selective Radiofrequency Pulse Trains," *J Magn Reson*, vol. 137, pp. 231–236, 1999.
- [106] S. Schmid, E. T. Petersen, and M. J. P. Van Osch, "Insight into the labeling mechanism of acceleration selective arterial spin labeling," *Magn. Reson. Mater. Physics, Biol. Med.*, pp. 1–10, Oct. 2016.
- [107] R. J. Ogg, P. B. Kingsley, and J. S. Taylor, "WET, a T<sub>1</sub>- and B<sub>1</sub>-Insensitive Water-Suppression Method for in Vivo Localized 1H NMR Spectroscopy," *J. Magn. Reson. Ser. B*, vol. 104, no. 1, pp. 1–10, 1994.
- [108] A. A. Harteveld, A. de Boer, S. L. Franklin, T. Leiner, M. van Stralen, and C. Bos, "Comparison of multi-delay FAIR and pCASL labeling approaches for renal perfusion quantification at 3T MRI," *Magn. Reson. Mater. Physics, Biol. Med.*, vol. 33, no. 1, pp. 81–94, Feb. 2019.
- [109] W. Luh, E. C. Wong, P. A. Bandettini, and J. S. Hyde, "QUIPSS II with thin-slice T<sub>1</sub> periodic saturation: A method for improving accuracy of quantitative perfusion imaging using pulsed arterial spin labeling," *Magn. Reson. Med.*, vol. 41, no. 6, pp. 1246–1254, Jun. 1999.
- [110] S. Clare and P. Jezzard, "RapidT<sub>1</sub> mapping using multislice echo planar imaging," *Magn. Reson. Med.*, vol. 45, no. 4, pp. 630–634, Apr. 2001.
- [111] V. L. Yarnykh, "Actual flip-angle imaging in the pulsed steady state: A method for rapid three-dimensional mapping of the transmitted radiofrequency field," *Magn. Reson. Med.*, vol. 57, no. 1, pp. 192–200, Jan. 2007.
- [112] W. Penny, K. Friston, J. Ashburner, S. Kiebel, and T. Nichols, *Statistical Parametric Mapping: The Analysis of Functional Brain Images*. Elsevier Ltd, 2007.
- [113] F. Ritter *et al.*, "Medical image analysis," *IEEE Pulse*, vol. 2, no. 6, pp. 60–70, Nov. 2011.

- [114] W. Huizinga *et al.*, “PCA-based groupwise image registration for quantitative MRI,” *Med. Image Anal.*, vol. 29, pp. 65–78, Apr. 2016.
- [115] J. A. Meakin and P. Jezzard, “An optimized velocity selective arterial spin labeling module with reduced eddy current sensitivity for improved perfusion quantification,” *Magn. Reson. Med.*, vol. 69, no. 3, pp. 832–838, 2013.
- [116] T. L. Pallone, A. Edwards, and D. L. Mattson, “Renal medullary circulation,” *Compr. Physiol.*, vol. 2, no. 1, pp. 97–140, Jan. 2012.
- [117] P. M. Robson, A. J. Madhuranthakam, W. Dai, I. Pedrosa, N. M. Rofsky, and D. C. Alsop, “Strategies for reducing respiratory motion artifacts in renal perfusion imaging with arterial spin labeling,” *Magn. Reson. Med.*, vol. 61, no. 6, pp. 1374–1387, Jun. 2009.
- [118] S. L. Franklin, S. Schmid, C. Bos, and M. J. P. van Osch, “Influence of the cardiac cycle on velocity selective and acceleration selective arterial spin labeling,” *Magn. Reson. Med.*, vol. 83, no. 3, pp. 872–882, Mar. 2020.
- [119] R. Echeverria-Chasco, M. Vidorreta, V. Aramendia-Vidaurreta, G. Bastarrika, and M. A. Fernandez-Seara, “Optimization of Pseudo Continuous Arterial Spin Labeling for renal ASL,” *Proc. Int. Soc. Magn. Reson. Med. Montr. Canada#4954*, pp. 1–4, 2019.
- [120] M. Schmitt *et al.*, “Improved uniformity of RF-distribution in clinical whole body-imaging at 3T by means of dielectric pads,” in *Proceedings of International Society for Magnetic Resonance in medicine, Toronto, Canada, 2004*.
- [121] T. Shin, B. S. Hu, and D. G. Nishimura, “Off-resonance-robust velocity-selective magnetization preparation for non-contrast-enhanced peripheral MR angiography,” *Magn. Reson. Med.*, vol. 70, no. 5, pp. 1229–1240, 2013.
- [122] Q. Qin, T. Shin, M. Schär, H. Guo, H. Chen, and Y. Qiao, “Velocity-selective magnetization-prepared non-contrast-enhanced cerebral MR angiography at 3 Tesla: Improved immunity to B0/B1 inhomogeneity,” *Magn. Reson. Med.*, vol. 75, no. 3, pp. 1232–1241, Mar. 2016.
- [123] W. Li *et al.*, “Whole-brain arteriography and venography: Using improved velocity-selective saturation pulse trains,” *Magn. Reson. Med.*, vol. 79, no. 4, pp. 2014–2023, Apr. 2018.
- [124] D. Zhu *et al.*, “Non-contrast-enhanced abdominal MRA at 3 T using velocity-selective pulse trains,” *Magn Reson Med*, vol. 84, no. 3, pp. 1173–1183, Feb. 2020.
- [125] V. Landes, A. Javed, T. Jao, Q. Qin, and K. Nayak, “Improved velocity-selective labeling pulses for myocardial ASL,” *Magn. Reson. Med.*, vol. 84, no. 4, pp. 1909–1918, 2020.
- [126] M. Taso, A. Guidon, and D. C. Alsop, “Influence of background suppression and retrospective realignment on free-breathing renal perfusion measurement using pseudo-continuous ASL,” *Magn. Reson. Med.*, vol. 81, no. 4, pp. 2439–2449, Apr. 2019.
- [127] A. Matakos, J. M. Balter, and Y. Cao, “A Robust Method for Estimating B0 Inhomogeneity Field in the Liver by Mitigating Fat Signals and Phase-Wrapping,” *Magn Reson Med*, vol. 3, no. 2, pp. 79–88, 2017.
- [128] M. Schär, E.-J. Vonken, M. Stuber, and R. H. Morgan, “Simultaneous B 0-and B 1 +-map Acquisition for Fast Localized Shim, Frequency and RF Power Determination in the Heart at 3T,” vol. 63, no. 2, pp. 419–426, 2010.
- [129] M. A. Marino, T. Helbich, P. Baltzer, and K. Pinker-Domenig, “Multiparametric MRI of the breast: A review,” *J. Magn. Reson. Imaging*, vol. 47, no. 2, pp. 301–315, Feb. 2018.
- [130] D. Saslow *et al.*, “American Cancer Society Guidelines for Breast Screening with MRI as an Adjunct to Mammography,” *CA. Cancer J. Clin.*, vol. 57, no. 2, pp. 75–89, Mar. 2007.
- [131] R. M. Mann, N. Cho, and L. Moy, “Breast MRI: State of the art,” *Radiology*, vol. 292, no. 3, pp. 520–536, Jul. 2019.

- [132] H. Abe *et al.*, “Kinetic analysis of benign and malignant breast lesions with ultrafast dynamic contrast-enhanced MRI: Comparison with standard kinetic assessment,” *Am. J. Roentgenol.*, vol. 207, no. 5, pp. 1159–1166, Nov. 2016.
- [133] J. C. M. Van Zelst *et al.*, “Multireader Study on the Diagnostic Accuracy of Ultrafast Breast Magnetic Resonance Imaging for Breast Cancer Screening,” *Invest. Radiol.*, vol. 53, no. 10, pp. 579–586, Oct. 2018.
- [134] S.-G. Kim, “Quantification of relative cerebral blood flow change by flow-sensitive alternating inversion recovery (FAIR) technique: Application to functional mapping,” *Magn. Reson. Med.*, vol. 34, no. 3, pp. 293–301, Sep. 1995.
- [135] E. Kaldoudi, S. C. R. Williams, G. J. Barker, and P. S. Tofts, “A chemical shift selective inversion recovery sequence for fat-suppressed MRI: Theory and experimental validation,” *Magn. Reson. Imaging*, vol. 11, no. 3, pp. 341–355, 1993.
- [136] T. C. Lauenstein, P. Sharma, T. Hughes, K. Heberlein, D. Tudorascu, and D. R. Martin, “Evaluation of optimized inversion-recovery fat-suppression techniques for T2-weighted abdominal MR imaging,” *J. Magn. Reson. Imaging*, vol. 27, no. 6, pp. 1448–1454, May 2008.
- [137] C. D’Orsi, E. Sickles, E. Mendelson, and E. Morris, *Breast Imaging Reporting and Data System: ACR BI-RADS breast imaging atlas*, 5th ed. Reston: American College of Radiology, 2013.
- [138] D. Hanahan and J. Folkman, “Patterns and Emerging Mechanisms Review of the Angiogenic Switch during Tumorigenesis,” *Cell*, vol. 86, pp. 353–364, 1996.
- [139] W.-C. Wu, S. England, M. Schnell, and J. Wang, “Feasibility of arterial spin labeling in the measurement of breast perfusion,” 2007.
- [140] M. Goto *et al.*, “Diagnostic performance of initial enhancement analysis using ultra-fast dynamic contrast-enhanced MRI for breast lesions,” *Eur. Radiol.*, vol. 29, no. 3, pp. 1164–1174, Mar. 2019.
- [141] N. Onishi *et al.*, “Ultrafast dynamic contrast-enhanced breast MRI may generate prognostic imaging markers of breast cancer,” *Breast Cancer Res.*, vol. 22, no. 1, p. 58, May 2020.
- [142] A. C. Schmitz *et al.*, “Contrast-enhanced 3.0-T breast MRI for characterization of breast lesions: Increased specificity by using vascular maps,” *Eur. Radiol.*, vol. 18, no. 2, pp. 355–364, Feb. 2008.
- [143] C. Wu, F. Pineda, D. A. Hormuth, G. S. Karczmar, and T. E. Yankeelov, “Quantitative analysis of vascular properties derived from ultrafast DCE-MRI to discriminate malignant and benign breast tumors,” *Magn. Reson. Med.*, vol. 81, no. 3, pp. 2147–2160, Mar. 2019.
- [144] S. Mani, J. Pauly, S. Conolly, C. Meyer, and D. Nishimura, “Background suppression with multiple inversion recovery nulling: Applications to projective angiography,” *Magn. Reson. Med.*, vol. 37, no. 6, pp. 898–905, 1997.
- [145] S. L. Franklin *et al.*, “Multi-organ comparison of flow-based arterial spin labeling techniques: Spatially non-selective labeling for cerebral and renal perfusion imaging,” *Magn Reson Med*, pp. 7–8, 2020.
- [146] D. Liu, W. Li, F. Xu, D. Zhu, T. Shin, and Q. Qin, “Ensuring both velocity and spatial responses robust to field inhomogeneities for velocity-selective arterial spin labeling through dynamic phase-cycling,” *Magn. Reson. Med.*, p. mrm.28622, Dec. 2020.
- [147] L. Hernandez-Garcia, A. Lahiri, and J. Schollenberger, “Recent progress in ASL,” *NeuroImage*, vol. 187. Academic Press Inc., pp. 3–16, 15-Feb-2019.
- [148] S. L. Franklin *et al.*, “Multi-organ comparison of flow-based arterial spin labeling techniques: Spatially non-selective labeling for cerebral and renal perfusion imaging,” *Magn. Reson. Med.*, vol. 85, no. 5, pp. 2580–2594, May 2021.
- [149] A. A. Harteveld *et al.*, “Systematic evaluation of velocity-selective arterial spin labeling settings for placental perfusion measurement,” *Magn. Reson. Med.*, vol. 84, no. 4, pp. 1828–1843, Oct. 2020.

- [150] P. Martirosian *et al.*, “Spatial-temporal perfusion patterns of the human liver assessed by pseudo-continuous arterial spin labeling MRI,” *Z. Med. Phys.*, vol. 29, no. 2, pp. 173–183, May 2019.
- [151] S. C. Partridge, N. Nissan, H. Rahbar, A. E. Kitsch, and E. E. Sigmund, “Diffusion-weighted breast MRI: Clinical applications and emerging techniques,” *Journal of Magnetic Resonance Imaging*, vol. 45, no. 2. John Wiley and Sons Inc., pp. 337–355, 01-Feb-2017.
- [152] R. Goetti, R. O’gorman, N. Khan, C. J. Kellenberger, and I. Scheer, “Arterial spin labelling MRI for assessment of cerebral perfusion in children with moyamoya disease: comparison with dynamic susceptibility contrast MRI.”
- [153] W. G. Bradley, “MR Appearance of Hemorrhage in the Brain’.”
- [154] A. Dumas *et al.*, “Functional magnetic resonance imaging detection of vascular reactivity in cerebral amyloid angiopathy,” *Ann. Neurol.*, vol. 72, no. 1, pp. 76–81, Jul. 2012.
- [155] Y. Shrot and L. Frydman, “Spatially encoded NMR and the acquisition of 2D magnetic resonance images within a single scan,” *J. Magn. Reson.*, vol. 172, no. 2, pp. 179–190, Feb. 2005.
- [156] N. Ben-Eliezer, U. Goerke, K. Ugurbil, and L. Frydman, “Functional MRI using super-resolved spatiotemporal encoding,” *Magn. Reson. Imaging*, vol. 30, no. 10, pp. 1401–1408, Dec. 2012.
- [157] E. Solomon, G. Liberman, N. Nissan, E. Furman-Haran, M. Sklair-Levy, and L. Frydman, “Diffusion-weighted breast MRI of malignancies with submillimeter resolution and immunity to artifacts by spatiotemporal encoding at 3T,” *Magn. Reson. Med.*, vol. 84, no. 3, pp. 1391–1403, Sep. 2020.
- [158] U. Goerke, M. Garwood, and K. Ugurbil, “Functional magnetic resonance imaging using RASER,” *Neuroimage*, vol. 54, no. 1, pp. 350–360, Jan. 2011.
- [159] A. M. Airaksinen *et al.*, “Simultaneous fMRI and local field potential measurements during epileptic seizures in medetomidine sedated rats using RASER pulse sequence.”
- [160] N. Ben-Eliezer, E. Solomon, E. Harel, N. Nevo, and L. Frydman, “Fully refocused multi-shot spatiotemporally encoded MRI: Robust imaging in the presence of metallic implants,” *Magn. Reson. Mater. Physics, Biol. Med.*, vol. 25, no. 6, pp. 433–442, Dec. 2012.
- [161] R. Schmidt, B. Baishya, N. Ben-Eliezer, A. Seginer, and L. Frydman, “Super-resolved Parallel MRI by Spatiotemporal Encoding,” *Magn. Reson. Imaging*, vol. 32, pp. 60–70, 2014.
- [162] N. Ben-Eliezer, Y. Shrot, L. Frydman, and D. K. Sodickson, “Parametric analysis of the spatial resolution and signal-to-noise ratio in super-resolved spatiotemporally encoded (SPEN) MRI,” *Magn. Reson. Med.*, vol. 72, no. 2, pp. 418–429, 2014.
- [163] A. Tal and L. Frydman, “Single-scan multidimensional magnetic resonance,” *Progress in Nuclear Magnetic Resonance Spectroscopy*, vol. 57, no. 3. Elsevier B.V., pp. 241–292, 01-Oct-2010.
- [164] G. Liberman, E. Solomon, M. Lustig, and L. Frydman, “Multiple-coil k-space interpolation enhances resolution in single-shot spatiotemporal MRI,” *Magn. Reson. Med.*, vol. 79, no. 2, pp. 796–805, Feb. 2018.
- [165] A. Seginer, R. Schmidt, A. Leftin, E. Solomon, and L. Frydman, “Referenceless reconstruction of spatiotemporally encoded imaging data: Principles and applications to real-time MRI,” *Magn. Reson. Med.*, vol. 72, no. 6, pp. 1687–1695, Dec. 2014.
- [166] S. F. Cousin, G. Liberman, E. Solomon, M. Otkovs, and L. Frydman, “A regularized reconstruction pipeline for high-definition diffusion MRI in challenging regions incorporating a per-shot image correction,” *Magn. Reson. Med.*, vol. 82, no. 4, pp. 1322–1330, Oct. 2019.
- [167] K. M. Koch, B. A. Hargreaves, K. B. Pauly, W. Chen, G. E. Gold, and K. F. King, “Magnetic resonance imaging near metal implants,” *Journal of magnetic resonance imaging : JMRI*, vol. 32, no. 4. John Wiley & Sons, Ltd, pp. 773–787, 01-Oct-2010.
- [168] L. Chen *et al.*, “Super-resolved enhancing and edge deghosting (SEED) for spatiotemporally encoded single-shot MRI,” *Med. Image Anal.*, vol. 23, no. 1, pp. 1–14, Jul. 2015.

- [169] F. Nery, E. De Vita, C. A. Clark, I. Gordon, and D. L. Thomas, "Robust kidney perfusion mapping in pediatric chronic kidney disease using single-shot 3D-GRASE ASL with optimized retrospective motion correction," *Magn. Reson. Med.*, vol. 81, no. 5, pp. 2972–2984, May 2019.
- [170] T. Nguyen, U. Goerke, S. Moeller, K. Ugurbil, and M. Garwood, "Parallel Imaging with RASER Using Multiband Frequency-Modulated Excitation Pulses (ISMRM 2009)." [Online]. Available: <https://archive.ismrm.org/2009/2738.html>. [Accessed: 05-Mar-2021].
- [171] R. Schmidt and L. Frydman, "New Spatiotemporal Approaches for Fully-Refocused, Multi-Slice Ultrafast 2D MRI," *Magn. Reson. Med.*, vol. 71, no. 2, p. 711, 2014.
- [172] T. Zhang *et al.*, "Ultrafast multi-slice spatiotemporally encoded MRI with slice-selective dimension segmented," *J. Magn. Reson.*, vol. 269, pp. 138–145, Aug. 2016.
- [173] R. Corti *et al.*, "Imaging of atherosclerosis: magnetic resonance imaging," *Eur. Heart J.*, vol. 32, no. 14, pp. 1709–19b, Jul. 2011.
- [174] K. Oshio and D. A. Feinberg, "GRASE (Gradient-and Spin-Echo) imaging: A novel fast MRI technique," *Magn. Reson. Med.*, vol. 20, no. 2, pp. 344–349, Aug. 1991.
- [175] J. Hennig and H. Friedburg, "Clinical applications and methodological developments of the RARE technique," *Magn. Reson. Imaging*, vol. 6, no. 4, pp. 391–395, Jul. 1988.
- [176] M. Taso, L. Zhao, A. Guidon, D. V. Litwiller, and D. C. Alsop, "Volumetric abdominal perfusion measurement using a pseudo-randomly sampled 3D fast-spin-echo (FSE) arterial spin labeling (ASL) sequence and compressed sensing reconstruction," *Magn. Reson. Med.*, vol. 82, no. 2, pp. 680–692, Aug. 2019.
- [177] J. S. Greer *et al.*, "Robust pCASL perfusion imaging using a 3D Cartesian acquisition with spiral profile reordering (CASPR)," *Magn. Reson. Med.*, vol. 82, no. 5, pp. 1713–1724, Nov. 2019.
- [178] Z. Zhang, M. Lustig, and L. Frydman, "Phase-encoded xSPEN: A novel high-resolution volumetric alternative to RARE MRI," *Magn. Reson. Med.*, vol. 80, no. 4, pp. 1492–1506, Oct. 2018.
- [179] "Handbook of MRI Pulse Sequences - Matt A. Bernstein, Kevin F. King, Xiaohong Joe Zhou - Google Books." [Online]. Available: [https://books.google.nl/books/about/Handbook\\_of\\_MRI\\_Pulse\\_Sequences.html?id=d6PLHcyejEIC&redir\\_esc=y](https://books.google.nl/books/about/Handbook_of_MRI_Pulse_Sequences.html?id=d6PLHcyejEIC&redir_esc=y). [Accessed: 07-Mar-2021].
- [180] J. G. Pipe, "Spatial Encoding and Reconstruction in MRI with Quadratic Phase Profiles," *Magn. Reson. Med.*, vol. 33, no. 1, pp. 24–33, Jan. 1995.
- [181] D. WT, S. M, C. M, and S. GP, "Multiple inversion recovery reduces static tissue signal in angiograms," *Magn. Reson. Med.*, vol. 18, no. 2, pp. 257–268, 1991.
- [182] J. Baum, R. Tycko, and A. Pines, "Broadband and adiabatic inversion of a two-level system by phase-modulated pulses," *Phys. Rev. A*, vol. 32, no. 6, pp. 3435–3447, Dec. 1985.
- [183] A. Tannus and M. Garwood, "Adiabatic pulses," *NMR Biomed.*, vol. 10, pp. 423–434, 1997.
- [184] R. S. STAEWEN, A. J. JOHNSON, B. D. ROSS, T. PARRISH, H. MERKLE, and M. GARWOOD, "3-D FLASH Imaging Using a Single Surface Coil and a New Adiabatic Pulse, BIR-4," *Invest. Radiol.*, vol. 25, no. 5, pp. 559–567, May 1990.
- [185] R. J. Ordidge, M. Wylezinska, J. W. Hugg, E. Butterworth, and F. Franconi, "Frequency offset corrected inversion (FOCI) pulses for use in localized spectroscopy," *Magn. Reson. Med.*, vol. 36, no. 4, pp. 562–566, 1996.
- [186] M. N. Yongbi, C. A. Branch, and J. A. Helpert, "Perfusion imaging using FOCI RF pulses," *Magn. Reson. Med.*, vol. 40, no. 6, pp. 938–943, Dec. 1998.
- [187] H. Lu, C. Clingman, X. Golay, and P. C. M. van Zijl, "Determining the longitudinal relaxation time (T1) of blood at 3.0 Tesla," *Magn. Reson. Med.*, vol. 52, no. 3, pp. 679–682, Sep. 2004.
- [188] C. JJ and P. GB, "Human whole blood T2 relaxometry at 3 Tesla," *Magn. Reson. Med.*, vol. 61, no. 2, pp. 249–254, 2009.

- [189] D. Liu, F. Xu, W. Li, P. C. van Zijl, D. D. Lin, and Q. Qin, "Improved velocity-selective-inversion arterial spin labeling for cerebral blood flow mapping with 3D acquisition," *Magn. Reson. Med.*, vol. 84, no. 5, pp. 2512–2522, Nov. 2020.
- [190] N. T. Roberts, L. A. Hinshaw, T. J. Colgan, T. Li, D. Hernando, and S. B. Reeder, "B0 and B1 inhomogeneities in the liver at 1.5 T and 3.0 T," *Magn. Reson. Med.*, vol. 85, no. 4, pp. 2212–2220, Apr. 2021.
- [191] J. Moore, M. Jankiewicz, A. W. Anderson, and J. C. Gore, "Evaluation of non-selective refocusing pulses for 7 T MRI," *J. Magn. Reson.*, vol. 214, pp. 212–220, Jan. 2012.
- [192] J. Guo, S. Das, and L. Hernandez-Garcia, "Comparison of velocity-selective arterial spin labeling schemes," *Magn. Reson. Med.*, vol. 85, no. 4, pp. 2027–2039, Apr. 2021.
- [193] D. Liu, W. Li, F. Xu, D. Zhu, T. Shin, and Q. Qin, "Ensuring both velocity and spatial responses robust to B0/B1+ field inhomogeneities for velocity-selective arterial spin labeling through dynamic phase-cycling," *Magn. Reson. Med.*, vol. 85, no. 5, pp. 2723–2734, May 2021.
- [194] W. R. Nitz, "Fast and ultrafast non-echo-planar MR imaging techniques," *Eur. Radiol.*, vol. 12, no. 12, pp. 2866–2882, Dec. 2002.
- [195] A. de Boer *et al.*, "Multiparametric Renal MRI: An Intrasubject Test–Retest Repeatability Study," *J. Magn. Reson. Imaging*, vol. 53, no. 3, pp. 859–873, Mar. 2021.



# Chapter 10

---

**List of publications**

---





1. [S.L. Franklin](#), N. Voormolen, I.K. Bones, T. Korteweg, M.N.J.M. Wasser, H.G. Dankers, D. Cohen, M. Van Stralen, C. Bos and M.J.P. van Osch (2021). Feasibility of Velocity-Selective Arterial Spin Labeling in breast cancer patients for non-contrast enhanced perfusion imaging. *jMRI*, 54(4):1282-1291.
2. [S.L. Franklin](#), I. Bones, A. Hartevelde, L. Hirschler, M. van Stralen, Q. Qin, A. de Boer, J. Hoogduin, C. Bos, M.J.P. van Osch, S. Schmidt (2020). Multi-organ comparison of flow-based Arterial Spin Labeling techniques. *Mag Res Med*, 85(5):2580-2594.
3. [S.L. Franklin](#), S. Schmid, C. Bos, M.J.P. van Osch (2019). Influence of the cardiac cycle on velocity selective and acceleration selective arterial spin labeling. *Mag Res Med*, 83(3):872-882.
4. I.K. Bones, [S.L. Franklin](#), A.A. Hartevelde, M.J.P. van Osch, S. Schmid, J. Hendrikse, C.T. Moonen, M. van Stralen, C. Bos, (2020). Exploring label dynamics of velocity-selective arterial spin labeling in the kidney. *Mag Res Med*, 86(1): 131-142.
5. I.K. Bones, [S.L. Franklin](#), A.A. Hartevelde, M.J.P. van Osch, J. Hendrikse, C.T. Moonen, M. van Stralen, C. Bos, (2020). Influence of labelling parameters and respiratory motion on velocity-selective ASL for renal perfusion imaging. *Mag Res Med*, 84(4):1919-1932.
6. I.K. Bones, A.A. Hartevelde, [S.L. Franklin](#), M.J.P. van Osch, J. Hendrikse, C.T.W. Moonen, C. Bos, M. van Stralen (2019). Enabling free-breathing background suppression renal pCASL using fat imaging and retrospective motion correction. *Mag Res Med*, 82(1):276-288.
7. A.A. Hartevelde, A. de Boer, [S.L. Franklin](#), T. Leiner, M. van Stralen, C. Bos (2019). Comparison of multi-delay FAIR and pCASL labeling approaches for renal perfusion quantification at 3T MRI. *MAGMA*, 33:81-94.
8. A.A. Hartevelde, J. Hutter, [S.L. Franklin](#), L. Jackson, M. Rutherford, J. Hajnal, M.J.P. van Osch, C. Bos, E. De Vita (2020). Systematic evaluation of velocity-selective arterial spin labeling settings for placental perfusion measurement. *Mag Res Med*, 84(4):1828-1843.
9. J. Hutter, A.A. Hartevelde, L.H. Jackson, [S.L. Franklin](#), C. Bos, M.J.P. van Osch, J. O'Muircheartaigh, A. Ho, L. Chappell, J. V. Hajnal, M. Rutherford, E. De Vita (2018). Perfusion and apparent oxygenation in human placenta (PERFOX). *Mag Res Med*; 83(2):549-560.
10. C. Baligand, L. Hirschler, T.T.J. Veeger, L. Vaclavu, [S.L. Franklin](#), M.J.P. van Osch, H.E. Kan (2021). A split-label design for simultaneous measurements of perfusion in distant slices by pulsed arterial spin labelling. *Magn Res Med*, 86(5):2441-2453.



# Chapter 11

---

**Curriculum vitae**

---



Suzanne Franklin was born on the 24<sup>th</sup> of May 1990 in Eindhoven, the Netherlands. She started her university career in Nijmegen, where she studied Physics, specializing in neuroscience to fulfill her life-long fascination with the brain. After two years she decided to switch to a more applied scientific field and went on to study Psychology at the Vrije Universiteit (VU) in Amsterdam. At the Vrije Universiteit, Suzanne obtained her Psychology bachelor's degree cum laude. She specialized in Biological Psychology, which focused on unraveling the underlying mechanisms of the brain. In addition, she participated in the Honours program to follow extracurricular courses.

After obtaining her bachelor's degree, Suzanne went on to do her master's in Biomedical Engineering at the Technical University in Eindhoven. Here, she specialized in Magnetic Resonance Imaging under supervision of prof. Klaas Nicolay. Suzanne was first introduced to non-contrast body imaging during her internship at King's College London, where she worked on a non-contrast technique to visualize the renal arteries under supervision of prof. René Botnar. This spiked her interest for non-contrast imaging and pulse programming of MR-sequences, which led to her starting a PhD-project in Arterial Spin Labeling with Thijs van Osch and Clemens Bos. The PhD-project was a joint-collaboration of Leiden University Medical Center and University Medical Center Utrecht.

Following her PhD, Suzanne briefly worked at 3mensio, developing machine learning solutions for medical image analysis. Currently, Suzanne works as pulse programming developer of novel MR sequences at Philips Healthcare.



# Chapter 11

---

## Acknowledgements

---





First and foremost I would like to say that I have thoroughly enjoyed my time as a PhD candidate. I felt completely at home in between the researchers at the LUMC and UMCU, which is a feeling that I did not always experience during my university career. This feeling is partly thanks to the commitment of Thijs and Clemens as my supervisors, but also because of the great atmosphere in both research groups. Despite my shared position in het LUMC and UMCU, I have never felt like there was any competition between the two, which is definitely not always the case in science.

Thijs, I greatly appreciate how you could always free up time in your busy schedule whenever I got stuck. Our discussions were as helpful as they were enjoyable. You have stimulated me to think for myself and be creative, and besides the scientific support, you always had attention for the personal side. You have set a great example, and inspired me both as a researcher and as a group lead. It was very stimulating to be part of your 'ASL-subgroup' within the Gorter group. Lydiane, Leonie, Merlijn, Sophie, Thijs, Lena, Barbara and Danielle thank you for the inspiring discussions during our weekly ASL journal clubs. Thanks to the informal atmosphere I got a lot of good feedback on my own projects as well as broadened my knowledge on ASL.

Clemens, thank you for your unwavering support and your positive energy. You showed me that doing research should be fun, driven by an inherent curiosity. I especially enjoyed our open discussions on MR physics and ASL. During those discussions, you always treated me as an equal, which helped me grow as an independent researcher. I would also like to thank the rest of the drag-and-drop group; Isabell, Anita and Marijn for the good collaboration!

In particular, I would like to thank Isabell, who has made my PhD journey so much more enjoyable. It was amazing to be able to work together with you so closely. Our numerous scanning sessions together not only helped my research, but also broadened my knowledge of techno. In addition, thanks to your organizational skills I never missed any deadline nor forgot any important items on our numerous trips.

Cyril and Deji, thank you for the helpful discussions and advice on science and PhD-life during coffee breaks and lunch. Our trips to the ISMRM-conferences, together with Isabell, form some of the best memories I have of my time as a PhD candidate.

Megan, it was so much fun being the supervisor of your masters project. Now I know what cucumbers and melons look like in the MRI scanner!

Also the rest of the group at the UMC, specifically Alberto, Carlo and Beatrice, thank you for the good times in and outside of the hospital!

At the LUMC, I would like to thank Lydiane for all the baked goods, that kept me going whenever I was frustrated, as well as the good stories and positive vibes. I really enjoyed our coffee breaks at the C2 coffee room discussing science and the latest gossip together with Leonie.

In addition, I would like to thank my bunker-mates Lydiane, Thijs, Reijer, Annemieke and Nadieh who by their presence completely made up for the lack of sunlight in the office.

I feel privileged that I have been part of the 'Gorter-family' at the LUMC. It is very stimulating to be part of a group of such talented researchers, and I greatly enjoyed our weekly group meeting and Friday afternoons at Lemmy's.

I would also like to thank my mum, dad and my sister Isabel for their unwavering support. In particular, I would like to thank my dad for teaching me to always stay curious and for inspiring me to pursue a career in science, which has brought me so much joy and satisfaction.

Miko, thank you for your support and advice during our numerous evening walks where I could vent my frustrations. Your love and support helped me grow and become a better researcher. This January, as ultimate cherry on the pie of my PhD-time, our daughter Liz was born. You two put everything else into perspective.



**Blood flow velocity**

